Université Lille I - Sciences et Technologies

Laboratoire de Mécanique de Lille (UMR CNRS 8107)

École Doctorale Science Pour l'Ingenieur Lille Nord-de-France

Année 2014 - N^o d'ordre : 41608

Thèse

Pour l'obtention du grade de

Docteur de l'Université Lille I - Sciences et Technologies

Discipline : Génie Civil

présentée par:

Hamid GHORBANBEIGI

Modélisation multi-échelle du comportement mécanique des matériaux cimentaires soumis à la carbonatation ou à la lixiviation

---

Soutenue publiquement le 12 Décembre 2014 devant le jury composé de

A. Giraud	**Professeur, INPL, Ecole de Géologie**	**Rapporteur**
Y. Malecot	**Professeur, Université Grenoble I**	**Rapporteur**
D. Kondo	**Professeur, Université Paris VI**	**Examinateur**
J.F. Shao	**Professeur, USTL, LML**	**Directeur de thèse**
I. Yurtdas	**Maître de conférences, Université de Reims**	**Co-encadrant**
W.Q. Shen	**Maître de conférences, USTL, LML**	**Co-encadrant**

Remerciements

Je souhaite tout d'abord remercier très chaleureusement le Professeur Jian-Fu Shao pour m'avoir accueilli au sein du Laboratoire de Mécanique de Lille, de m'avoir encadré et guidé durant ces trois années de thèse sur des sujets originaux avec beaucoup de rigueur et patience, mais aussi d'avoir mis en ma possession tout le besoin nécessaire pour achever ce travail dans les meilleurs conditions.

Je suis extrêmement reconnaissant envers le Professeur Djimedo Kondo qui m'a fait l'honneur de présider mon jury de thèse. Je souhaite remercier Messieurs Albert Giraud et Yann Malécot qui ont accepté la lourde tâche de juger ce travail et d'avoir suggéré des remarques pertinentes.

Mes remerciements s'adressent ensuite à Ismael Yurtdas pour m'avoir encadré et parce qui a toujours été là pour moi, malgré la distance et qui m'a toujours apporter son soutien. Je tiens particulièrement à le remercier pour m'avoir beaucoup aidé durant la rédaction et la présentation de cette thèse. Je remercie également Wanqing Shen, qui m'a encadré et transmis ses connaissances scientifiques dans le domaine de la micromécanique.

Je tiens à exprimer ma sincère reconnaissance au Professeur Jean-Baptiste Colliat dont j'ai eu l'occasion de renforcer mes connaissances scientifiques avec ces precieux conseils, mais aussi de m'avoir appris à utiliser les outils les plus indispensables pour la recherche. Je souhaite exprimer ma gratitude envers lui et le Professeur Nicolas Burlion pour leurs précieux conseils et leurs soutiens envers moi.

Mes remerciements s'adressent également à mes professeurs, amis et collègues dont je ne citerai pas leur nom par peur d'en oublier certains.

Je ne remercierai jamais assez ma famille, mes parents et Mahban, pour leurs soutiens et encouragements tout au long de l'élaboration de ce travail.

Abstract

The objective of this thesis concerns the modeling of cement based materials subjected to chemical degradations such as carbonation and leaching. In the first part, a macroscopic model has been used in order to identify the parameters influenced by chemical degradations and characterize their evolution along with the change of the microstructure. The analysis of this first part will be used in the second part to develop micro-macro models allowing us to explicitly link the evolution of microstructural parameters to the change of the macroscopic mechanical behavior. The multi-scale approach is possible by considering the material being a composite which is constituted of several components at various scales (micro-meso-macro). Several steps of non-linear homogenization based on the modified secant method will be required depending on the studied material (cement paste or concrete) to obtain the macroscopic criterion.

Keywords: Micromechanics, Plastic criterion, Drucker-Prager, Cement paste, Concrete, Micro-macro models, Carbonation, Lixiviation, Nonlinear homogenization, Inclusions, Porosity, Calcite

Resumé

L'objectif de cette thèse se porte sur la modélisation des matériaux cimentaires soumis aux dégradations chimiques telles que la carbonatation et la lixiviation. Dans la première partie, un modèle macroscopique a été utilisé afin d'identifier les paramètres influencés par ces dégradations chimiques et de caractériser leur évolution avec le changement de la microstructure. L'analyse de cette première partie servira par la suite pour la modélisation de la seconde partie en développent des modèles micro-macro permettent ainsi de lier explicitement l'évolution des paramètres microstructuraux au changement du comportement mécanique. L'approche multi-échelle est possible en considérant le matériau étant un composite qui est constitué de plusieurs composants aux échelles différentes (micro-méso-macro). Plusieurs étapes d'homogénéisation non-linéaire basée sur la méthode sécante modifiée seront nécessaires selon le matériau à étudier (pâte de ciment ou béton) pour aboutir au critère macroscopique.

Mots clés: Micromécanique, Critère de plasticité, Drucker-Prager, Pâte de ciment, Béton, Modèles micro-macro, Carbonatation, Lixiviation, Homogénéisation non linéaire, Inclusions, Porosité, Calcite

Contents

Principal Notations

- **Tensorial notations**:

C	scalar	.	simple contraction
$\boldsymbol{C}$	vector and second order tensor	:	double contraction
$\mathbb{C}$	fourth-order tensor	$\otimes$	tensor product
δ_{ij}	Kronecker delta δ_{ij}=1 if i=j, else δ_{ij}=0		
$\mathbf{1}$	second-order Identity tensor		
$\mathbb{I}$	fourth-order symmetric Identity tensor		$\mathbb{I}_{ijkl} = \frac{1}{2}(\delta_{ik}\delta_{jl} + \delta_{il}\delta_{jk})$
$\mathbb{J}$	spherical projection tensor of isotropic 4-order tensors		$\mathbb{J} = \frac{1}{3}(\mathbf{1} \otimes \mathbf{1})$
$\mathbb{K}$	deviatoric projection tensor of isotropic 4-order tensors		$\mathbb{K} = \mathbb{I} - \mathbb{J}$
tr$\boldsymbol{C}$	trace of the tensor $\boldsymbol{C}$		
$\boldsymbol{C}_d$	deviatoric part of tensor $\boldsymbol{C}$		$\boldsymbol{C}_d = \boldsymbol{C} - \frac{1}{3}\text{tr}\boldsymbol{C}$

- **Material and interface parameters for Chapter 2**:

E	Young's modulus
ν	Poisson's ratio
a_1	Parameter defining the slope of the failure envelope
a_2	Parameter defining the curvature of the failure envelope
a_3	Parameter defining the hydrostatic tension of the failure envelope
f_c	Uniaxial compressive strength
B	Parameter controlling strain hardening rate
n	Parameter describing confining pressure effect on strain hardening
η_c	Dilatancy parameter
C_0	Initial normal stress of interface
B_0	Initial shear stress of interface
α	Parameter related to normal stress softening of interface
β	Parameter related to shear stress softening of interface
$\boldsymbol{K}$	Second order interface striffness tensor
$\boldsymbol{K}^{ep}$	Second order elastoplastic interface stiffness tensor
k_n	Elastic normal stiffness of interface
k_t	Elastic shear stiffness of interface
h	Thickness of the shear band
μ	Internal characteristic length for localization

- **Common notations in all Chapters 3 and 4:**

$\boldsymbol{\sigma}$	Microscopic stress tensor
$\boldsymbol{\varepsilon}$	Local strain tensors
$\boldsymbol{d}$	Local strain rate
π	Support function
$\boldsymbol{\varepsilon}^e$	Elastic local strain tensor
$\boldsymbol{\varepsilon}^p$	Plastic local strain tensor
$\sim$	Symbol denoting the mesoscopic scale
$\boldsymbol{\Sigma}$	Macroscopic stress tensor
$\boldsymbol{E}$	Macroscopic strain tensors
$\boldsymbol{D}$	Macroscopic strain rate
f	Porosity
ρ_c	Calcites volume fraction
ρ_a	Aggregates volume fraction
T	Frictional coefficient
t	Dilation coefficient
h	Hydrostatic tensile strength
C^{hom}	Homogenized Value of C
k	Bulk modulus
μ	Shear modulus
σ^p	Local isotropic prestress
E	Young's modulus
ν	Poisson's ratio
Ω	Domain occupied by the REV
$\partial\Omega$	boundary on the REV

Introduction Générale

Les matériaux cimentaires sont affectés notamment par les attaques chimiques tout au long de leur durée de vie. En effet, le milieu poreux interne des matériaux n'est pas un environnement neutre et réagit avec toute modification du milieu extérieure. Les réactions chimiques entre le matériau cimentaire et le milieu agressif environnant entraînent des changements dans la microstructure du matériau et par conséquent sur le comportement mécanique et peut ainsi avoir un impact important sur la durabilité des structures. Les matériaux cimentaires considérés ici sont les pâtes de ciment et les bétons. Deux principales réactions chimiques sont considérées dans le cadre de cette thèse, à savoir la carbonatation et la lixiviation qui affectent très différemment le matériau.

La carbonatation est une réaction chimique lente qui se produit dans les matériaux cimentaires avec la diffusion du CO_2 dans les pores et les réactions consécutives de dissolution/précipitation avec les hydrates, notamment la portlandite $Ca(OH)_2$ et les C-S-H. Les principales conséquences de cette réaction sont la formation de calcite $CaCO_3$ et une diminution de la porosité. Dans le cadre du projet de séquestration du CO_2, la carbonatation joue un rôle majeur sur le comportement mécanique et la durabilité des puits de pétrole, car ces derniers sont en partie constitués de ciment. Dans le contexte de stockage des déchets radioactifs, les déchets peuvent aussi générer du dioxyde de carbone provenant de la dégradation des matières organiques, ce qui va réagir avec le tunnel en béton tout autour. Puisque le taux de dioxyde de carbone de l'atmosphère ne cesse d'augmenter, l'effet de carbonatation est de plus en plus important de nos jours sur toutes sortes de structure en béton. La carbonatation n'est pas considérée comme une dégradation dans un premier temps car elle protège le béton et sa structure poreuse et augmente sa résistance mécanique. Toutefois, en diminuant le pH du milieu, elle peut conduire à la corrosion des armatures dont la propagation est à l'origine des fissures et du décollement du béton d'enrobage. Il peut aussi être à l'origine de la carbonatation partielle d'une structure à base de ciment, ce qui conduit à une hétérogénéité de la structure et par conséquent des fissures peuvent apparaître.

La lixiviation est un phénomène qui se produit lors de l'exposition des matériaux cimentaires à l'eau déminéralisé ou aux fluides acides. En effet, la solution interstitielle du béton est fortement basique et chargée en ions de calcium, ce qui impose donc un fort gradient de concentration des ions vers l'extérieur. Ceci conduit à la décalcification des hydrates qui a pour conséquence d'augmenter la porosité et de diminuer la résistance du

matériau. L'évaluation de l'impact de cette dégradation est cruciale pour les conteneurs de déchets radioactifs enfouis dans le sol ou les puits pétroliers.

Pour la caractérisation du comportement mécanique de ces matériaux chimiquement influencés, deux approches différentes sont proposées dans cette thèse: l'approche macroscopique et microscopique. Dans la première partie de cette thèse, une approche macroscopique est utilisée. L'intérêt est d'utiliser un modèle élastoplastique classique pour voir l'influence de la carbonatation et la lixiviation sur les paramètres élastiques et plastiques. Dans la deuxième partie, en prenant avantage des modèles micros-macro, il est possible de lier explicitement l'évolution de la microstructure durant la dégradation au comportement mécanique du matériau.

Cette mémoire de thèse se décompose donc de quatre chapitres de la manière suivante:

Le premier chapitre présente la problématique dans son ensemble. Nous présentons une étude bibliographique générale concernant l'effet de la carbonatation et de la lixiviation sur les matériaux cimentaires. Auparavant, quelques généralités sur les matériaux cimentaires sont rappelées. Notons que le processus de carbonatation et de lixiviation étant lent dans des conditions ordinaires, les expérimentateurs ont recours à des procédés permettant d'accélérer ces processus. Nous terminons ce chapitre en mettant l'accent sur l'évolution de la microstructure et des propriétés mécaniques avec la carbonatation et la lixiviation.

Dans le deuxième chapitre, nous nous intéressons premièrement à la modélisation macroscopique des effets du CO_2 et des dégradations chimiques par les fluides acides sur le comportement mécanique multiaxial d'une pâte de ciment pétrolier (class "G"). Cette action s'articule en particulier au sein du projet REGASEQ de TOTAL. La modélisation s'effectue en deux parties. La première partie a pour objectif de modéliser le comportement multiaxial de la pâte de ciment jusqu'au pic, par un modèle phénoménologique [1] et de montrer l'effet de la carbonatation et lixiviation sur les paramètres élastiques et plastiques liés au modèle. Ce modèle servira de base pour une modélisation des processus de localisation des deformations et de la rupture. Dans une seconde partie, ce chapitre est consacré à la modélisation de la fissuration localisée des matériaux cimentaires, toujours par une approche macroscopique. Le modèle phénoménologique de base est ainsi étendu par l'introduction d'une fissure orientée dans le volume élémentaire représentatif. Une loi de comportement spécifique est proposée pour la fissure localisée considérée comme une interface. Le modèle de comportement homogénéisé est implémenté dans un code

de calcul par éléments finis. Des simulations numériques sont présentées sur les essais de laboratoire pour prendre en compte le comportement radoucissant du matériau.

Le troisième chapitre est dédié à la modélisation micro-macro de la pâte de ciment sous l'effet de la carbonatation ou de la lixiviation. La pâte de ciment est considérée comme une matrice poreuse. Pour le cas de la carbonatation, des grains de calcite sont formés durant le processus chimique et la porosité diminue. Dans ces conditions, la pâte de ciment est considérée comme un matériau à trois phases: une phase solide qui représente le ciment, de petites inclusions représentent la calcite qui renforce la matrice cimentaire, et des pores qui sont entourés de cette matrice renforcée. Pour des raisons de simplification et pour pouvoir formuler le critère macroscopique, nous considérons les inclusions comme étant rigides. Les pores et les inclusions sont aléatoirement repartis et ont une forme sphérique. Deux étapes d'homogénéisation non-linéaire basée sur [2] sont nécessaires pour formuler le critère macroscopique. Pour le cas de la lixiviation, nous mettons à profit directement le critère obtenu par [2] pour une phase solide entourant des pores sphériques.

Dans le quatrième chapitre, une extension du modèle présenté dans le chapitre 3 est proposée, pour tenir compte de l'effet des granulats pour une application sur les bétons. Il s'agit donc de faire une troisième homogénéisation pour introduire l'effet de grosses inclusions (granulats). Ce modèle prend en compte les matériaux à quatre phases: une phase solide, de petites inclusions, des pores et de grosses inclusions (granulats). Il pourra donc être appliqué pour évaluer l'influence de la carbonatation, et aussi celle de la lixiviation en éliminant l'effet des petites inclusions (calcites).

Part I

Macroscopic Approach to Carbonation and Lixiviation of Cement Paste

Chapter 1

A Review of Carbonation and Lixiviation of Cement-Based Materials

Contents

1.1 Introduction

In many engineering applications such as nuclear power plants, disposal and storage of radioactive wastes, drilling of oil wells, and sequestration of residual gases in depleted reservoirs, cement-based materials are subjected not only to mechanical loading, but also to moisture transfer, variation of temperature and chemical degradations. The durability analysis of such sensitive structures requires the consideration of such multi-physical coupling phenomena. Two different chemical reactions, namely carbonation and lixiviation, are considered within the framework of this thesis.

Carbonation is a phenomenon largely encountered in cement-based materials. It corresponds to physical and chemical mechanisms resulting from the instability of portlandite ($Ca(OH)_2$) and calcium silicate hydrate (C-S-H) phases under the influence of carbon dioxide (CO_2). The penetration of CO_2 into the porous network causes a chemical reaction mainly in the hydrated cement materials. This action transforms the hydration products, notably the calcium hydroxide ($Ca(OH)_2$) and C-S-H to the calcium carbonate ($CaCO_3$). Lixiviation, which is a non-uniform evolution process like carbonation, mainly comes from leaching of the above cited main component of cement paste: the first dissolves completely while the second decalcifies itself gradually by the reduction of C/S ratio in solid phase, leading to a progressive enrichment of C-S-H in siliceous. These two chemical processes cause significant changes in the microstructure and mechanical behavior of cement-based materials.

In the following, the process of cement hydration is first presented. Then, mechanisms of carbonation and lixiviation are detailed. Finally, the effects of these two chemical degradations on the evolution of the microstructure and mechanical properties of cement-based materials are presented and analysed.

1.2 Some Generalities on Cement-Based Materials

1.2.1 Hydration of cement

Cement is a hydraulic binder and has a very complex mineral composition. It is made of clinker and a few percent of gypsum $CaSO_4.2H_2O$ which is necessary to regulate the rate of set. Clinker is obtained by mixing at high temperature of 1400 - 1600 °C the “limestone” that brings calcium oxide CaO and the “clay” that brings silica SiO_2, aluminium oxide Al_2O_3 and iron oxide Fe_2O_3. These oxides represent about 95% of cement mass. The four main compounds of clinker are listed in Table 1.1 with commonly used abbreviations (C=CaO, S=SiO_2, H=H_2O, A=Al_2O_3, F=Fe_2O_3).

Name	Formula	Abbreviation	mass %
Tricalcium silicate (alite)	$3CaO.SiO_2$	C_3S	50-70
Dicalcium silicate (belite)	$2CaO.SiO_2$	C_2S	15-30
Tricalcium aluminate	$3CaO.Al_2O_3$	C_3A	5-10
Tetracalcium aluminoferrite	$4CaO.Al_2O_3.Fe_2O_3$	C_4AF	5-15

TABLE 1.1: Mineral composition of clinker

European standards (NF EN 197-1) distinguish five types of cement depending on the amount of clinker and other constituents such as blast furnace slag, fly ash, pozzolana, silica fume, etc.

The addition of water to cement leads to hydration of cement which corresponds to the whole chemical reactions occurring between cement and water. These chemical reactions take place before setting and continue long time after but more and more slowly corresponding to hardening [3]. Setting occurs within a few hours without significant compressive strength development while during hardening there is an important increase in mechanical properties.

The main hydrates are derived from hydration of dominant anhydrous phases which are C_3S and C_2S (Table 1.1). As a result of hydration at ambient temperature (see (1.1) and (1.2)), silicates form calcium hydroxide also called portlandite (CH) and an amorphous calcium silicate hydrate (C-S-H). Hydration of aluminate (C_3A) in presence of gypsum forms ettringite, monosulfoaluminate and hydrated aluminates. Aluminoferrite (C_4AF) gives the same hydrates as aluminates, their formulas are obtained simply by total or partial substitution of aluminium by iron. As an example, hydrated cement paste is constituted (in mass) approximately by 70% C-S-H, 20% CH and 10% remaining hydrates. Thus, the main compounds of cement paste are C-S-H and CH.

$$C_3S + (3 - x + y)H \longrightarrow C_xSH_y + (3 - x)CH \tag{1.1}$$

$$C_3S + (2 - x + y)H \longrightarrow C_xSH_y + (2 - x)CH \tag{1.2}$$

1.2.1.1 Portlandite ($Ca(OH)_2$)

Portlandite is the outcome of calcium excess in hydration of C_3S and C_2S and crystallizes in the form of hexagonal platelets piled between grains of partially hydrated cement. The size of platelets can vary from a few micrometers to a few dozen micrometers and increases with the W/C ratio [4]. Portlandite has no significant mechanical strength but

its solubility in water is about 1.6 g/L [5], allowing to maintain pH of the pore solution to about 13, and hence it plays a major role in sustainability concerns.

1.2.1.2 Calcium Silicate Hydrates (C-S-H)

C-S-H are considered as a real "glue" of cement paste and thus at the origin of the main properties of hardened cement paste, in particular its mechanical strength [6]. They originate from hydration of alite (C_3S) and belite (C_2S) as shown in reactions (1.1) and (1.2). There are however many various stoichiometric formulas for C-S-H hydrates within the same cement paste. The ratio of C/S is generally between 0.8 and 1.7. The exact structure of C-S-H in cement paste has been still studied. C-S-H are hydrates of small degree of crystallinity and thus qualified as "gel". The elementary particle of C-S-H would be a lamellar micro-crystal. Each lamina is composed of two or three layers spaced every 17 angstroms with an average thickness of 30 angstroms. Several models of the structural unit of C-S-H have been proposed in order to reproduce its evolutions, and to connect these evolutions to macroscopic variations (shrinkage, creep, phenomena of sorption). The model of Feldman and Sereda [7] seems to be the most used to justify these macroscopic variations. According to this model, the structure in layer of C-S-H is the consequence of an irregular arrangement of poorly crystallized simple layers which form interlayers spaces by approaching one to another. Thus, these spaces do not have fixed dimension and volume. Layers can have reversible relative movements whereas the coming in or coming out of the water of inter-foliaceous spaces can be irreversible. The layers are bound by ionic or covalent forces, and by the Van der Waal forces which balance the disjointing pressure.

1.2.2 Porosity

The cement paste structured during hydration is a porous solid medium consisting of hydrated and anhydrous solid phases and an interstitial solution partially filling the pores. The porous network depends on arrangement of various products of hydration. The mercury porosimetry analysis of cement pastes reveals mainly two families of pores (see Fig. 1.1).

- capillary pores that are initially occupied by the mixing water and not filled by hydrates. Their diameter varies from few hundred to a few thousand angstroms. For a given age, typical dimension and the total volume of these capillary pores increase with W/C ratio, and for a given W/C ratio, the total volume decreases with maturation.

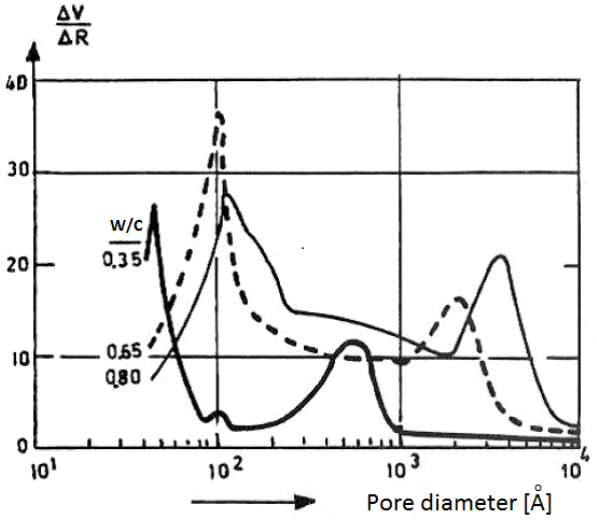

FIGURE 1.1: Curves of porosity distribution for different cement pastes [8]

- pores of hydrates that represent interlayer spaces. Their characteristic radius, approximately 17 angstroms, depends a bit on W/C ratio and conditions of hydration, and thus constitutes an intrinsic characteristic of the formed hydrates. The increase in the quantity of these hydrates during maturation leads to an increase in micro-porosity. The total volume represented by this intrinsic micro-porosity is approximately 26% of the volume of hydrates.

It is worth noting that there is also porosity created by micro-cracking and occluded air bubbles that favour connectivity of the porous medium.

1.2.3 Evolution of mechanical strength with hydration, and effects of temperature

The contacts between grains increase while capillary porosity decreases with formation of C-S-H. This hardening leads to the increase in mechanical properties of material such as compressive and tensile strengths and Young's modulus. Fig. 1.2 shows the evolution of the degree of hydration and compressive strength versus time. The compressive strength increases with formation of hydrates that fill capillary porosity, but the influence of the nature of the formed hydrates has a secondary effect on strength development. Note that the increase in Young's modulus also depends on the development of hydration but the modulus tends more quickly to a stabilisation.

The increase in curing temperature influences the hydration process and mechanical properties. According to Taylor [10], the chemistry of hydration is essentially the same between 25°C and 100°C. However, the temperature accelerates hydration process and

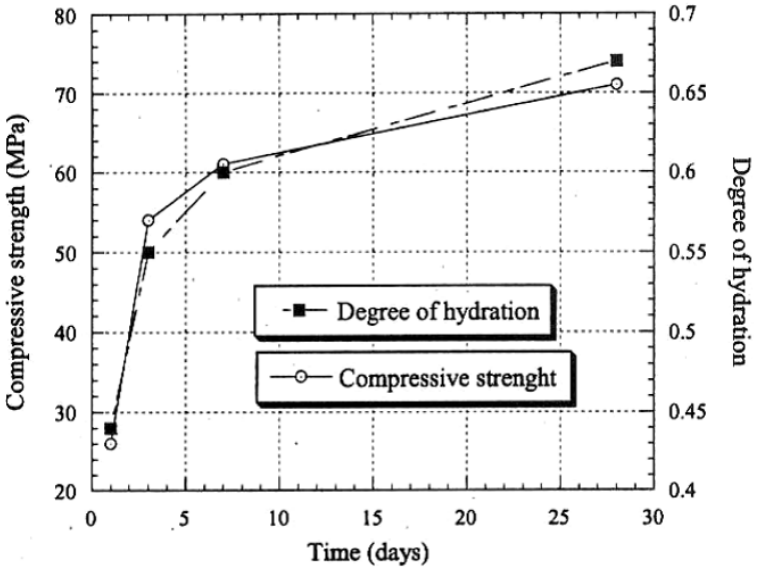

FIGURE 1.2: Evolution of the degree of hydration and compressive strength of a mortar versus maturation time [9]

modifies the volume fractions of different phases [10]. Hydration at higher temperature increases the porosity and results in a more porous and more heterogeneous low density C-S-H but a less porous high density C-S-H [8, 11]. These modifications due to temperature increase in cement paste porous structure lead to an increase of early age strength but a decrease of long-term strength [8, 12].

1.2.4 Interfacial transition zone (ITZ)

The addition of aggregates in an ordinary cement paste leads to the creation of a new zone at the paste/aggregate interface. This is due to the modifications of local conditions of hydration, generated by the water excess in this zone [5, 13, 14]. Cement paste structure changes on a certain distance that increases with the size of aggregates and W/C ratio but remains always lower than 50 µm. Therefore, the porosity of this zone is higher than the bulk paste. This zone of low strength constitutes the weakest point of the ordinary strength cement-based materials subjected to mechanical, chemical or physical actions.

1.3 Carbonation of Cement-Based Materials

CO_2 penetrates into the material by the porous network or cracks. Its diffusion through the porous medium is conditioned by the hygroscopic state of material pores [15]. It can penetrate through the liquid phase when there is a transfer of water containing

dissolved CO_2, or when water is already present, by diffusing in the aqueous phase. It can penetrate through gaseous phase when the accessible porous network is desaturated [16].

The contact of CO_2 with commonly used cementitious materials in the presence of moisture, makes long terms chemical reactions named as carbonation. Carbonation occurs even at low concentrations of CO_2 into the atmosphere where its volume fraction into the air is about 0.03%. In poorly ventilated facilities, this proportion may reach 0.1%, and in larger cities or industrial zone, the average is about 0.3%. It can reach 1% in exceptional conditions such as walls of road tunnels, urban and underground parking garages which are submitted to high concentration of CO_2 [17–19].

Carbon dioxide is produced by various processes but is mainly caused by fossil fuel combustions due to the dependence of economies and growing demands on the world's energy and human activities over the past decades. The substantial rise of global temperature and the consequent climatic change is a direct outcome of massive discharge of greenhouse gases such as CO_2 into the atmosphere [20]. Of all other greenhouse gases, CO_2 is responsible for about 64% of the enhanced 'greenhouse effects', making it the target for mitigation of greenhouse gases [20]. The oil wells could be used as barrier for sealing geological sequestration of acid gases such as CO_2 and H_2S in depleted reservoirs. These acid gases produced by industrial activities could be also used in the oilfield as a kind of oil-displacing agent to enhance the recovery of oil [21] and to offset the cost of CO_2 capture. Cement based-materials are used in the Oil and Gas industry for cementing casing and plugging well-bores. Therefore, it can be exposed to different chemical environments when supercritical CO_2 is sequestrated in geological formations (that means a storage at depths greater than 800 m where the pressure is higher than 7.38 MPa and the temperature is higher than 31.1 °C [22]). Even if the precipitation of calcium carbonates leads to densify the cement paste and thus to an improvement in mechanical and hydraulic properties, this aggressive environment could potentially cause the degradation of cement paste [22–24] as it is thermodynamically unstable in CO_2-rich environment [23].

In this section, the process of carbonation is first described. Then, its effects on the microstructure and mechanical properties of cement-based materials are presented.

1.3.1 Dissolution of carbon dioxide in liquid phase

When a solution is subjected to CO_2, the gas dissolves and forms the carbonic acid H_2CO_3. The influence of partial pressure of CO_2 is very important: more partial pressure engenders faster carbonation progress.

$$CO_2 + H_2O \rightleftharpoons H_2CO_3 \tag{1.3}$$

Carbonic acid H_2CO_3 behaves as a weak unstable acid whose dissociation takes place in two phases designated by the following reactions as a function of pH value:

$$H_2CO_3 + OH^- \rightleftharpoons HCO_3^- + H_2O \tag{1.4}$$

$$HCO_3^- + OH^- \rightleftharpoons CO_3^{2-} + H_2O \tag{1.5}$$

In hydrated cement-based materials, the aggressivity of a carbonated solution towards portlandite is in function of pH and concentration of total carbonates (ΣHCO_3^{2-}). It should be noted that, in view of the high alkalinity of cementitous materials, CO_3^{2-} is the major dissolved substance.

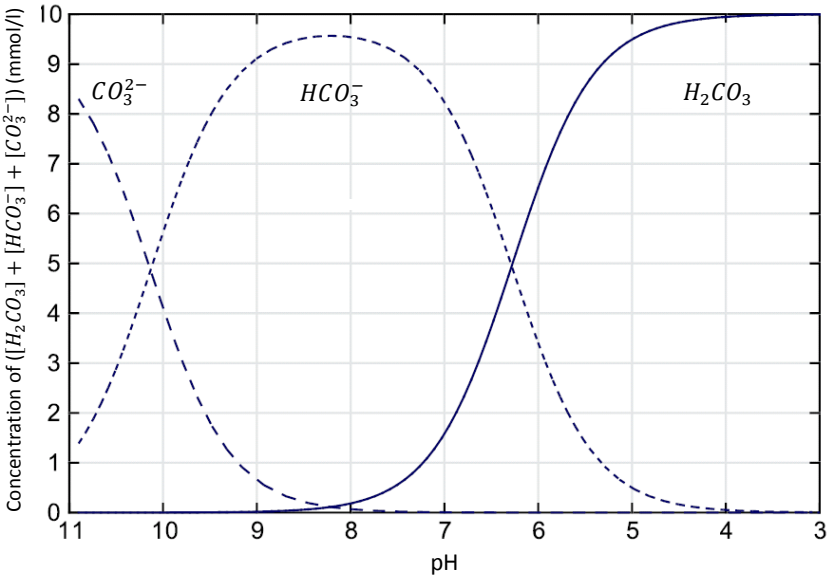

FIGURE 1.3: Carbonate concentration in function of pH [25]

Each of the dissociation reactions (1.4) and (1.5) corresponds to the acidity of carbonic acid H_2CO_3. As shown in Fig. 1.3, at equilibrium, these two acids have disjoint predominant areas. For pH greater than 10.3, CO_3^{2-} predominates and for pH ranging between 6.3 and 10.3, HCO_3^- predominates. Throughout carbonation process, the interstitial solution pH of the cementitous material decreases from a value near 13 to a value lower than 9 [18]. Therefore the existence of disjoint predominant areas has an important impact on carbonation process.

1.3.2 Carbonation of portlandite ($Ca(OH)_2$)

As the dissolution of CO_2 in interstitial pore solution decreases the pH, portlandite dissolves according to reactions (1.6) and (1.7) to re-establish the alkalinity of the porous medium.

$$Ca(OH)_2 \rightleftharpoons CaOH^+ + OH^- \tag{1.6}$$

$$Ca(OH)^+ \rightleftharpoons \quad Ca^{2+} \quad + OH^- \tag{1.7}$$

The calcium ions released with the chemical alteration of portlandite react with carbonate ions to form a salt known as calcium carbonate $CaCO_3$.

$$Ca^{2+} + CO_3^{2-} \rightleftharpoons CaCO_3 \tag{1.8}$$

Calcium carbonate exists in three different polymorphic forms: vaterite, aragonite and calcite. According to [26], calcite is the most stable form in standard pressure and temperature [27, 28]. The two other forms exist at short terms in low quantity in carbonated cement-based materials.

In the context of a simplified approach, it is possible to summarize the carbonation of portlandite by the following heterogeneous chemical reaction:

$$Ca(OH)_2 + CO_2 \rightarrow CaCO_3 + H_2O \tag{1.9}$$

The use of this formulation hides intermediate steps of the mechanism, but has the advantage to show a release of water with carbonation of portlandite. Fig. 1.4 illustrates schematically principal chemical reactions involved in carbonation of portlandite through gas, liquid and solid phases.

It is important to mention that normally carbonation of portlandite at initial stages is faster than C-S-H, however there is a turning point when a large amount of microcristals of calcium carbonate are formed on the surface of portlandite. This prevents a part of portlandite to continue the carbonation process and slows down the carbonation rate of the latter [17].

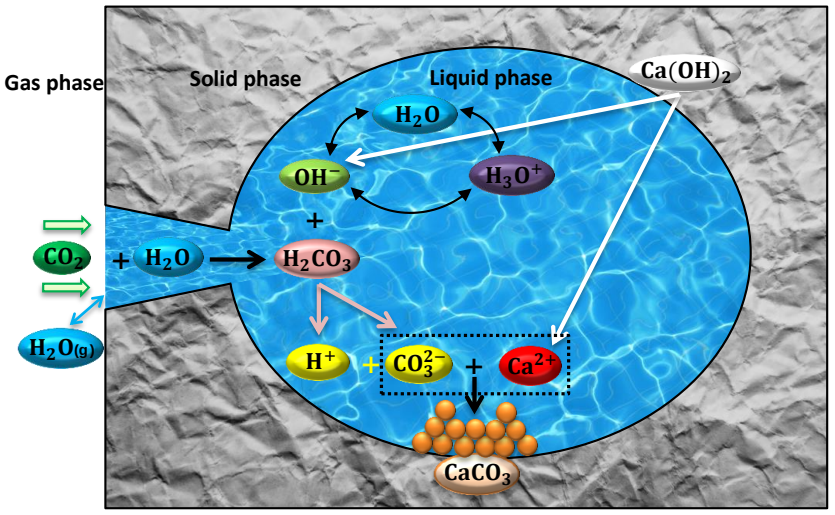

FIGURE 1.4: A schematic representation of portlandite carbonation mechanism

1.3.3 Carbonation of Calcium Silicates Hydrates (C-S-H)

Carbonation of C-S-H results in the formation of calcium carbonate $CaCO_3$, an amorphous silica gel and eventually water. In fact, when CO_2 is dissolved into the water, it grabs calcium ions in the C-S-H releasing silicate ions. Calcium ions enter in reaction with carbonate ions, while the silicate ions may condense with other silicates in C-S-H to form at the end, long silica chains low in calcium. Carbonation of C-S-H hydrates takes place according to the following reaction:

$$C_xS_yH_z + xH_2CO_3 \rightarrow xCaCO_3 + ySiO_2.tH_2O + (x - t + z)H_2O \tag{1.10}$$

Carbonation makes all of C-S-H gel almost disappear while portlandite remains in noticeable amounts. This may be associated with the creation of $CaCO_3$ that forms a dense layer around portlandite and prevents them from continuing to be carbonated. In addition, C-S-H hydrates provide a reaction surface larger than portlandite crystals [17].

Moreover, as previously indicated, these C-S-H hydrates which represent the most important part of the hydrated cement paste give to the cement matrix its main mechanical strength. However, their pH buffering capacity of the solution is lower than portlandite. Therefore, their incorporation into the carbonation mechanism is not crucial. However, they induce important change in the microstructure that must be taken into account [17].

Phases containing aluminates and alkalines are also subject to carbonation. But, as they are of low quantity in common cement-based materials, their carbonation is generally neglected.

1.3.4 Calcium carbonate ($CaCO_3$) dissolution

The beneficial effects of carbonation that initially densify cement-based material can disappear in CO_2-rich environment (supercritical CO_2, CO_2 saturated water). Indeed, the pH of the pore solution will fall below 10.5 with depletion of the calcium hydroxide and alkali phases [29–31]. As a result, bicarbonate (HCO_3^-) becomes dominant species instead of carbonate (CO_3^{2-}). This process leads to the dissolution of calcium carbonate and then to a poor strength porous silica gel.

$$CaCO_3 + CO_2 + H_2O \rightleftharpoons \quad Ca^{2+} \quad + 2HCO_3^- \tag{1.11}$$

1.3.5 Carbonation kinetics

Depth measurements of penetration can allow us to predict the evolution of carbonation depth over time. Due to the diffusive process of CO_2 penetration, it is generally assumed that the thickness of the carbonated zone during the life of a structure is given by the following empirical law (1.12):

$$x(t) = x_0 + k\sqrt{t} \tag{1.12}$$

where,

$x(m)$ is the carbonation depth and x_0(m) is the initial carbonation depth

k (m.year$^{-\frac{1}{2}}$) is a coefficient that takes into account material composition (W/C ratio, nature of cement) and also environmental conditions (humidity, temperature, pressure, ...)

t (year) is the time exposition

Furthermore, [32] proposed an empirical relation for "k" in case of accelerated carbonation. However, it seems that this relationship in square root of time is not always verified, for instance in case of a petroleum cement paste matured and carbonated under temperature of 90°C for which the relationship is rather linear [33].

There are various techniques to measure carbonation depth: pH indicator (phenolphthalein), thermogravimetric analysis (TGA) (supplemented with chemical analysis (AC)), scanning electron microscopy (SEB), gammadensitometry, X-ray diffraction, etc. The most used is the phenolphthalein because it is easy, fast and economic. The solution of phenolphthalein, applied directly to a fresh part cut in half, allows distinguishing the sound part that becomes pink, from carbonated part that remains colourless. The colour becomes pink when the pH is higher than 9. However, the carbonation profiles does not exhibit a sharp reaction with phenolphthalein as suggested by [17, 34, 35]. Fig. 1.5 presents typical carbonation profiles of $Ca(OH)_2$ and shows three distinct zones [17, 35]: non-carbonated zone (inner zone), intermediate transitional zone where the $Ca(OH)_2$ content progressively decreases toward CO_2 exposed surface and an outer zone just in front of the phenolphthalein neutralization depth. Furthermore, as it can be seen in Fig. 1.5, the phenolphthalein test does not enable the real carbonation depth to be known [17, 34–37], and underestimates it. However, this test is useful because it provides information on concrete reinforcements, whether they are already subjected to the corrosion at this depth or not.

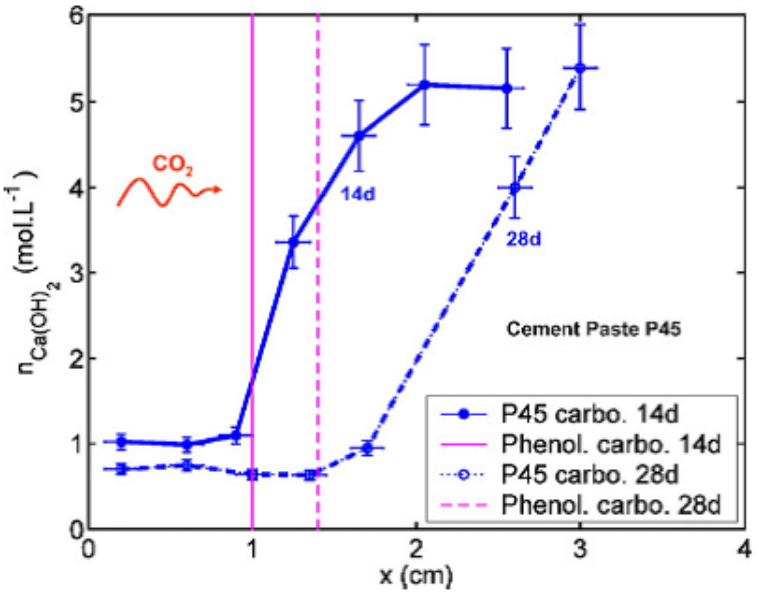

FIGURE 1.5: $Ca(OH)_2$ depth-profiles obtained by TGA and phenolphthalein after 14 and 28 days of accelerated carbonation of a cement paste with W/C=0.45 (P45) [17, 35].

1.3.6 Factors influencing the rate of carbonation

Carbonation rate depends on the parameters related to material composition, curing and environmental conditions.

The W/C ratio that conditions the porous network (porosity, permeability and diffusivity) and mechanical strength has a paramount importance on carbonation rate. Its increase favours the CO_2 diffusion in the material and causes an increase in carbonation depth. The influence of cement content on carbonation remains less important compared to W/C ratio [32]. Note that the use of binders containing slag, fly ash or silica fume increases considerably the carbonation depth as they contain less portlandite compared to Portland cement.

The properties of a cement-based material strongly depend on the curing conditions that determine the progress of hydration reactions. A prolonged wet curing is very beneficial as it increases the resistance to penetration of the aggressive agents and thus limits the carbonation depth [12].

Moreover, the environmental conditions, such as CO_2 concentration, relative humidity and temperature play a crucial role in the process of carbonation. It is clear that carbonation depth is more pronounced in rich CO_2 environments. However, carbonation depth depends on the relative humidity of the environment that determines the level of saturation in the material. Accelerated carbonation tests at ambient temperature show that carbonation depth is maximum for a relative humidity between 50 and 70% [38]. At low levels of relative humidity, the minimal water level adsorbed on the surface of pores limits the solubility of CO_2. At high levels of relative humidity, the high degree of pores saturation prevents the penetration of carbonic gas. Carbonation rate also depends on temperature increase that leads to a decrease of solubility of reagents but accelerates the transport. Note that the temperature increase accelerates carbonation process because it causes drying of the pores and then facilitates the CO_2 to access into the material pores [39]. Furthermore, the experiments carried out by [26] show that temperature increase also leads to higher carbonation depth at optimal constant relative humidity.

1.3.7 Consequences of carbonation on microstructure and mechanical behavior of cement-based materials

Here the emphasis will be put on the effect of carbonation on the evolution of microstructure and mechanical properties that forms one of the main object of this thesis.

1.3.7.1 Modification of the microstructure

Carbonation decreases the total porosity as it can be seen in table 1.2. The lower the W/C ratio the more the porosity will decrease by carbonation [40, 41]. However, other results seem to show rather an inverse order of evolution [42]. The decrease in porosity comes from the fact that the volume occupied by products of carbonation is higher than the volume of the products reacting with CO_2. Table 1.3 provides the molar volume of portlandite and the three calcium carbonate phases formed. By analysing the data of Ngala and Page [41], Thiery [17] showed that the decrease in porosity was not only due to the carbonation of portlandite but also to the carbonation of other hydrates, in particular the C-S-H. The author also reported that carbonation of portlandite would lead preferentially to the formation of calcite while the formation of vaterite and aragonite (thermally less stable) and amorphous carbonates would be rather associated with carbonation of C-S-H for the case of CEM I cement paste. Carbonation of portlandite and C-S-H leads to an increase of volume by 3.8 and 15.39 cm^3/mol respectively [43]. However, the volume increase caused by C-S-H carbonation depends on the intensity of carbonation to which the material is subjected [44].

W/C	Porosity [%]	
	sound	carbonated
0.3	19.05	—
0.4	24.05	13.4
0.5	32.3	23.0
0.8	48.0	42.3

TABLE 1.2: Porosity of sound and carbonated cement paste [40]

Cristal	**molar volume ($cm^3.mol^{-1}$)**	**Volume variation(%)**
$Ca(OH)_2$ Portlandite	33	—
$CaCO_3$ Argonite	34	3
$CaCO_3$ Calcite	35	6
$CaCO_3$ Vaterite	38	15

TABLE 1.3: Molar volume of portlandite compared with the three forms of calcium carbonate [17, 40]

Carbonation also modifies the distribution of pore sizes. In particular, the volume of pores with radius lower than 0.1 µm seems mainly to be reduced in case of CEM I cement pastes with W/C $\leq$ 0.5 [40, 45]. This can be seen clearly on Fig. 1.6. A macro-porosity with radius higher than 0.05 µm also appears for W/C=0.8 in addition to a volume reduction of pores lower than 0.05 µm [40]. Thiery [17] also registered a reduction of the fraction of pores with sizes between 6 and 10 nm for W/C=0.25 and between 10 and

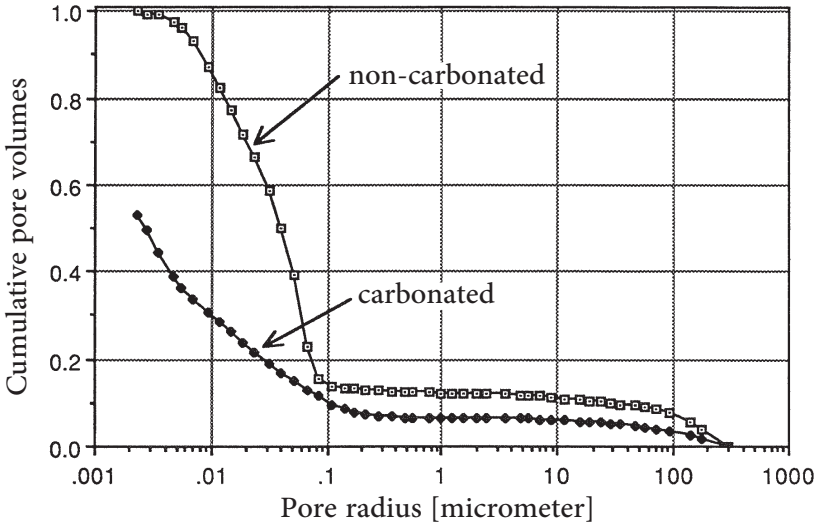

FIGURE 1.6: Pore size of hardened cement pastes of W/C=0.4 [40]

20 nm for W/C=0.35, 0.45, 0.50 and 0.60. The author also noted an increase in macro-porosity around 80-100 nm for W/C from 0.45 to 0.60: the higher the W/C ratio, the more the macro-porosity was marked. However, Ngala and Page [41] observed a slight increase in the proportion of pores with radius higher than 15 nm, but this increase was more marked for the pastes containing fly ashes or blast furnace slag. The experimental conditions of these two studies are probably at the origin of the differences observed. The appearance of the macro-porosity after carbonation can be due to the formation of silica gel which is very porous and to the possible micro-cracking of the calcite gangue surrounding the portlandite [17, 46, 47]. The higher increase in the macro-porosity of cements with mineral additions can be attributable to the fact that these additions lead to more C-S-H by reaction with portlandite, which leads to a larger quantity of silica gel formed by carbonation of C-S-H.

Moreover, although carbonation leads to an increase of solid phase it also causes a shrinkage issued from very complex origins [17, 38, 40]. This shrinkage is generally superimposed to drying shrinkage.

1.3.7.2 Influence on mechanical behavior

Carbonation leads to an increase of uniaxial compressive strength [42, 48–53] and Young's modulus [51, 52] of cement-based materials. Pihlajavaara [50] studied the effect of carbonation on uniaxial strength of two mortars with W/C= 0.5 and 0.75. After two years

of storage under sealed conditions, the prismatic samples (40×40×160 mm^3) were subjected to carbonation for two or three years in climate controlled rooms (0.05% CO_2), the relative humidity of which being 40% or 70%. Witness samples (not carbonated) enabled the effect of carbonation to be correctly evaluated. The increase observed in compressive strength (measured on the samples of 40×40×40 mm^3 after bending test on prismatic samples) mainly comes from the decrease of porosity and also from the fact that the calcite itself strengthens the microstructure. Indeed, calcium carbonate is well known to be an excellent binder, for instance it provides the main part of the strength of lime mortars [17]. Pihlajavaara [50] also noted that the increase in compressive strength was more pronounced for higher W/C ratio: approximately 10% for the first mortar and 30% for the second. This is probably due to a higher carbonation rate of the second mortar. Zornoza and al. [42] also carried out their study on mortars, with W/C= 0.5 and 0.7, but in accelerated carbonation conditions. After 28 day water maturation, the prismatic samples (40×40×160 mm^3) were left in an atmosphere with 50% RH for 21 days of desaturation then submitted to carbonation in an atmosphere with 100% CO_2 and 65±5% RH. The increase in uniaxial compressive strength was 21% and 42% respectively (measured on the samples of 40×40×40 mm^3 after bending test on prismatic samples). The comparison of the two studies for mortar with W/C=0.5 seems to indicate that the accelerated carbonation leads to higher increase of compressive strength. Note however that there is a loss of strength for cement-based materials manufactured with blast-furnace slag or fly ash containing cements [17].

Moreover, Zornoza and al. [42] observed a decrease of 45% of flexural strength for the mortar with W/C= 0.5 and a marginal increase of 2% for the mortar with W/C=0.7. The results of Pihlajavaara [50] also showed a deterioration of the flexural strength of the mortar with W/C= 0.5, especially when the RH passes from 70% to 40%. This can be explained by the fact that the volume increase due to carbonation products under severe carbonation conditions is prevented by the pores walls, in particular when W/C ratio is relatively low. This induces tensile stresses that leads to a fall of flexural strength.

Fig. 1.7 shows the effect of carbonation on the evolution of axial deformation in uniaxial compression of an ordinary concrete with W/C= 0.65 [52]. The cylindrical concrete samples (ϕ=150mm, h=300mm) were initially preserved for 28 days in a controlled environment (23±1,7°C and 100% RH) for a sufficient maturity. Then, a part of the samples were subjected to accelerated carbonation in a controlled atmosphere with 20% CO_2 and 70% RH during 48 weeks. The two ends of samples were covered with an epoxy resin in order to cause only radial carbonation. The other samples were always kept in the controlled environment to follow the effect of maturation on strength. Fig. 1.7 shows that the initially ductile behavior becomes brittle and the strain at peak decreases with carbonation. The strength increases until complete carbonation but the main strength

increase occurs within the 12 first weeks. After complete carbonation, the compressive strength and Young's modulus increase passing from 24.2 to 59.6 MPa and from 18,000 to 25,500 MPa respectively. As it can be seen in Fig. 1.8, the evolution of mechanical properties is closely linked to that of average porosity evolution (determined by mercury porosimetry) which decreases from 12.7 to 7.7% after complete carbonation.

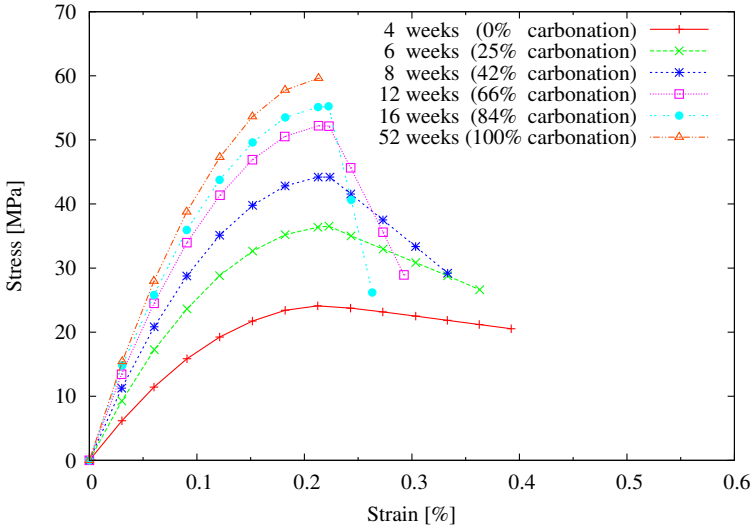

FIGURE 1.7: Stress-strain relationship of concrete with W/C=0.65 in uniaxial compression for different level of carbonation [52]

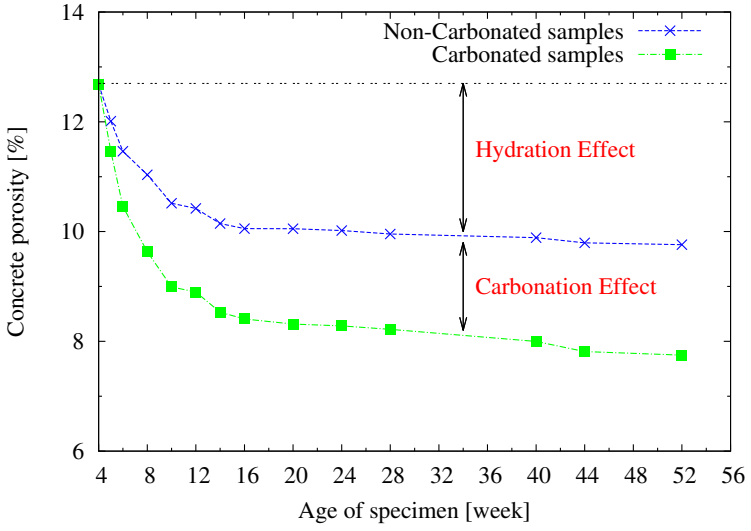

FIGURE 1.8: Effect of carbonation on concrete porosity (determined by mercury porosimetry) [52]

Note that a part of the evolution of these properties comes from continuation of the hydration and also from drying effects (capillary depression and shrinkage) caused by the passage of RH from 100 to 70% and carbonation shrinkage, during the period of the experimental program. However, the effect of maturation should be weaker than that

reported because the conditions of the samples subjected to carbonation and those used to evaluate the effect of maturation are not identical.

Few studies have been also interested in the evolution of triaxial mechanical behavior of cement-based materials. For instance, Takla and al. [33, 54] carried out a comprehensive experimental study on a classical oil cement paste (G Class cement) with a W/C ratio equal to 0.44. Two additives (a dispersing agent and an anti-foam agent) were used to pour the material. This work has been performed in collaboration with TOTAL through the research project on the feasibility study for residual gas sequestration.

The experimental study was carried out at the temperature of 90°C to get closer to borehole conditions. All samples with diameter 36 mm and height 100 mm were cast in one batch in order to have representative samples. After casting, the samples in their mold were first placed in distilled lime saturated water for 3 days in an oven regulated at 90°C. Afterwards, the samples were quickly removed and returned to the distilled lime saturated water at 90°C to reach maturation of one month in total. This maturation period was adopted to stabilize the microstructure for the evolution of mechanical properties. The tests were carried out on samples with diameter 22 mm and height 20 mm derived from the initial samples.

After the maturation phase, carbonation process was launched by injecting 100 cm^3/min of CO_2 [55] in a climatic enclosure where the temperature and relative humidity could be controlled simultaneously. The enclosure temperature was set to 90°C and the relative humidity was set to 65% which is an optimum humidity for maximum and rapid carbonation. The samples used for mechanical tests have been protected by their two extremities with aluminium foil for a more regular carbonation through their lateral surface. Note that the sound samples were also kept under conditions of 90°C and 65% relative humidity but protected from carbonation. Apart from the two extreme cases of sound and totally carbonated materials, two other carbonation depths equal to 3 mm and 6 mm were chosen. This was necessary to simulate conditions where oil wells are often partially carbonated.

Mechanical tests, consisting of uniaxial and triaxial compression tests (see Fig. 1.9) were performed on sound, partially and completely carbonated samples. For uniaxial compression test, the sample was loaded in uniaxial compression without any application of interstitial pressure until failure. For triaxial tests, the sample was initially subjected to a confining pressure of $P_c = 3, 10$ and 20 MPa. These values were chosen according to average in situ conditions. Afterwards, the sample was subjected to a fluid injection pressure of $P_i = 2.5$ MPa at the upstream and an outlet pressure of $P_o = 0$ MPa at downstream; this interstitial pressure gradient was applied for the measurement of initial permeability. The permeability was measured but is not in the subject of this study.

Next, the outlet valve of interstitial fluid was closed to get an increase of pore water pressure up to 2.5 MPa. Then, the deviatoric stress was applied to the sample until failure, by keeping the pore pressure constant throughout the test.

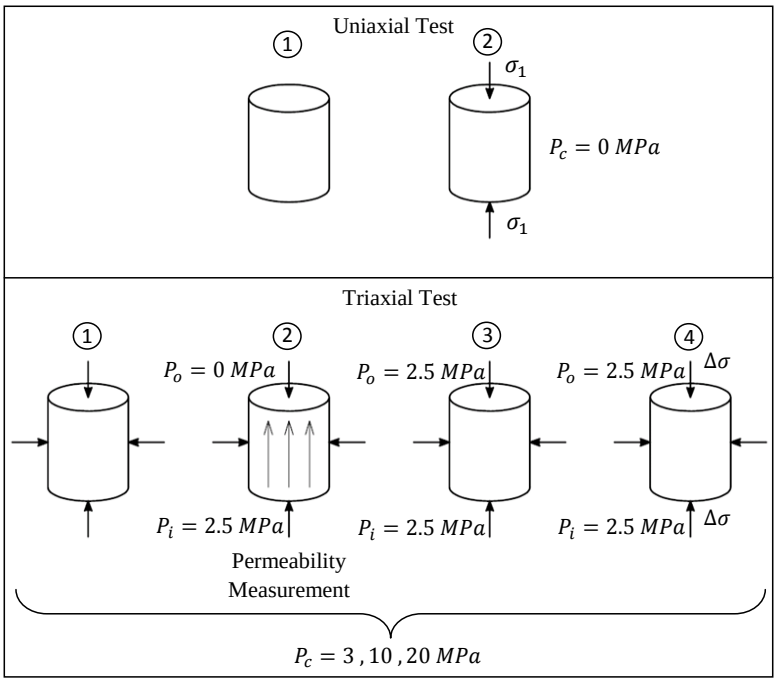

FIGURE 1.9: Schematic representation of different laboratory tests

Fig. 1.10 shows the evolution of failure strength versus carbonated volume for different confining pressures [33, 54]. Fig. 1.11 presents the evolution of water porosity with carbonated volume [54] while Fig. 1.12 presents the evolution of carbonation depth, obtained by phenolphthalein spray-test, over time [33, 54].

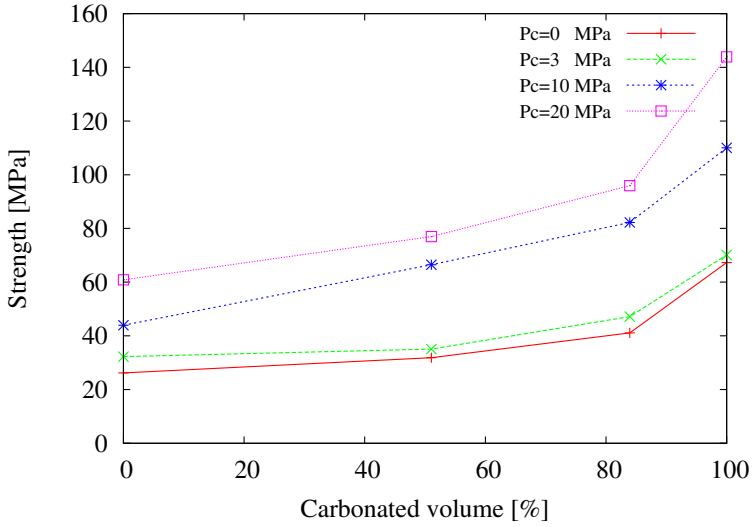

FIGURE 1.10: Evolution of deviatoric failure strength versus carbonated volume of oil-well cement paste for different confining pressure [33] [54]

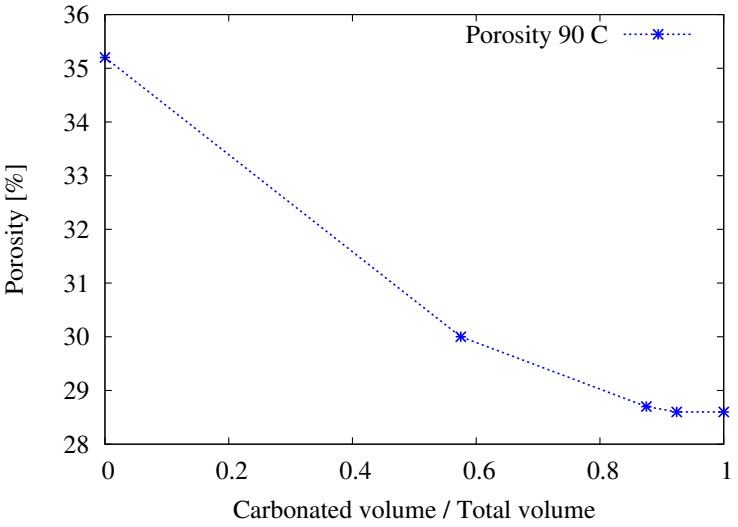

FIGURE 1.11: Water porosity versus carbonated volume of oil-well cement paste [33]

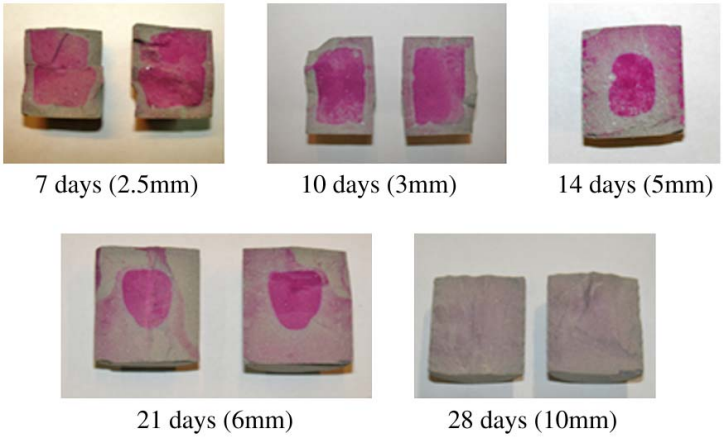

FIGURE 1.12: Evolution of carbonation depth of oil-well cement paste over time [33, 54]

Classically, the deviatoric failure stress increases with confining pressure due to internal frictional effect. It can be observed that, whatever the confining pressure, deviatoric strength increases with carbonated volume especially when the sample is completely carbonated. Moreover, the strength of samples tested in uniaxial compression and those tested in triaxial deviatoric compression with a confining pressure of 3 MPa are very close because the latter have also a pore pressure of 2.5 MPa. The effect of carbonation becomes more visible when the confining pressure reaches 10 MPa.

The formation of calcite that reduces the porosity and improves the binder properties, increases the deviatoric strength. The consequent carbonation shrinkage leads also to a confining of the non-carbonated inner part and thus contributes to the improvement of mechanical strength [33] (as it has been already reported in case of drying shrinkage [56]). The less marked increase in strength for intermediate carbonated volumes (3 and 6 mm) compared to completely carbonated volume (10 mm) comes from the heterogeneity

of the samples (completely carbonated zone, partially carbonated zone and sound zone). However, the effect of this heterogeneity becomes weaker when confining pressure reaches 10 MPa. The improvement of the homogeneity after complete carbonation obviously leads to a higher increase of strength [33]. Note that this increase does not seem to be detected by measurement of water porosity (see Fig. 1.11). Takla [33] also determined the values of Young's modulus during the multiaxial compression tests. The author observed that the evolution of the modulus with carbonation was similar to that of failure strength.

However, when the calcium hydroxide and alkali phases are depleted, the pH of the pore solution will be lower than 10.5 and the dominant specie is no longer carbonate [29, 30, 57]. This process leads to the leaching of the calcium and presence of only a porous silica gel [29, 30, 57]. Note that carbonation not only depends on the chemical environment, but also on the pressure [29, 58] and temperature increase [29].

Barlet-Gouédard et al. [23] carried out an experimental study on an oil cement paste to evaluate the effect of CO_2-rich environment (supercritical CO_2 and CO_2 saturated water). Pure water with pH of about 8 was used rather than saline solution to provide more severe conditions. The cubic samples were cured for three days at 20.7 MPa and 90°C, then after obtaining cylindrical samples to be tested by coring, these were conserved at 28 MPa and 90°C. The tests were carried out at room temperature after de-pressurization until atmospheric pressure. The authors observed an initial sealing due to the carbonation of the outer zone followed by its dissolution which started earlier in CO_2 saturated water. Such dissolution of calcite was also reported by others [22, 29, 30]. Barlet-Gouédard et al. [23] also observed that, after six weeks, the decrease in uniaxial compression strength of cement paste was higher in the case of the samples left in CO_2 saturated water compared to the case of supercritical CO_2. For the first environment, strength was not measurable anymore after six months due to high degree of sample deterioration. A degradation of triaxial mechanical strength due to acid environment was also reported by Fabbri and al. [24]. However, as the tests were carried out after de-pressurization to the atmospheric pressure and cooling down (which are not real downhole conditions), microcracks might appear and cause [59] or accentuate an important deterioration of the mechanical properties.

Furthermore, it is worth mentioning that, as indicated by Neville et al. [58], in down-hole conditions, the cement sheath can be altered by the formation water before the sequestration of CO_2 [58–60]. This would mean that the degraded cement paste is more representative in the case of old wells [58]. Indeed, the cement sheath must guarantee the isolation from the reservoir to the surface and between the surrounding geological formations [23] that contain fluids whose compositions are different from that of the

cement paste interstitial pore fluid [58, 60]. This difference in fluid compositions can lead to the alteration of the cement paste and thus to some leakage of formation fluids through degraded cement paste or rock-cement-casing interfaces [58, 60].

1.4 Lixiviation of Cement-Based Materials

Cement-based material is in equilibrium with its interstitial pore solution. However, when it is exposed to an aggressive solution, like deionised or acid water, chemical reactions take place leading to its lixiviation. Lixiviation indicates mainly the leaching of solid calcium phases of cement paste. It causes loss of bearing capacity and influences the durability of structures such as oil wells, underground radioactive waste storage facilities and etc.

1.4.1 Lixiviation process and factors influencing the leaching kinetics

Normal lixiviation or otherwise called simple lixiviation occurs in presence of pure or poorly mineralized water. Since cement paste pore solution is strongly basic (pH between 12.5 and 13.7) and contains chemical species with high concentrations [61], the weakly mineralized water (pH between 7 and 8.5) is an aggressive environment for it. Concentration gradients between the pore solution of cementitious material and the pure water leads to the diffusion of ions (alkalis, Ca^{2+}, OH^{-},...) toward the outside environment. Any change in the pore solution leads to a chemical readjustment process by dissolution/precipitation of solid phases which is assumed to be immediate compared to the diffusion process (hypothesis of local chemical equilibrium). Therefore, this process is controlled by the slowest phenomenon that is the diffusion process.

The calcium leaching is controlled by the thermodynamic equilibrium of the hydrates with pore solution. Fig. 1.13 presents the equilibrium giving the ratio of CaO/SiO_2 in function of calcium concentration of the solution [62]. It shows three different zones corresponding to the dissolution of various hydrated products [63]. The zone where the calcium concentration is about 22 mol/m^3 characterizes the balance of portlandite. This means that portlandite is stable in the cement paste only when the calcium concentration is high. The balance of the C-S-H phase is illustrated by the second zone corresponding to a calcium concentration between 2 and 22 mol/m^3. In this area, the Ca/Si of the solid can be attributed to a progressive decalcification of C-S-H. In the third zone where calcium concentration is between 0.3 and 1 mol/m^3, the structure of C-S-H is close to that of tobermorite [10] .

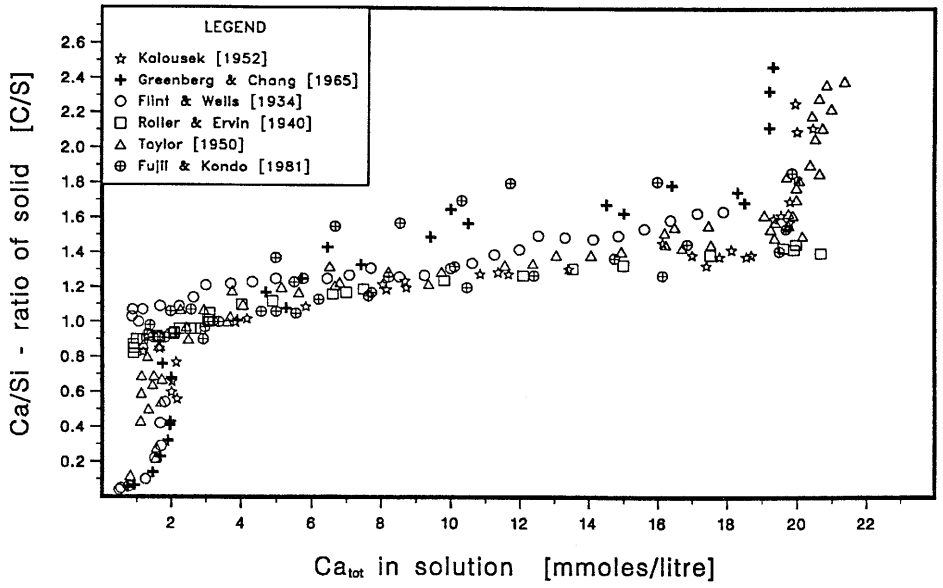

FIGURE 1.13: Equilibrium diagram between solid calcium/solid silica and calcium concentration in pore solution [62]

With the disruption of the balance that leads to the dissolution of hydrates, portlandite is the first one to dissolve [64, 65]. After its compelete leaching, the balance of the system is ensured by the C-S-H, which are then submitted, in their turn, to a gradual decalcification [64, 65]. Silica gels are the remaining products after the entire dissolution of C-S-H. According to Fick's laws, the degradation generally follows a linear law of square root of time as long as there is an unaltered zone and the chemical solution composition remains constant.

Additionally, the degradation kinetics is mainly governed by the pH of the aggressive solution. Lowering the pH increases the degradation kinetics but even at pH=4.5 the degradation kinetics with real chemical solutions, for instance slightly mineralized water, is generally low [65]. Therefore, different acceleration processes have been proposed in literature. Among them, one can mention for instance the electrochemical method [66] and the acid chemical solution injection [65]. In many works reported in literature, the ammonium nitrate NH_4NO_3 solution is largely used as the accelerating solution. Indeed, the chemical degradation caused by 6mol/l ammonium nitrate solution is 300 times higher than water at ambient temperature [67]. Note that the aggressiveness of the solution does not increase any more beyond 6mol/l. Such acceleration procedure is based on the assumption that the final consequence of chemical degradation on microstructure modification is the same for different solutions; the chemical nature of solution will only affect the degradation kinetics. However, the amount of the calcium leached by

accelerated lixiviation is higher than simple lixiviation for the same degradation depth [61]. Thus, accelerated degradation leads to higher impoverishment in calcium.

When cement paste is in contact with the ammonium nitrate solution of a pH near 5, ammonium diffuses into the material pores and reacts with the hydrated products leading to the modification of chemical equilibrium between the solid and liquid phase. The dissolution of the portlandite with NH_4NO_3 solution occurs according to the following reaction:

$$Ca(OH)_2 + 2NH_4NO_3 \rightleftharpoons Ca(NO_3)_2 + 2\overset{\uparrow}{N}H_3 + 2H_2O \tag{1.13}$$

The acceleration of degradation is amplified by the temperature increase [61, 68, 69], but the solubility of portlandite and C-S-H decreases. The calcium proportion passing into the solution increases as soon as the temperature changes from 20 to 50°C. For temperature ranging between 50 and 85°C, Kamali and al. [69] reported an increase in kinetics whereas Torrenti and al. [61] did not observe such an evolution. Moreover, the leaching kinetics also depends on material composition. It increases with water to binder (W/B) [69] or W/C ratio [70] leading to higher capillary porosity but decreases with the presence of cement additions, such as silica fume or fly ash, that reduces the amount of portlandite by forming additional C-S-H [69]. Besides, it is also observed that the degraded depth is almost similar for cement paste and mortar but decreases for concrete at a given leaching time [63, 71]: the presence of coarse aggregates delays the process of diffusion mainly due to the effect of tortuosity.

1.4.2 Influence on mechanical behavior

Many authors have been interested in the effect of lixiviation on the mechanical behavior of cement-based materials [54, 61, 63, 65, 67, 71–81]. Among them, Carde and al. [65, 72–74] have carried out an experimental study on a pure cement paste and cement paste with silica fume. The second mixture, obtained by the replacement of 30% cement by silica fume, was cast in order to distinguish the effect of portlandite $Ca(OH)_2$ and C-S-H on mechanical performances. The expected results after leaching were the total dissolution of portlandite and a progressive dissolution of the C-S-H for the first mixture, and progressive dissolution of the C-S-H only for the second one because the portlandite would have been consumed by the chemical reaction with silica fume to give new C-S-H. The pure cement paste had a W/C=0.5 while the paste with silica fume had a W/B= 0.45. After the maturation period in lime saturated water, because of the slowness of the degradation kinetics, the samples of smaller size, with diameter from 10 to 30 mm

and height/diameter ratio of 2, were obtained in the median part of larger samples by coring. A first series of samples was placed in an ammonium nitrate NH_4NO_3 solution (437g/l) while the second series (control samples) remained in the lime saturated water until testing.

Fig. 1.14 presents the evolution of mechanical behavior as a function of degradation rate (ratio of degraded cross section to total cross section) for samples with diameter of 30 mm. These results clearly show that the uniaxial compressive strength and elastic modulus decrease with chemical degradation. In addition, the initially brittle behavior becomes ductile with lixiviation. The strength and elastic modulus pass respectively from 56.5 to 14.6 MPa and from 15.8 to 5.85 GPa. As it can be seen in Fig. 1.15, the decrease in strength and the increase in porosity evolve linearly with the degradation of cement paste. This is also the case for the cement paste with silica fume, which means that there is a single law between loss of strength and porosity increase for any initial amount of portlandite [65, 73]. However, residual properties of materials depend on initial portlandite content.

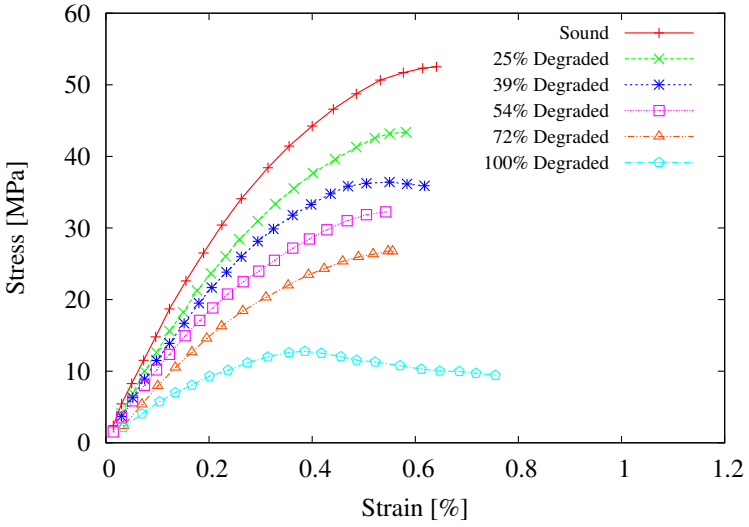

FIGURE 1.14: Stress-strain relationship of cement paste with W/C=0.50 in uniaxial compression for different levels of degradation [65]

Comparison of mechanical strength of cement paste with and without silica fume allowed distinguishing portlandite and C-S-H decalcification effects on mechanical strength. By modelling their tests, the authors concluded that for a total decrease of 76 % in uniaxial strength of cement paste without silica fume, 70% came from portlandite leaching and only 6% from C-S-H decalcification [65, 72, 73]. They also concluded that 2/3 of porosity increase was due to portlandite leaching and 1/3 to the C-S-H leaching [65, 73]. Therefore, il seems that there is an apparent contradiction as the influence of C-S-H leaching on mechanical strength remains weaker. However, as C-S-H leaching increases

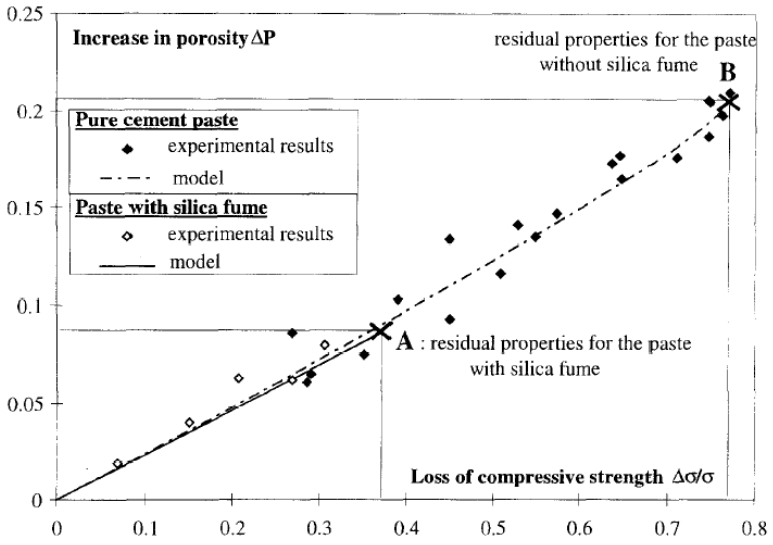

FIGURE 1.15: Evolution of the increase in water porosity as a function of the compressive strength decrease for a pure cement paste and a cement paste with silica fume [73]

micro-porosity, its influence on the failure strength remains moderate compared to portlandite leaching which induces a macro-porosity. Therefore, portlandite leaching is the main responsible cause of deterioration of uniaxial strength and Young's modulus, C-S-H leaching remains secondary in the case of a classical Portland cement paste. However, the influence of C-S-H leaching on strength becomes important when there is no longer portlandite in cement-based materials (case of cement paste containing silica fume), even if this material preserves overall its main properties [65, 72].

Moreover, the process of lixiviation (by ammonium chloride NH_4Cl solution) depends on W/C ratio [70]. The loss of strength increases with decrease of W/C ratio for a given rate of degradation. The authors explain this by an increase in portlandite content.

In order to evaluate the role of ITZ in the evolution of mechanical behavior with chemical degradation, Carde [65] has undertaken a new study on mortars similar to that on cement pastes. An ordinary mortar with W/C= 0.4 and a mortar with W/B= 0.4 and containing silica fume were poured for this study. The author observed that the variation in strength, elastic modulus and irreversible strains due to lixiviation were visibly more marked for ordinary mortar compared to ordinary cement paste. Such a difference did not exist between mortar and cement paste with silica fume, which indicates that the ITZ does not seem to play a particular role in this case. Therefore, these results confirm that the degradation of ITZ plays an important role in the modification of the mechanical properties of ordinary mortar, due to the dissolution of portlandite in the interfacial zone where it is abundant. This dissolution leads to a debonding between aggregates and ordinary paste cement [65]. The experimental study carried out by Le Béllego and

al. also highlights the negative effect of a chemical degradation by ammonium nitrate solution (6mol/l) on uniaxial [82] and flexural mechanical behavior of a mortar with W/C=0.4 [76, 82].

Mechanical behavior of cement paste and mortar were very often only considered in literature. More recently, Nguyen and al. [63, 71] have carried out an experimental study on the evolution of the mechanical behavior of a concrete with W/C=0.6. After 5 months of maturation in water, samples were placed in an ammonium nitrate solution (6mol/l). Two types of samples were used: fully cylindrical samples (ϕ=110 mm, h=220 mm) and hollow cylindrical samples with the same external dimensions and a centred hole of diameter (ϕ=27mm). The top and bottom faces of samples were protected in order to have only a radial leaching in the central part of samples. Fig. 1.16 shows the stress-strain curves of the hollow samples for different rate of degradation. It can be observed that the sound sample has an almost brittle behavior. This behavior becomes more and more ductile with higher strain as a function of lixiviation. The mechanical behavior is almost elastic perfectly plastic after an important period of leaching. After complete leaching, the strength and stiffness decrease by about 70 % and the mean strain at peak stress becomes almost three times higher compared to the sound state. The authors also carried out cyclic tests which illustrated the presence of considerable irreversible strains with degradation.

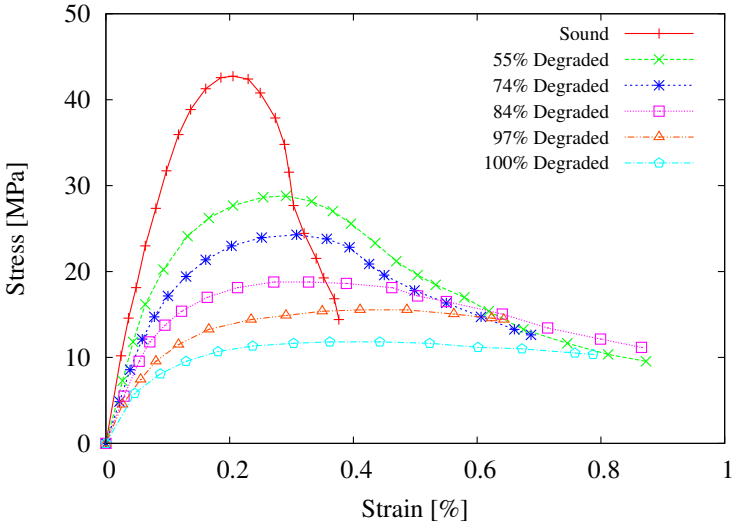

FIGURE 1.16: Stress-main strain relationship of concrete W/C=0.60 in uniaxial compression for different level of degradation (hollow cylinders) [71]

The triaxial mechanical behavior of mortar and cement paste in function of lixiviation was also examined in the literature. Here we present results obtained on the oil-well cement paste with W/C=0.44 within the framework of the project with TOTAL [78]. Note that this study was conducted before the evaluation of the effect of carbonation on this cement paste whose results were presented in the previous section. This study

on the effect of chemical degradation with an ammonium nitrate (NH_4NO_3) solution (6mol/l) under temperature of 90° has been carried out in order to simulate the case of complete degradation by an acid solution such as a carboxylic acid type or water charged in H_2S. The conditions of maturation were very close to those already presented for the study of carbonation. After the maturation phase, samples with a diameter of 37 mm and a height of 40 mm were separated into two series under 90°C: a first series was placed in a neutral fluid (a synthetic fluid that has similar composition to the interstitial fluid [78]) while the second series of samples was submitted to chemical degradation with ammonium nitrate (NH_4NO_3) solution until complete degradation. Samples of the second series were rinsed in distilled water before mechanical tests. Phenolphthalein was used to visualize the evolution of lixiviation.

The multi-axial performed compression tests showed that the behavior of cement paste at sound and chemically degraded states was characterized by a small elastic phase and a very important plastic phase at low confining pressure [78]. Further, even if there is larger elastic response in sound material when confining pressure reaches 10 MPa, the plastic deformation remains dominant with respect to the elastic one for the two materials. Fig. 1.17 presents the evolution of deviatoric failure strength (peak stress) versus effective confining pressure for sound and degraded materials. The deviatoric failure strength increases with effective confining pressure but such increase is attenuated by chemical leaching, going from 133 to 99%. This is correlated with porosity increase throughout degradation, from 37 to 56%. Due to the high porosity and ductile behavior, the oil cement paste both in sound and degraded states exhibits essentially compressive plastic volumetric strain. Further, the deviatoric failure stress of degraded samples reaches an asymptotic value after some threshold of confining pressure. Moreover, the failure strength of sound and degraded samples slightly increases after pre-confining (filled marks in the figure) due to preliminary compaction of material.

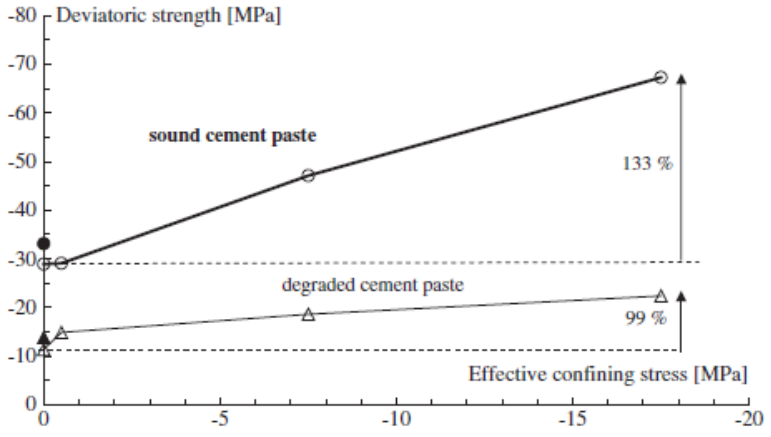

FIGURE 1.17: Multi-axial strength evolution of sound and degraded oil-well cement paste versus effective confining pressure [78]

Similar evolution of deviatoric strength with degradation in drained condition were also reported for the same oil-well cement paste [77] and for ordinary cement paste [67, 75, 80] and mortar [67, 75] with W/C=0.5 at ambient temperature. However, it has been observed that the deviatoric strength of ordinary cement paste or mortar remained constant with the increase of confining pressure in undrained condition [67, 75, 80] . This comes from the fact that the friction coefficient becomes almost zero in undrained condition. The degraded material is more sensitive to pore pressure than the sound material due to the increase of Skempton coefficient. Amplification of material sensitivity to pore pressure depends on two consequences of chemical damage: increase in porosity and decrease in the ratio of solid to fluid compressibility. The first is mainly due to Portlandite leaching while the second, also called intrinsic chemical damage, is due to the reduction in C/S ratio and has a dominating effect [67, 80].

The evolution of initial elastic modulus of sound and degraded materials versus effective confining pressure is presented in Fig. 1.18. Like failure strength, the elastic modulus also decreases with degradation. Moreover, the elastic modulus or more exactly elastic stiffness increases overall, with confining pressure. Elastic modulus of degraded sample determined from uniaxial compression test with pre-confining is higher than that of sample without pre-confining. The pre-confined sound sample should also have higher initial elastic modulus compared to sample without pre-confining (even if it could not be determined in the experimental study). This shows the effect of compaction due to pre-confining on initial elastic modulus. The decrease in elastic modulus, which tends from the sound material value to degraded one, is also reported in literature at ambient temperature [54, 61, 63, 65, 71, 72, 74, 76, 77, 79–81].

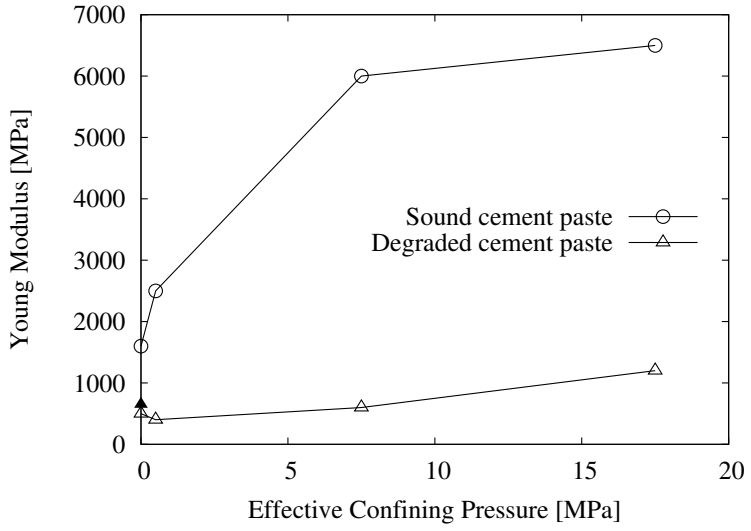

FIGURE 1.18: Young's modulus evolution of sound and degraded oil-well cement paste versus effective confining pressure [78]

Note that for all above presented mechanical tests performed to assess the effect of carbonation or lixiviation, the material can be considered homogeneous only when it is at sound or completely degraded state. For intermediate states, the sample is not homogeneous.

1.5 Conclusion

At the beginning of this chapter some generalities about cement-based materials such as hydration and porosity of cement paste, evolution of mechanical properties with hydration and effect of temperature, and specificity of the ITZ have been reviewed. Then, the process of carbonation and lixiviation and their effects on the microstructure and mechanical behavior of cement-based materials have been presented and analysed. As both of these chemical reactions have slow kinetics, accelerated methods have been used in order to understand different coupling phenomena. This is necessary to be able to evaluate the long term durability of cement-based materials used especially for radioactive waste storage or oil-well building for which the operational life may reach several thousands of years. It has been seen that generally carbonation decreases the porosity and improves mechanical properties of cement-based materials by the formation of calcite grains $CaCO_3$. Carbonation also leads to a transition from ductile to brittle behavior. However, lixiviation degrades the microstructure by leaching the calcium which is the key factor for the main properties of cement-based materials. This causes an increase of porosity that leads to a decrease of mechanical properties as well as a transition from brittle to ductile behavior. Based on experimental data presented in this chapter, an elastoplastic macroscopic model and micromechanics-based macroscopic models (micro-macro models) will be proposed in following chapters to take into account effects of the two above cited chemical degradations. Experimental data presented in this chapter will be used in order to calibrate model's parameters and to verify the capacity of the proposed models to reproduce the basic characteristics.

Chapter 2

Elastoplastic Macroscopic Model For Carbonation and Lixiviation of an Oil-Well Cement Paste

Contents

2.1 Introduction

Modeling the effects of carbonation and lixiviation on mechanical and transport properties of cement-based materials is crucial for long-term durability analysis of structures. In this chapter, an elastoplastic macroscopic constitutive model is proposed to describe the mechanical behavior of a petroleum cement paste (class "G" cement) under the effect of carbonation or lixiviation. Using a phenomenological model will help us identify influenced parameters by chemical degradations, in order to reveal relevant parameters governing the non-linear behavior of the studied material.

First, based on experimental investigations presented in previous section, an elastoplastic macroscopic model is introduced to reproduce the evolution of mechanical behavior up to the peak point of the stress-strain relationship. Then, an interface constitutive law is introduced in order to take into account the localization of deformations on a shear plane for modeling the post-peak behavior. Finally, a comparison between experimental data and numerical simulations is presented and the evolution of mechanical properties of cement paste versus chemical degradations is analysed.

2.2 Constitutive Model (pre-localization response)

Based on experimental investigations presented in the previous section, an elastoplastic model is proposed to simulate the before mentioned characteristics of sound and degraded cement paste. Chemical degradations change significantly material properties such as the elastic modulus, compressive strength and also ductility of the material. The assumptions of small strains and isothermal conditions are used throughout this study. As classically defined, the total strain tensor is decomposed into an elastic part $\boldsymbol{\varepsilon}^e$ and a plastic part $\boldsymbol{\varepsilon}^p$:

$$\boldsymbol{\varepsilon} = \boldsymbol{\varepsilon}^e + \boldsymbol{\varepsilon}^p, \qquad \dot{\boldsymbol{\varepsilon}} = \dot{\boldsymbol{\varepsilon}}^e + \dot{\boldsymbol{\varepsilon}}^p \tag{2.1}$$

The thermodynamic potential for this elastoplastic model can be expressed as follow:

$$\Psi = \frac{1}{2}(\boldsymbol{\varepsilon} - \boldsymbol{\varepsilon}^p) : \mathbb{C}^e : (\boldsymbol{\varepsilon} - \boldsymbol{\varepsilon}^p) + \Psi^p(\gamma^p) \tag{2.2}$$

Where $\Psi^p(\gamma^p)$ is the locked plastic energy due to plastic hardening and $\mathbb{C}^e$ is the fourth order elastic stiffness matrix of cement paste, assumed to be isotropic and is written in the general form:

$$\mathbb{C}^e = 3k\mathbb{J} + 2\mu\mathbb{K} \tag{2.3}$$

Where k and μ are positive scalars representing respectively the elastic bulk modulus and shear modulus. $\mathbb{J} = \frac{1}{3}\mathbf{1}\otimes\mathbf{1}$ and $\mathbb{K} = \mathbb{I} - \mathbb{J}$ represent respectively isotropic symmetric forth order spherical and deviatoric operators. $\mathbf{1}$ and $\mathbb{I}$ are respectively second and forth order symmetric identity tensors were $\mathbb{I}$ in symmetric conditions can be written as; $\mathbb{I}_{ijkl} = \frac{1}{2}(\boldsymbol{\delta}_{ik}\boldsymbol{\delta}_{jl} + \boldsymbol{\delta}_{il}\boldsymbol{\delta}_{jk})$. Derivation of thermodynamic potential by internal variable $\boldsymbol{\varepsilon}^e$ leads to the following state equation:

$$\boldsymbol{\sigma} = \frac{\partial \Psi}{\partial \boldsymbol{\varepsilon}^e} = \mathbb{C}^e : (\boldsymbol{\varepsilon} - \boldsymbol{\varepsilon}^p) \tag{2.4}$$

For most cohesive-frictional materials, the plastic response depends on three basic stress invariants. In order to provide a general mathematical formulation, the following stress invariants are introduced:

$$\begin{aligned} &I_1 = tr\boldsymbol{\sigma}, \quad \bar{\sigma} = \sqrt{J_2} \\ &\theta = \frac{1}{3}\sin^{-1}\left(-\frac{3\sqrt{3}}{2}\frac{J_3}{\bar{\sigma}^3}\right); \quad -\pi/6 \leq \theta \leq \pi/6 \\ &J_2 = \frac{1}{2}\boldsymbol{S}_{ij}\boldsymbol{S}_{ij}, \quad J_3 = det\bar{\bar{S}} = \frac{1}{3}\boldsymbol{S}_{ij}\boldsymbol{S}_{jk}\boldsymbol{S}_{kl} \end{aligned} \tag{2.5}$$

where θ represents the Lode angle and $\boldsymbol{S}_{ij} = \boldsymbol{\sigma}_{ij} - \sigma_m\boldsymbol{\delta}_{ij}$ denotes the stress deviator where, $\sigma_m = \frac{1}{3}tr\boldsymbol{\sigma}$

2.2.1 Yield surface

Based on existing experimental laboratory data on typical cement-based materials [83, 84], the mechanical behavior (yield and failure surface) of cementitious material are strongly pressure sensitive. In order to describe mechanical behaviors of these materials in a large range of stress (0 - 20 MPa confining pressure), it is necessary to define a non linear curved yield surface. The classical Mohr-Coulomb or Drucker-Prager type criteria are not suitable. Based on experimental results [33, 78], the quadratic form proposed by [1] is adapted here to describe the failure surface of cement paste.

$$\bar{F} = a_1\left(\frac{\bar{\sigma}}{g(\theta)f_c}\right) + a_2\left(\frac{\bar{\sigma}}{g(\theta)f_c}\right)^2 - \left(a_3 - \frac{I_1}{f_c}\right) = 0 \tag{2.6}$$

Where a_1, a_2 and a_3 are dimensionless material constants, whereas f_c represents uniaxial compressive strength of cement paste. These three parameters are used to determine the best fit calibration of failure surface with respect to existing laboratory experimental data. Various forms have been proposed for cement-based materials, for instance that by [85]. A specific form could be chosen based on experimental failure stresses in the

deviatoric plane. The failure surface is considered as the ultimate state of subsequent yield surfaces. The function $g(\theta)$ defines the best dependency of the failure surface on the Lode angle. The experimental data were performed on classical triaxial tests on cylindrical samples, so that $\sigma_2 = \sigma_3$. Hence, the effect of the lode angle is negligible. Therefore, for the sake of simplicity we take $g(\theta) = 1$. By taking a plastic hardening law, the yield surface can be described by the following functional form:

$$\begin{aligned} F &= \bar{\sigma} - \beta(\gamma^p)\bar{\sigma}_c = 0 \\ \bar{\sigma}_c &= \frac{-a_1 + \sqrt{a_1^2 + 4a_2(a_3 - \frac{I_1}{f_c})}}{2a_2} f_c \end{aligned} \tag{2.7}$$

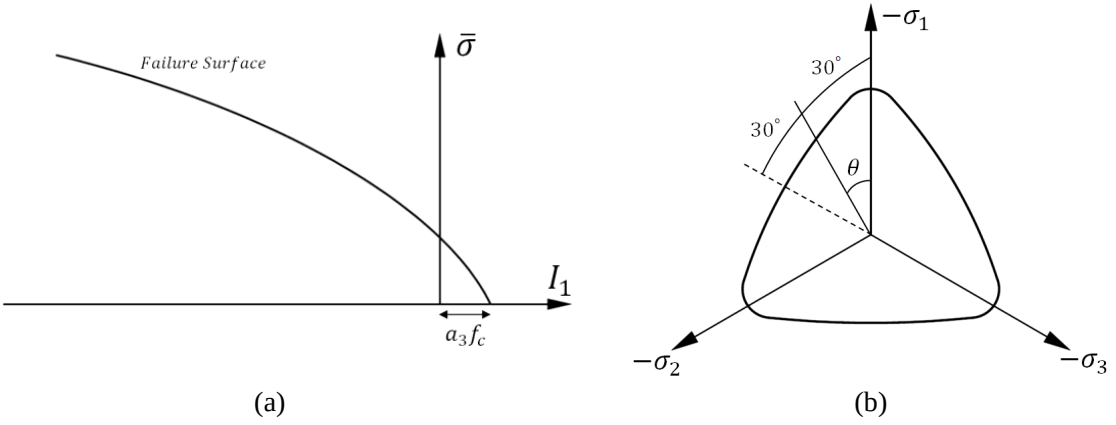

FIGURE 2.1: Failure envelope in (a) meridional plane (b) deviatoric plane (π-plane)

where the function $\beta(\gamma^p)$ represents the plastic hardening law of material and takes the value of 0 for elastic behavior to 1 when completely plastified. The internal hardening variable, noted by γ^p, is taken to be the cumulated plastic distortion defined in (2.8).

$$\gamma^p = \int d\gamma^p, \qquad d\gamma^p = \sqrt{d\boldsymbol{e}^p_{ij} d\boldsymbol{e}^p_{ij}}/\chi_p, \qquad d\boldsymbol{e}^p_{ij} = d\boldsymbol{\varepsilon}^p_{ij} - \frac{1}{3} d\boldsymbol{\varepsilon}^p_{kk} \boldsymbol{\delta}_{ij} \tag{2.8}$$

The plastic hardening law of cement paste is also strongly dependent on confining pressure in compression. For example, the value of axial strain at failure (peak point) state increases significantly with confining pressure. In order to account for this pressure sensitivity, a regularizing coefficient χ_p has been introduced in (2.8), which is a function of the effective mean stress.

$$\chi_p(I_1) = \left(a_3 - \frac{I_1}{f_c}\right)^n \tag{2.9}$$

where n is a model parameter. It's been assumed that the plastic deformation does not produce material softening behavior. Therefore, a fully positive hardening law with a hyperbolic form is proposed. The following relation is determined:

$$\beta(\gamma^p) = \frac{\gamma^p}{B + \gamma^p} \tag{2.10}$$

where parameter B is a positive scalar value which constrols the kinematics of hardening. For instance if B holds a very small value $B \to 0$ then $\beta(\xi) \to 1$, it is as if the material has an elastic perfectly plastic behavior as shown in Fig. 2.2.

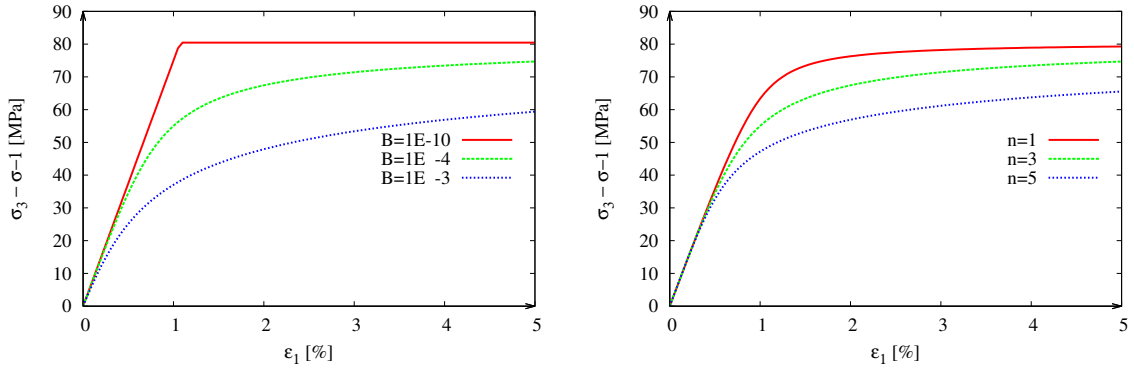

(a) Effect of Parameter B

(b) Effect of Parameter n

FIGURE 2.2: Effect of paremeters B and n

It should be noted that, according to (2.10), $\beta(\gamma^p) \to 1$ when $\gamma^p \to \infty$, which implies that the yield surface asymptotically approaches the failure surface. On the other hand, $\beta(\gamma^p) = 0$ for $\gamma^p = 0$, which indicates that, in the proposed approach, the initial yield surface is reduced to zero.

2.2.2 Plastic potential

The volume strain during plastic flow depends on applied stress state. There is a transition from plastic compressibility to dilatancy. A similar trend is also observed in certain geological materials and can adequately be modelled by assuming a non-associated flow rule and defining an appropriate form of the plastic potential [86]. Recognizing this analogy, the plastic potential proposed by [1] is adopted:

$$G = \bar{\sigma} + \eta_c g(\theta) \bar{I} \ln\left(\frac{\bar{I}}{\bar{I}_0}\right), \qquad \bar{I} = a_3 f_c - I_1 \tag{2.11}$$

where $\bar{I}_0$ defines the intersection of the plastic potential surface with the $\bar{I}$ axis. The transition from compressibility to dilatancy occurs at the points coinciding with $\frac{\partial G}{\partial I} = 0$. Based on experimental data, it is assumed that the transition points can be approached by a linear relation. The parameter η_c is the slope of the transition line between compressibility and dilatancy as shown in Fig. 2.3.

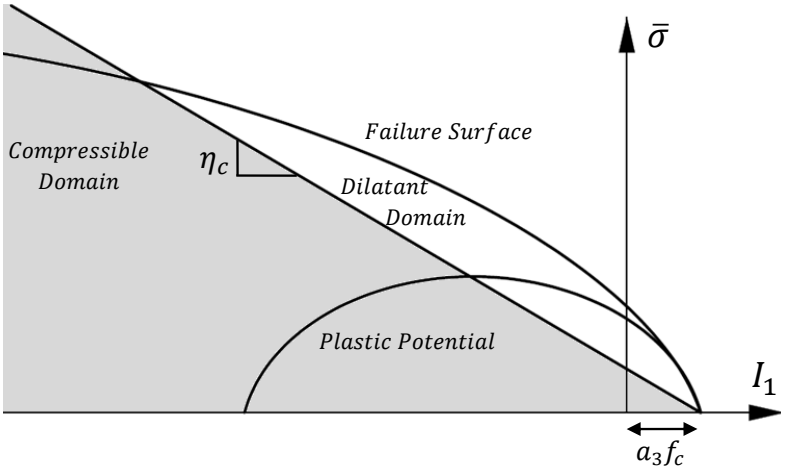

FIGURE 2.3: Illustration of compressibility/dilatancy boundary, failure surface and plastic potential

2.2.3 Mathematical model formulation

Considering the generalized Hook's law, the incremental form of the state equation can be written as:

$$\dot{\boldsymbol{\sigma}}_{ij} = \mathbb{C}^e_{ijkl}(\dot{\boldsymbol{\varepsilon}}_{kl} - \dot{\boldsymbol{\varepsilon}}^p_{kl}) \tag{2.12}$$

In any loading path, it is not possible to exceed the boundary of $F(\boldsymbol{\sigma}, \gamma^p)$, for this reason a consistency condition ($\dot{F} = 0$) has to be verified as expressed here:

$$\dot{F}(\boldsymbol{\sigma}, \gamma^p) = \frac{\partial F}{\partial \boldsymbol{\sigma}_{ij}}\dot{\boldsymbol{\sigma}}_{ij} + \frac{\partial F}{\partial \beta}\frac{d\beta}{d\gamma^p}\dot{\gamma}^p = 0 \tag{2.13}$$

The plastic flow rule which defines the direction and magnitude of plastic strain rate is introduced as follow.

$$\dot{\boldsymbol{\varepsilon}}^p_{ij} = \dot{\lambda}\frac{\partial G}{\partial \boldsymbol{\sigma}_{ij}} \tag{2.14}$$

The plastic potential is used to define the direction of the rate of change of the plastic strain tensor. The Plastic Multiplier ($\dot{\lambda}$) is a scalar value defining the magnitude of the

plastic flow rule. The Plastic Multiplier can be calculated by substituting (2.12) into (2.13) by using (2.8), as following:

$$\dot{\lambda} = \frac{\frac{\partial F}{\partial \boldsymbol{\sigma}_{ij}} \mathbb{C}^e_{ijkl} \dot{\boldsymbol{\varepsilon}}_{kl}}{H_e + H_p} \tag{2.15}$$

$$\begin{aligned} H_p &= -\frac{\partial F}{\partial \beta} \frac{d\beta}{d\gamma^p} \frac{\sqrt{d\boldsymbol{e}^p_{ij} d\boldsymbol{e}^p_{ij}}}{\chi_p} \\ H_e &= \frac{\partial F}{\partial \boldsymbol{\sigma}_{pq}} \mathbb{C}^e_{pqrs} \frac{\partial G}{\partial \boldsymbol{\sigma}_{rs}} \end{aligned} \tag{2.16}$$

By implementing this formulation with the Modified Newton-Raphson method (MNR), due to the reason that the tangential stiffness matrix is formed at the beginning of each step and is used in all iterations, a fast convergence is assured.

In order to have more precise results with less iterations, the classical Newton-Raphson (NR) method is suggested, which implies the use of the elastoplastic stiffness matrix to be formed at each iteration in a particular step. The convergence of the NR method takes more time but insures less iterations. The rate form of the constitutive equation can then be expressed as:

$$\dot{\boldsymbol{\sigma}} = \mathbb{C}^{ep} : \dot{\boldsymbol{\varepsilon}} \tag{2.17}$$

where $\mathbb{C}^{ep}$ is the tangent elastoplastic stiffness matrix and is calculated by substituting the plastic multiplier found in (2.15) in the incremental form of the Hook's law.

$$\begin{aligned} \dot{\boldsymbol{\sigma}} = \frac{\partial \Psi}{\partial \boldsymbol{\varepsilon}^e} &= \mathbb{C}^e : (\dot{\boldsymbol{\varepsilon}} - \dot{\boldsymbol{\varepsilon}}^p), \quad \dot{\boldsymbol{\varepsilon}}^p = \dot{\lambda} \frac{\partial G}{\partial \boldsymbol{\sigma}} \\ &= \mathbb{C}^e : \dot{\boldsymbol{\varepsilon}} - \dot{\lambda} \mathbb{C}^e \frac{\partial G}{\partial \boldsymbol{\sigma}} \\ &= \mathbb{C}^e : \dot{\boldsymbol{\varepsilon}} - \frac{\left(\mathbb{C}^e : \frac{\partial F}{\partial \boldsymbol{\sigma}}\right) \otimes \left(\mathbb{C}^e : \frac{\partial G}{\partial \boldsymbol{\sigma}}\right)}{H_e + H_p} : \dot{\boldsymbol{\varepsilon}} \end{aligned} \tag{2.18}$$

Where;

$$\mathbb{C}^{ep} = \begin{cases} \mathbb{C}^e & if \quad F(\boldsymbol{\sigma}, \gamma^p) \leq 0, \ \dot{F}(\boldsymbol{\sigma}, \gamma^p) < 0 \\ \mathbb{C}^e - \dfrac{\left(\mathbb{C}^e : \frac{\partial F}{\partial \boldsymbol{\sigma}}\right) \otimes \left(\mathbb{C}^e : \frac{\partial G}{\partial \boldsymbol{\sigma}}\right)}{H_e + H_p} & if \quad F(\boldsymbol{\sigma}, \gamma^p) = 0, \ \dot{F}(\boldsymbol{\sigma}, \gamma^p) = 0 \end{cases} \tag{2.19}$$

More information on the Integration algorithm of this model is given in Appendix A.

2.3 Numerical Simulations of the Effects of Chemical Degradations

The main objective of this part is to evaluate predictive capabilities of the proposed model and its abilities to reproduce the mechanical behavior of sound and degraded samples under various loading path. For this purpose, the model parameters involved were determined through a series of triaxial compression tests performed with different confining pressure. The proposed model contains two elastic parameters, four parameters describing the failure envelope and three plastic parameters describing the kinetics of hardening, pressure sensitivity and transition from contractant to dilatant behavior. Parameters related to the failure surface are obtained from the peak point of experimental stress-strain curves and the other ones are determined by numerical fitting with respect to experimental data.

As indicated above, the main concern of this part is to emphasize on the evolution of elastoplastic behavior and strength properties of chemical degradations due to carbonation or lixiviation reactions up to the peak point of the stress-strain relationship. The post-peak is motivated from different physical phenomenon apart from the ones stated here and should be treated otherwise by introducing another constitutive law to take into account the localization of deformations on a shear plane.

2.3.1 Numerical simulations of carbonation effects

Numerical simulations performed in the present study are based on experimental data obtained by [33, 54] on an oil-well cement paste (see section 1.3.7.2). Table 2.1 presents the set of parameters used for numerical simulations performed on different states of carbonation. As it can be seen, all elastic and plastic parameters are kept constant except E, a_2 and f_c which change through carbonation. Fig. 2.4 shows that the change of a_2 and f_c parameters reflect the significant dependants of the failure envelope to the formation of calcite grains. This figure illustrates a good concordance between numerical

and experimental results indicating that the effects of carbonation and confining pressure are correctly taken into account.

Parameters	Sound	Carbonated		
		3mm	6mm	10mm
Elastic				
E [MPa]	2800	5000	5900	6100
ν	0.2	0.2	0.2	0.2
Plastic				
B	5×10^{-6}	5×10^{-6}	5×10^{-6}	5×10^{-6}
a_1	1.6	1.6	1.6	1.6
a_2	1.2	0.9	0.8	0.7
a_3	0.2	0.2	0.2	0.2
f_c [MPa]	27	33	41	67
n	3	3	3	3
η_c	0.55	0.55	0.55	0.55

TABLE 2.1: Set of Parameters from sound state to completely carbonated state

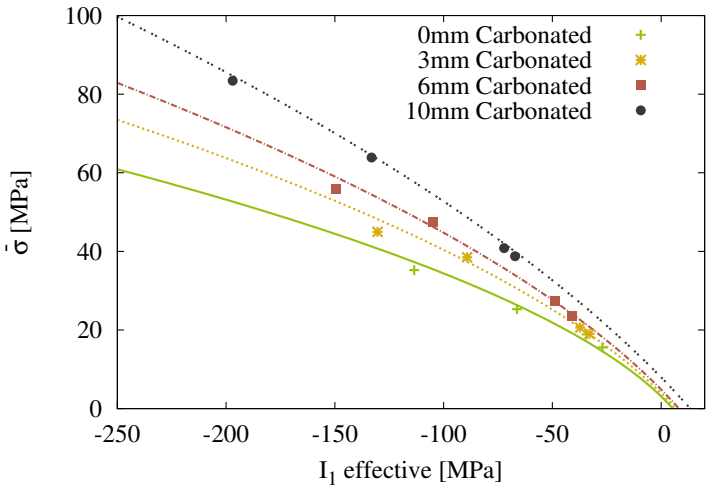

FIGURE 2.4: Failure Envelope evolution from sound state to completely carbonated state

The evolution of the above mentioned three parameters can be assumed as a function of carbonation rate (C_r) and expressed as follows:

$$E = \frac{E_0}{1 - \alpha_1 C_r} \; ; \quad f_c = \frac{f_{c0}}{1 - \alpha_2 C_r} \; ; \quad a_2 = \frac{a_{20}}{1 + \alpha_3 C_r} \tag{2.20}$$

where E_0, a_{20} and f_{c0} are the initial values without carbonation effect. α_1, α_2 and α_3 whose values are given in table 2.2 define the progressive change of parameters during carbonation.

Fig. 2.5 presents variation of normalized parameters E, f_c and a_2 with respect to carbonation rate where the filled marks and dotted lines correspond to experimental values

α_1	α_2	α_3
0.6	0.35	0.7

TABLE 2.2: Values of parameters controlling chemical damage effects

and the value obtained by (2.20). As previously mentioned, this is due to the decrease of porosity that leads to an increase of the solid phase volume and also to the higher elastic modulus of calcite grains (≈95 GPa), in comparison with portlandite (≈42 GPa) and C-S-H (≈22 GPa) [87]. However, the parameter a_2 decreases with carbonation. By looking again at (2.6) it becomes evident that a_2 parameter plays with the curvature of the failure surface. When a_2 tends to zero ($a_2 \to 0$) the failure surface becomes steeper. Physically said, when a_2 decreases the material becomes more brittle.

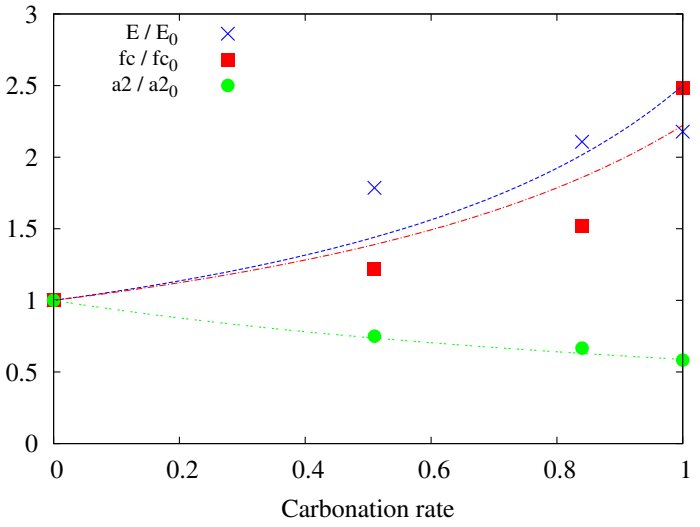

FIGURE 2.5: Evolution of parameters during carbonation

Fig. 2.6 to Fig. 2.9 present comparisons between numerical predictions and experimental data which are satisfactory. Note that these comparisons show only a verification of consistency of parameters as these experimental results have been also used for the determination of model's parameters.

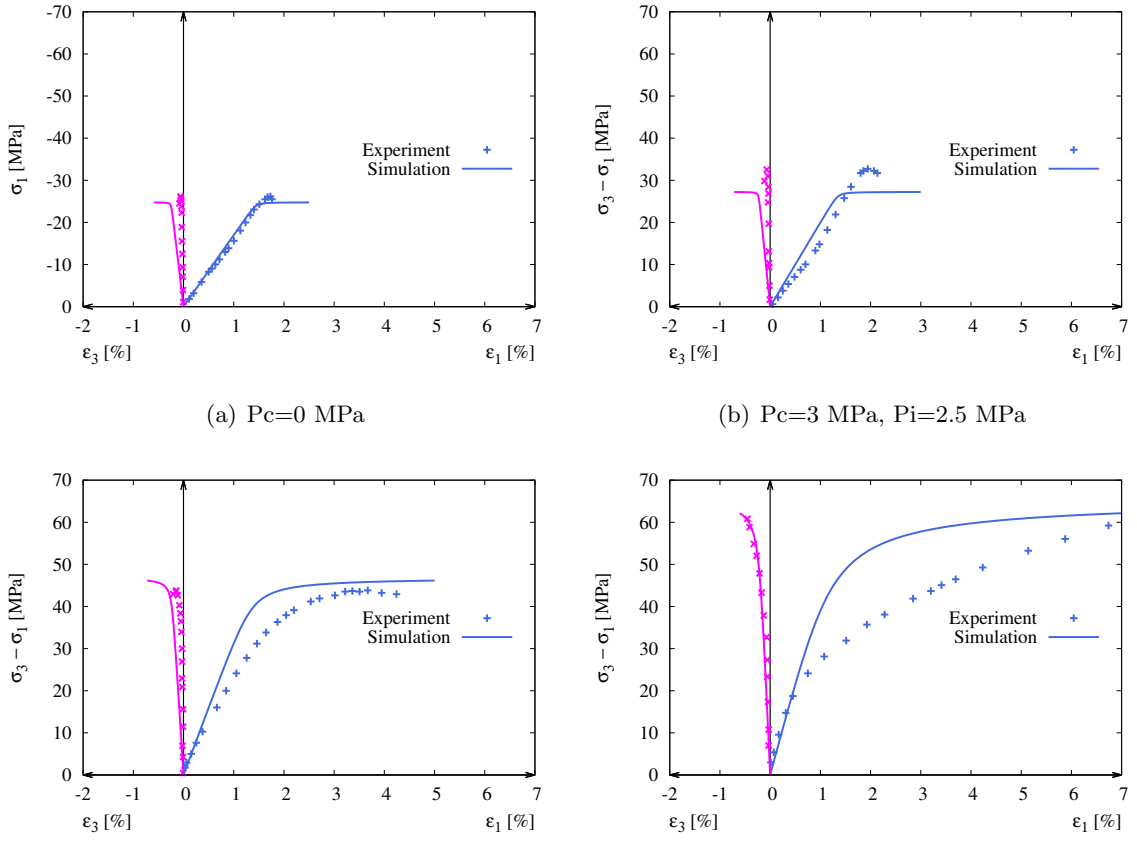

(a) Pc=0 MPa

(b) Pc=3 MPa, Pi=2.5 MPa

(c) Pc=10 MPa, Pi=2.5 MPa

(d) Pc=20 MPa, Pi=2.5 MPa

FIGURE 2.6: Uniaxial and Triaxial compression tests for sound samples ($\phi = 20\text{mm}, h = 22\text{mm}$) at different confining pressures

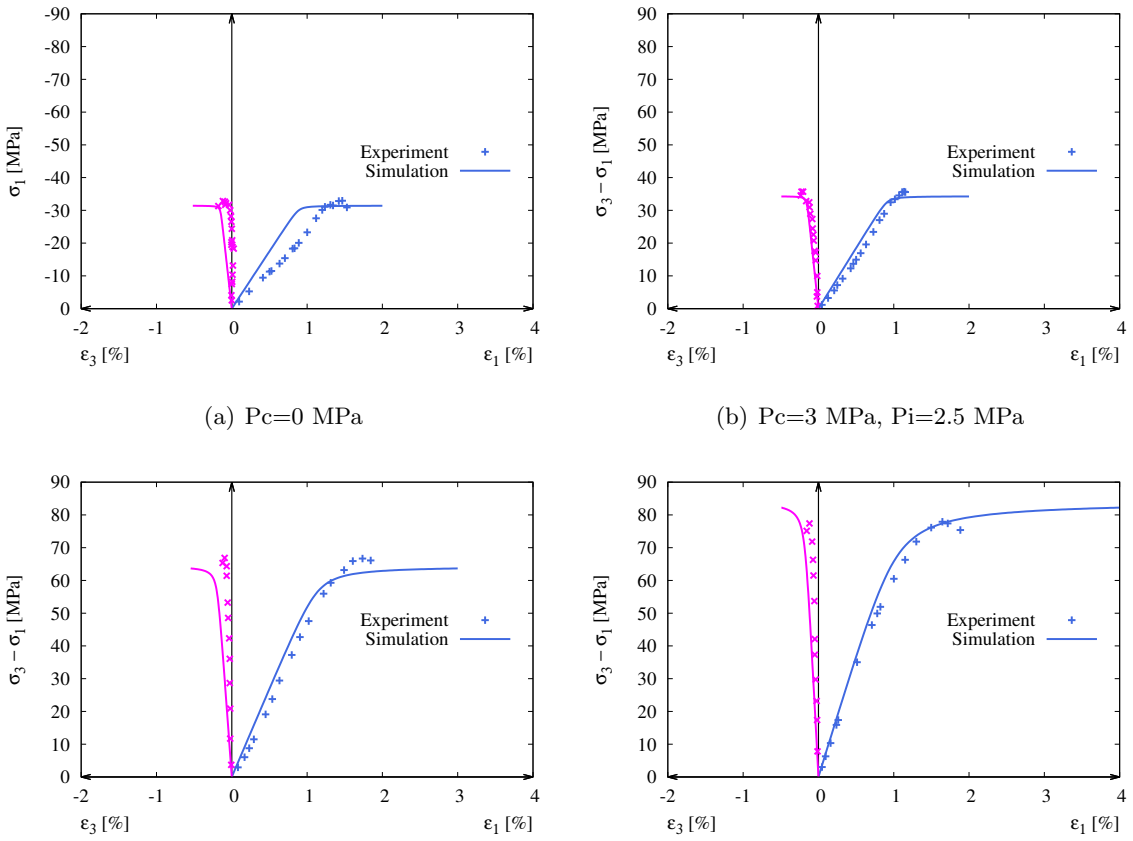

(a) Pc=0 MPa

(b) Pc=3 MPa, Pi=2.5 MPa

(c) Pc=10 MPa, Pi=2.5 MPa

(d) Pc=20 MPa, Pi=2.5 MPa

FIGURE 2.7: Uniaxial and Triaxial compression tests for 3mm carbonated samples ($\phi = 20\text{mm}, h = 22\text{mm}$) at different confining pressures

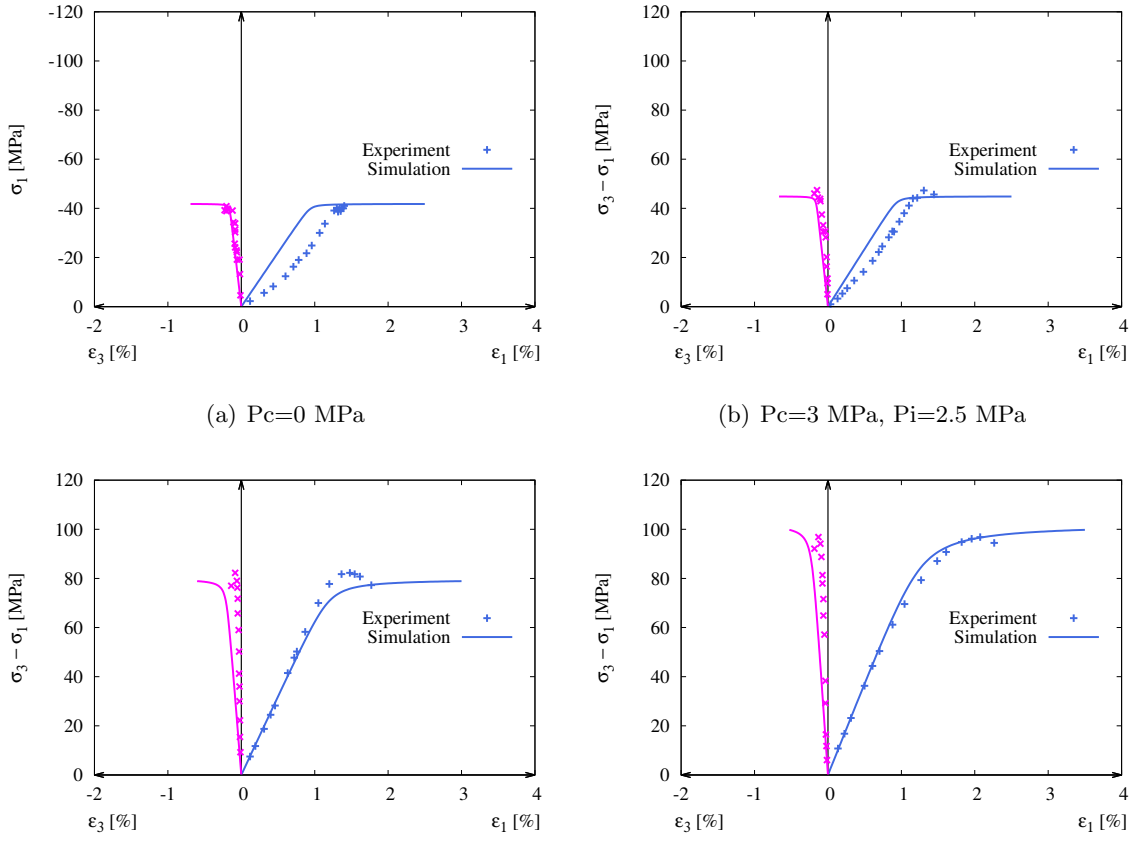

(a) Pc=0 MPa

(b) Pc=3 MPa, Pi=2.5 MPa

(c) Pc=10 MPa, Pi=2.5 MPa

(d) Pc=20 MPa, Pi=2.5 MPa

FIGURE 2.8: Uniaxial and Triaxial compression tests for 6mm carbonated samples ($\phi = 20\text{mm}, h = 22\text{mm}$) at different confining pressures

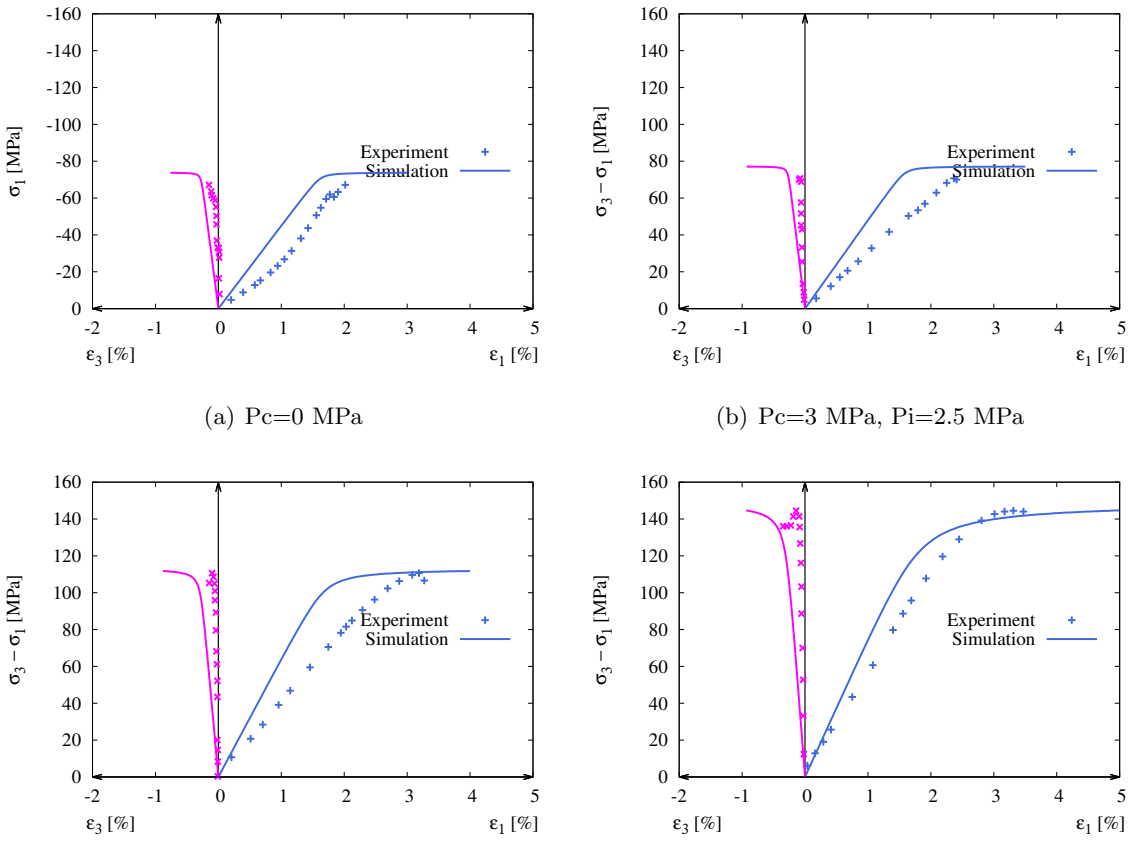

(a) Pc=0 MPa

(b) Pc=3 MPa, Pi=2.5 MPa

(c) Pc=10 MPa, Pi=2.5 MPa

(d) Pc=20 MPa, Pi=2.5 MPa

FIGURE 2.9: Uniaxial and Triaxial compression tests for 10mm carbonated samples ($\phi = 20\text{mm}, h = 22\text{mm}$) at different confining pressures

2.3.2 Numerical simulations of lixiviation effects

Numerical simulations performed in the present study are based on experimental data obtained by [78] on an oil-well cement paste (see section 1.4.2). Table 2.3 presents the set of parameters used for numerical simulations performed on sound and totally leached samples. Again, all parameters were taken constant except E, a_2 and f_c.

Parameters	Sound	Degraded
Elastic		
E [MPa]	4000	1000
ν	0.2	0.2
Plastic		
B	1.75×10^{-6}	1.75×10^{-6}
a_1	0.5	0.5
a_2	2.2	3.0
a_3	0.2	0.2
f_c [MPa]	28	11
n	1.5	1.5
η_c	0.5	0.5

TABLE 2.3: Set of Parameters from sound to totally leached state

Fig. 2.10 shows the significant deterioration of mechanical properties due to porosity increase by calcium leaching. Again one can observe a good agreement between numerical predictions and experimental results.

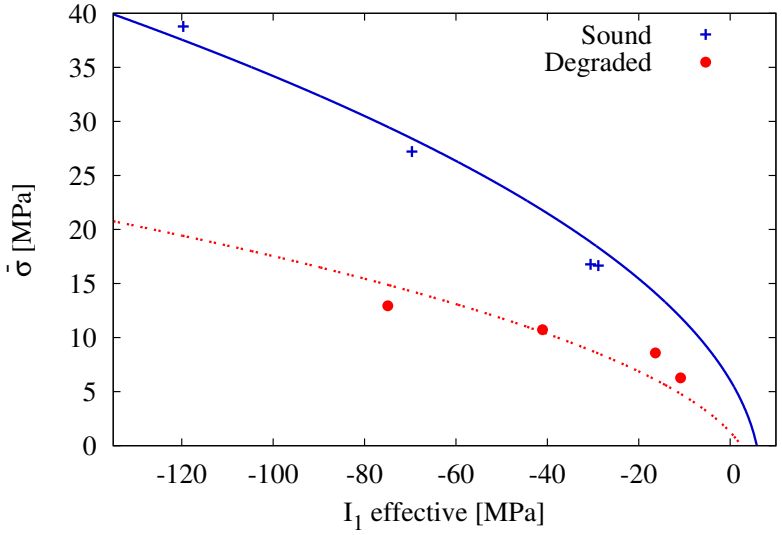

FIGURE 2.10: Failure Envelope evolution from sound state to completely leached state

Lixiviation affects, like carbonation, E, f_c and a_2 parameters. In the absence of mechanical damage, changes of material properties depend on the chemical damage variable d_c.

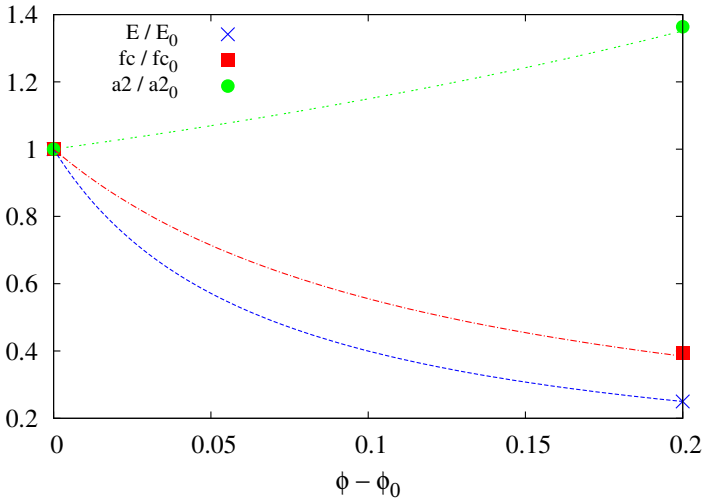

FIGURE 2.11: Evolution of parameters during lixiviation with respect to the increase of porosity

Here, the chemical damage variable d_c can be assumed as the difference between the porosity of sound and leached samples. Inspired by relevant micromechanical analysis on elastic properties of voided materials (Nemat-Nasser and Horri 1993), the following relations can be used to assess the evolution of parameters during leaching.

$$E = \frac{E_0}{1+\beta_1 d_c} \; ; \quad f_c = \frac{f_{c0}}{1+\beta_2 d_c} \; ; \quad a_2 = \frac{a_{20}}{1-\beta_3 d_c} \tag{2.21}$$

where E_0, a_{20} and f_{c0} are values of sound material. β_1, β_2 and β_3 define the progressive change of parameters due to chemical leaching. Their values are determined (table 2.4) from the sound and completely degraded states, as there were only these two particular states that were experimentally evaluated. Fig. 2.11 presents variation of normalized parameters E, f_c and a_2 with chemical damage. Normalized Young's modulus and uniaxial strength show a clear deterioration with calcium leaching. The latter leads to an increase of a_2 parameter which, as discussed earlier, controls the curvature of the failure envelope. The increase of this parameter engenders a more curved failure envelope which physically speaking means that the material becomes more ductile with lixiviation.

β_1	β_2	β_3
15	8	1.3

TABLE 2.4: Values of parameters controlling chemical damage effects

Comparisons between numerical simulations and experimental data are shown in Fig. 2.12 and Fig. 2.13. A good agreement is obtained for axial and lateral strains.

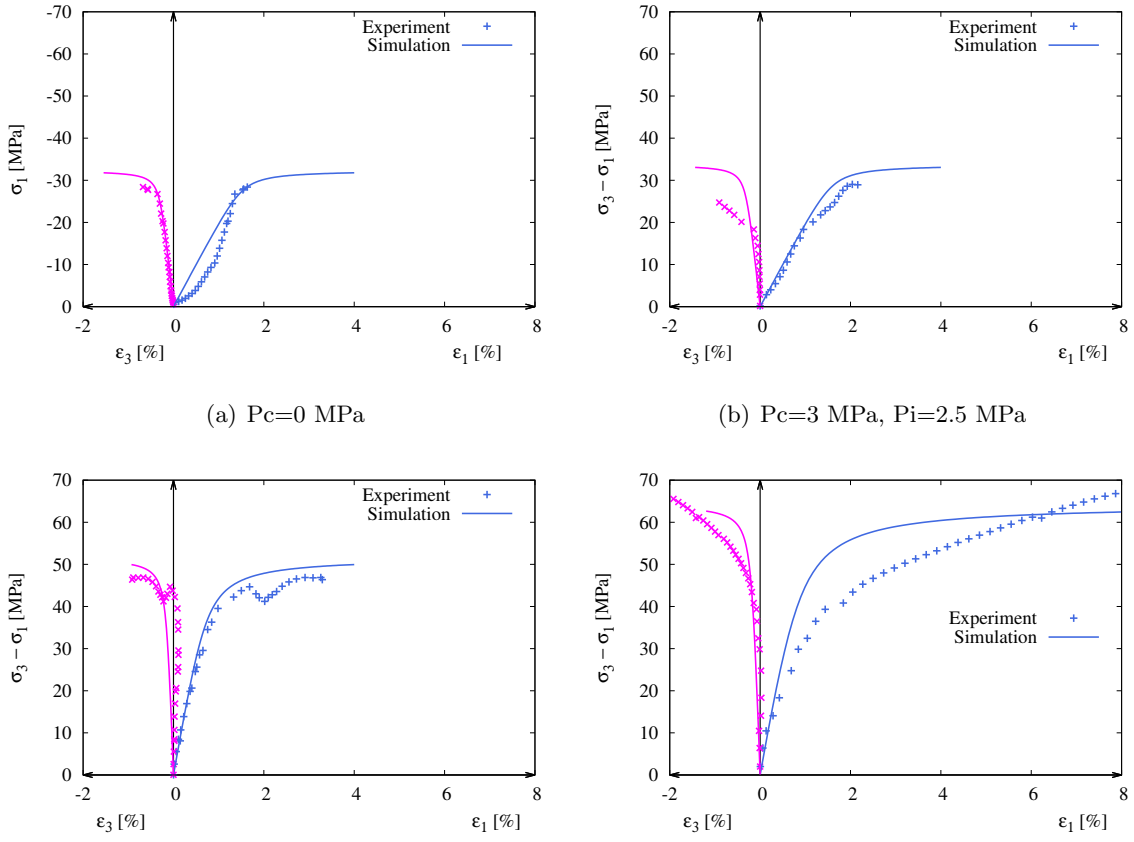

(a) Pc=0 MPa

(b) Pc=3 MPa, Pi=2.5 MPa

(c) Pc=10 MPa, Pi=2.5 MPa

(d) Pc=20 MPa, Pi=2.5 MPa

FIGURE 2.12: Uniaxial and Triaxial compression tests sound samples ($\phi = 36$mm$, h =$ 40mm) at different confining pressure

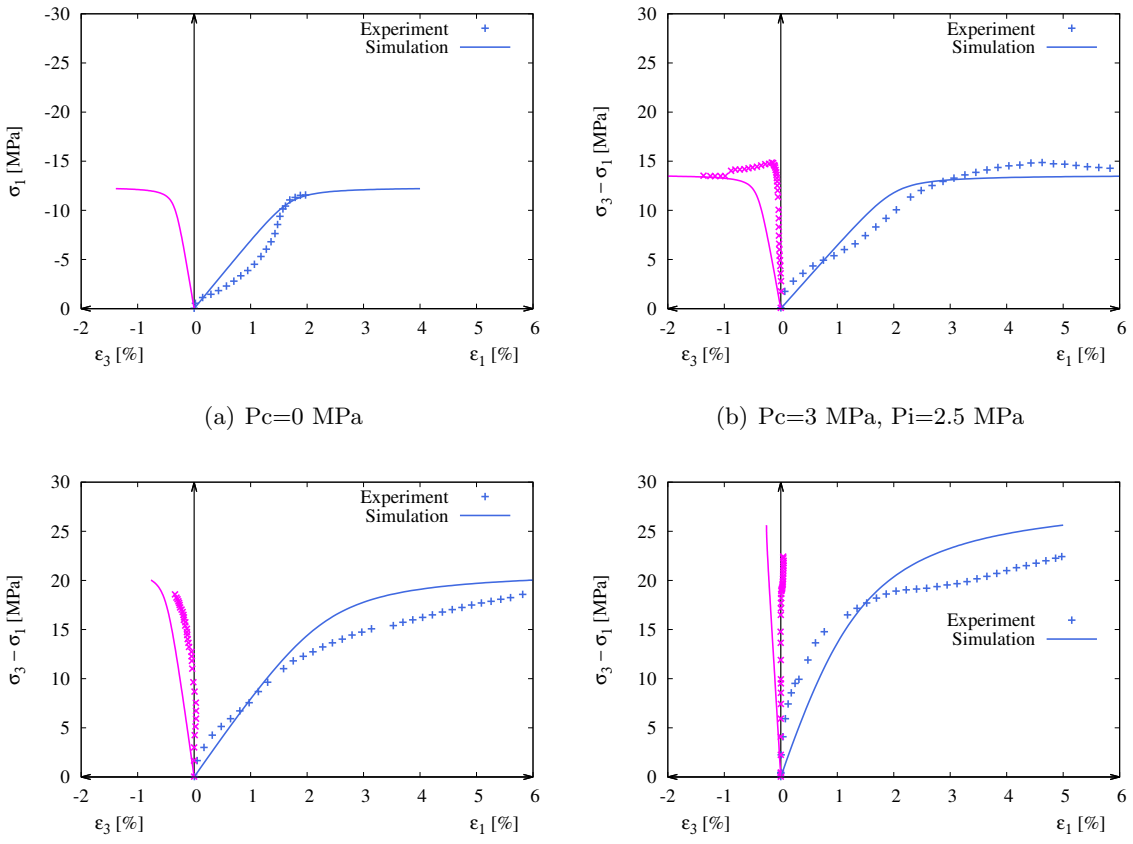

(a) Pc=0 MPa

(b) Pc=3 MPa, Pi=2.5 MPa

(c) Pc=10 MPa, Pi=2.5 MPa

(d) Pc=20 MPa, Pi=2.5 MPa

FIGURE 2.13: Uniaxial and Triaxial compression tests for totally leached samples ($\phi = 36\text{mm}, h = 40\text{mm}$) at different confining pressure

2.4 Strain Localization

In order for a constitutive model to reproduce general aspects that geomaterials normally exhibit, it should be able to consider:

- highly non-linear pre-peak stress-strain relation
- non associated plastic flow rule for contractant-dilatant behavior
- shear banding for post-peak strain softening

Shear banding is a very common phenomenon in geomaterials, the process which gives rise to shear bands is known as "strain localization". Strain localization is frequently observed in geomaterials and is considered an important precursor of soil failure and relevant geostructures including major geohazards such as landslides and debris flow. Due to its clear importance, relevant studies on strain localization, both experimentally and theoretically, have been an active area in geomechanics for decades (see [88–90]). These studies identified the following key factors which influence strain localization, including the confining pressure, boundary conditions, sample size, imperfection conditions.

According to experimental observations, the deformation process is diffuse at first, and then tends to concentrate in narrow zones called shear bands. As shown schematically in Fig. 2.14, this is essentially due to nucleation and propagation of microcracks created under loading which then form a narrow shear band with concentrated shear strain at failure stages. A smooth displacement pattern is formed involving highly localized deformations.

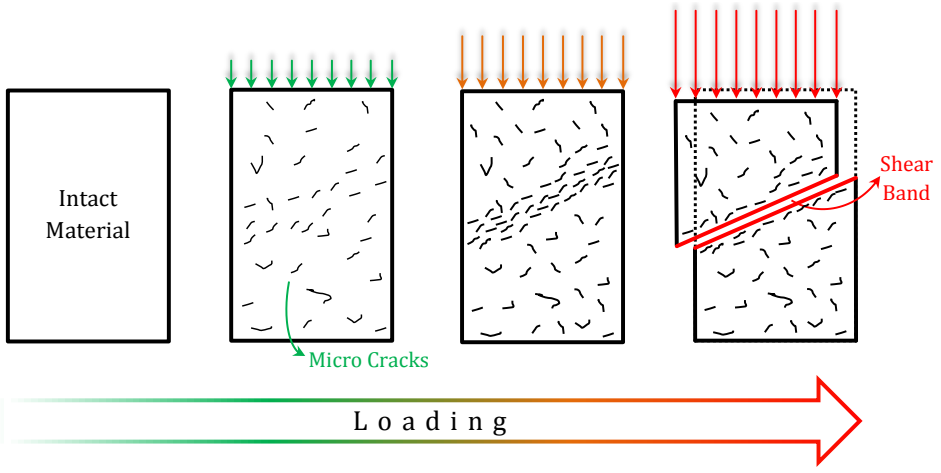

FIGURE 2.14: Formation of shear band during loading

Laboratory tests on granular material have demonstrated the formation of shear band during experimentations [91, 92] (see Fig. 2.15).

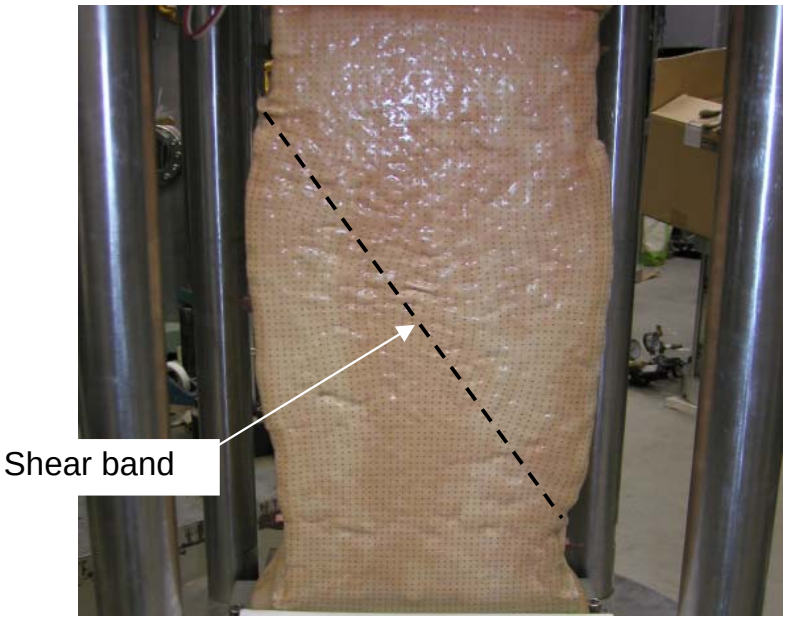

FIGURE 2.15: Shear band formation during plane strain test [91]

Strain localization is generally considered to be important as a presage of failure. It represents the instability corresponding to an abrupt loss of deformations homogeneity after the maximum load has been reached. When heterogeneities start to appear, the whole structure enters into the failure phase, this phase being often called "strain softening". From a mathematical point of view, this is due to a loss of positively defined value of the material tangent operator, associated with the change in type of governing field equation [93].

2.5 Constitutive Model (post-localization response)

Solutions of boundary value problems involving strain softening material property have serous difficulties from both modeling of strain localization, numerical and mathematical point of view. A variety of constitutive models have been proposed to simulate strain localization. Although stress-strain damage models with strain softening behavior used in a standard continuum mechanics demonstrate good predictions, they also lead to physically meaningless results and the numerical solution suffers by a pathological sensitivity to the finite element discretization. In addition, local microcrack parameters are not taken into account either. Moreover, using straightforward strain softening model in a classical continuum mechanics does not result in a well posed problem. As a result, the field equations that describe the motion of the body lose ellipticity and become hyperbolic as soon as strain softening occurs. Hence, there is no thickness for the localized line and the energy consumption in that zone remains zero, which results in a

mesh-dependency. Mesh size dependent hardening modulus, non-local hardening model, gradient plasticity model, rate-dependent model and micro-polar (cosserat) continuum model are techniques that have been proposed to bypass the mesh-dependency. They are all based on an internal length parameter that scales the shear band.

2.5.1 Mathematical formulation of strain localization

When the failure criterion is reached, the shear band is formed and the material does not act as homogeneous anymore. Properties along the interface are assumed to be different from the intact material. Here we use a homogenization technique based on [88, 94], where average properties of the whole material can be estimated through an averaging procedure. Thickness of the shear band is assumed negligible compared to the dimension of the elementary volume. If constituents are perfectly bonded then the integration over the volume of a representative element yields:

$$\dot{\boldsymbol{\sigma}} = \phi_1 \dot{\boldsymbol{\sigma}}^1 + \phi_2 \dot{\boldsymbol{\sigma}}^2 \quad , \quad \dot{\boldsymbol{\varepsilon}} = \phi_1 \dot{\boldsymbol{\varepsilon}}^1 + \phi_2 \dot{\boldsymbol{\varepsilon}}^2 \tag{2.22}$$

Where ϕ_1 and ϕ_2 represent respectively volume fractions of the intact material and the localization zone.

The strain rate within the fractured zone can be expressed in terms of velocity discontinuities across the interface (see Fig. 2.16):

$$\left[\dot{\boldsymbol{\varepsilon}}^{(2)}\right] = \frac{1}{2h}\left(\vec{n} \otimes \vec{g} + \vec{g} \otimes \vec{n}\right) \longrightarrow \dot{\boldsymbol{\varepsilon}}^{(2)} = \frac{1}{h}\left[N\right]\dot{\boldsymbol{g}} \tag{2.23}$$

where $\vec{n}$ is the unit vector normal to the shear band, and h is the thickness of the shear band.

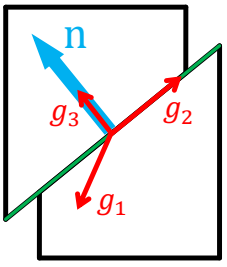

FIGURE 2.16: Schematic representation of the unit vector and velocity discontinuity

[1] Represents the intact material zone
[2] Represents the fractured localization zone

In order to satisfy the equilibrium equation, traction along the interface should remain continuous:

$$\dot{\boldsymbol{t}}^{(1)} = \dot{\boldsymbol{t}}^{(2)} \tag{2.24}$$

The traction of the material is obtained from:

$$\dot{\boldsymbol{t}}^{(1)} = \dot{\boldsymbol{\sigma}}^{(1)} \cdot \boldsymbol{n} \tag{2.25}$$

The traction on the interface is established from the velocity discontinuity:

$$\dot{\boldsymbol{t}}^{(1)} = \boldsymbol{K}^{ep} \cdot \dot{\boldsymbol{g}} \tag{2.26}$$

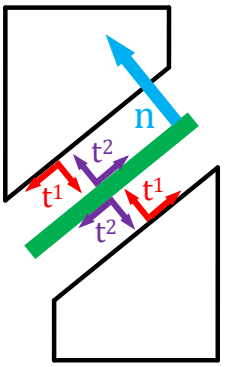

FIGURE 2.17: Schematic representation of traction continuity in 45° inclined plane

where $\boldsymbol{K}^{ep}$ is the elastoplastic operator defining the properties within the fractured zone.

Knowing the constitutive relation $\dot{\boldsymbol{\sigma}}^{(1)} = [\mathbf{C}] : \dot{\boldsymbol{\varepsilon}}^{(1)}$ and using the above-mentioned equations one gets:

$$[\mathbf{C}] : \dot{\boldsymbol{\varepsilon}}^{(1)} \cdot \boldsymbol{n} = \boldsymbol{K}^{ep} \cdot \dot{\boldsymbol{g}} \tag{2.27}$$

where $[\mathbf{C}]$ is the elasticity matrix of the intact material.

Assuming that the thickness of the shear band is negligible compared to the dimension of the intact material, it is possible to conclude that $\phi_1 = 1$. Therefore using (2.22), the velocity discontinuity can be related to the homogenized deformation in the whole volume of the representative element.

$$\dot{\boldsymbol{g}} = [S] : \dot{\boldsymbol{\varepsilon}} \tag{2.28}$$

$$[S] = \left([K^{ep}] + \mu \, [N]^T \, [C] \, [N] \right)^{-1} [N]^T \, [C] \tag{2.29}$$

where $\mu = \phi_2 / h$ is defined as the ratio of the shear band surface area to the sample volume. $[S]$ is a third order tensor which specifies the velocity discontinuity in terms of the macroscopic strain rate.

Replacing 2.23 and 2.29 into 2.22 the stress rate of the intact material can be expressed as:

$$\dot{\boldsymbol{\sigma}}^{(1)} = [\mathbf{C}] : (\mathbf{I} - \mu \, [N] \, [S]) : \dot{\boldsymbol{\varepsilon}} \tag{2.30}$$

where $\mathbf{I}$ is the forth order identity matrix. As mentioned earlier the shear band thickness is negligible, hence it $\dot{\boldsymbol{\sigma}}^{(1)} \approx \dot{\boldsymbol{\sigma}}$.

$$\dot{\boldsymbol{\sigma}} = [\mathbf{C^h}] : \dot{\boldsymbol{\varepsilon}} \quad , \quad [\mathbf{C^h}] = [\mathbf{C}] : (\mathbf{I} - \mu \, [N] \, [S]) \tag{2.31}$$

(2.31) establishes the constitutive law between the stress rate of the representative volume and the macroscopic strain rate.

2.5.2 Elastoplastic formulation of the interface

The elastic domain is represented by a quadratic yield locus which is defined by normal and shear stresses on the localized plane:

$$\begin{aligned} f &= \sigma + \frac{C_0}{B^2(\kappa)}(\tau) - C(\kappa) = 0 \\ C(\kappa) &= C_0 e^{-(\alpha\kappa)^{\gamma_1}} \\ B(\kappa) &= B_0 e^{-(\beta\kappa)^{\gamma_2}} \end{aligned} \tag{2.32}$$

Where $\tau = \sqrt{t_1^2 + t_2^2}$ is the shear stress, $\sigma = t_3$ is the normal stress and $\boldsymbol{t} = \langle t_1 \;\; t_2 \;\; t_3 \rangle^T$ is the traction vector along the interface.

Note that when κ increases due to plastic deformations on the shear band, the yield surface of the interface model decreases and hence engenders a softening behavior. During

loading, C parameter decreases, causing the yield surface to shift along σ axis, and the decrease of B changes the surface shape.

The internal plastic parameter of the interface κ is defined as follow :

$$\dot{\kappa} = (\dot{\boldsymbol{g}}^p \cdot \dot{\boldsymbol{g}}^p)^{\frac{1}{2}} \quad , \quad \dot{\boldsymbol{g}}^p = \dot{\lambda}\frac{\partial f}{\partial \boldsymbol{t}} \tag{2.33}$$

where, $\dot{\boldsymbol{g}}^p$ is the plastic part of the velocity discontinuity that can be obtained through an associated plastic flow rule for material dilation. $\dot{\lambda}$ is the plastic multiplier related to the shear band.

When out of the elastic domain, the interface behavior is assumed to become elastoplastic and recalling the additivity postulate, one obtains :

$$\dot{\boldsymbol{t}} = \boldsymbol{K}^e \cdot (\dot{\boldsymbol{g}} - \dot{\boldsymbol{g}}^p) \tag{2.34}$$

$\boldsymbol{K}^e$ is the second order elastic stiffness matrix of the shear zone.

$$\boldsymbol{K}^e = \begin{bmatrix} K_T & 0 & 0 \\ 0 & K_T & 0 \\ 0 & 0 & K_N \end{bmatrix}$$

where, K_T and K_N are the elastic tangential and normal stiffness moduli per unit cross-sectional of the localized plane.

Using the consistency condition and the plastic flow rule it is possible to link the traction and velocity discontinuity along the interface through the rate form below :

$$\dot{\boldsymbol{t}} = \boldsymbol{K}^{ep} \cdot \dot{\boldsymbol{g}} \tag{2.35}$$

where, $\boldsymbol{K}^{ep}$ is the tangential elastoplastic operator and can be deduced as follow:

$$\boldsymbol{K}^{ep} = \boldsymbol{K}^e - \frac{1}{H_e + H_p}\left(\boldsymbol{K}^e \cdot \frac{\partial f}{\partial \boldsymbol{t}}\right) \otimes \left(\frac{\partial f}{\partial \boldsymbol{t}} \cdot \boldsymbol{K}^e\right) \tag{2.36}$$

where H_e and H_p are respectively the elastic and plastic hardening modulus.

$$H_e = \frac{\partial f}{\partial \boldsymbol{t}} \cdot \boldsymbol{K}^e \cdot \frac{\partial f}{\partial \boldsymbol{t}} \tag{2.37}$$

$$H_p = -\frac{\partial f}{\partial \boldsymbol{\kappa}} \sqrt{\frac{\partial f}{\partial \boldsymbol{t}} \cdot \frac{\partial f}{\partial \boldsymbol{t}}} \tag{2.38}$$

More information on the integration algorithm of the localization model is given in Appendix B.

2.5.3 Model behavior, before and after Localization

Before the shear band appears, the material has an elastoplastic behavior as explained in section 2.2.

The onset of localization is triggered when:

$$\int_V \dot{\boldsymbol{\sigma}} : \dot{\boldsymbol{\varepsilon}} \simeq 0 \tag{2.39}$$

As soon as the strain localization model is active, the material behaves elastically with an elastoplastic interface (see Fig. 2.18). After the interface model is out of its elastic domain it behaves as elastoplastic creating a softening behavior and the intact material undergoes an elastic unloading.

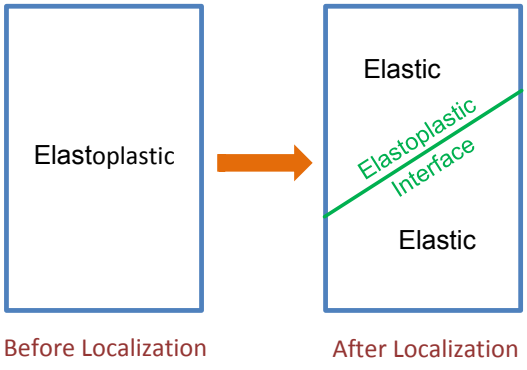

FIGURE 2.18: Schematic representation of before and after activation of the localization model

The global stress-strain behavior of the material before and after the formation of the shear band is schematically shown in Fig. 2.19. As we can see in the figure, there is a slight delay between the onset of localization and the softening behavior. This delay corresponds to the time needed by the localization model to reach the elastic threshold of the interface model and changes to plastic behavior.

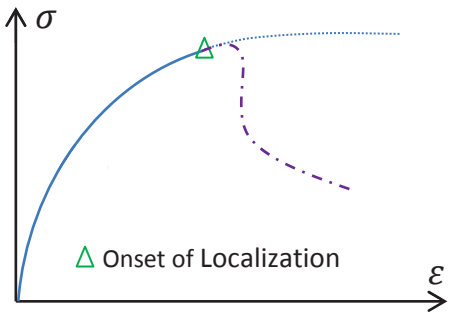

FIGURE 2.19: Schematic representation of the stress-strain behavior before and after localization

2.5.4 Validation of interface model and parameter analysis

In order to verify the capacity of the interface model, a parametric analysis is proposed here. We should verify the existence of an elastic behavior followed by a plastic one that produces a softening behavior. 4 tests are proposed here:

- Uniaxial tension test (shear band orientation taken horizontally) (Fig. 2.20)
- Pure shear test (shear band orientation taken horizontally) (Fig. 2.21)
- Uniaxial compression test (shear band orientation taken 45°) (Fig. 2.22)
- Uniaxial tension test (shear band orientation taken 45°) (Fig. 2.23)

Simulations reported here were carried out with material properties given in table 2.5. These tests are performed along with the sensitivity of α and β which influence the softening behavior.

K_N (GPa.m^{-1})	K_T (GPa.m^{-1})	C_0 (MPa)	B_0 (MPa)	α	β	γ_1	γ_2	μ
12.6	6.3	5.0	5.0	10	10	1	1	0.25

TABLE 2.5: Interface parameters

All tests have been performed on a 4 nodes element. The shear band orientation is deliberately changed according to the utility of the desired simulation.

The results are in perfect concordance with our expectations. In a pure tensile test (Fig. 2.20), the elastic part respects its threshold defined as $C_0 = 5$ MPa. For a pure shear test (Fig. 2.21), the elastic behavior does not exceed the defined value of $B_0 = 5$ MPa. After elastic behavior, the material starts to soften regarding softening parameters, α and β. These parameters have significant influence on the strain softening of

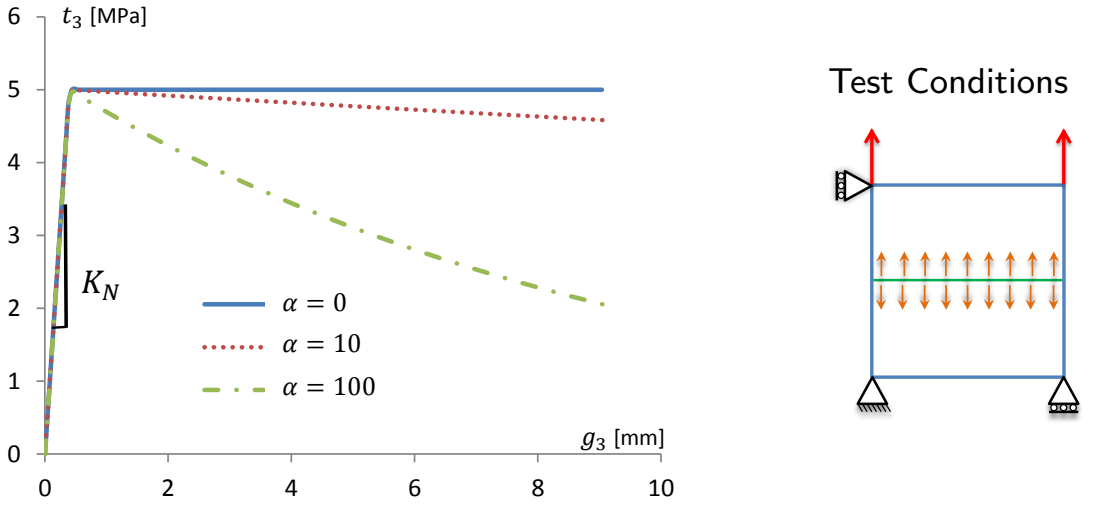

FIGURE 2.20: Uniaxial tension test of the interface with sensitivity of α

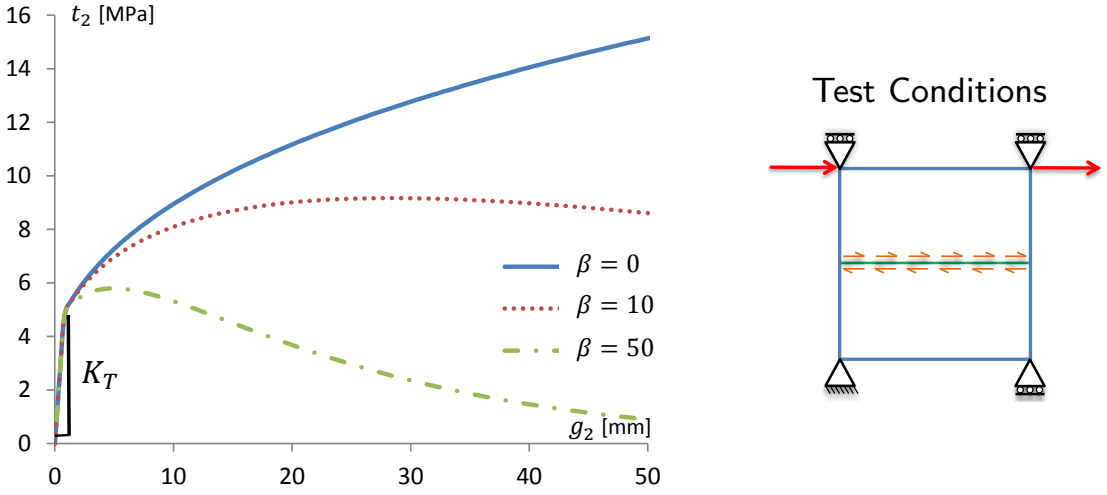

FIGURE 2.21: Pure shear test of the interface with sensitivity of β

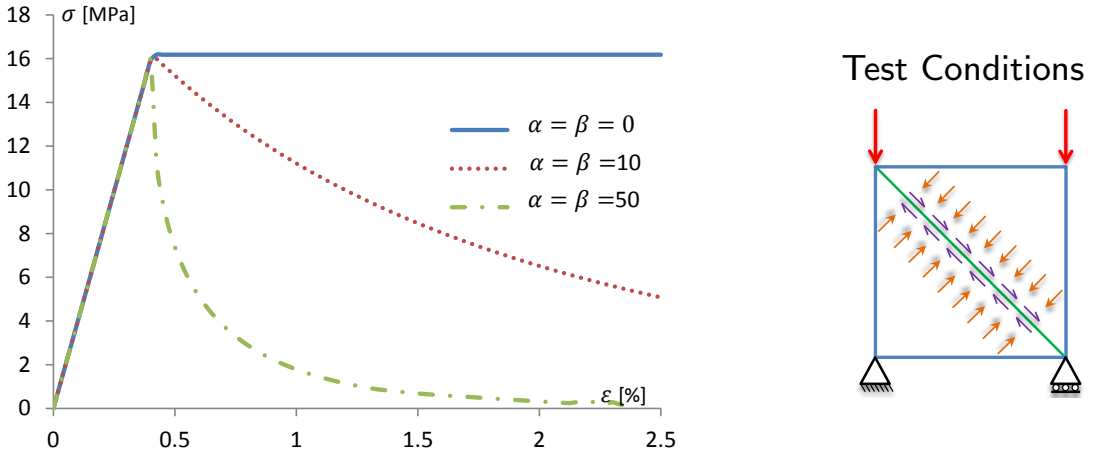

FIGURE 2.22: Uniaxial compression test of the interface with sensitivity of α and β

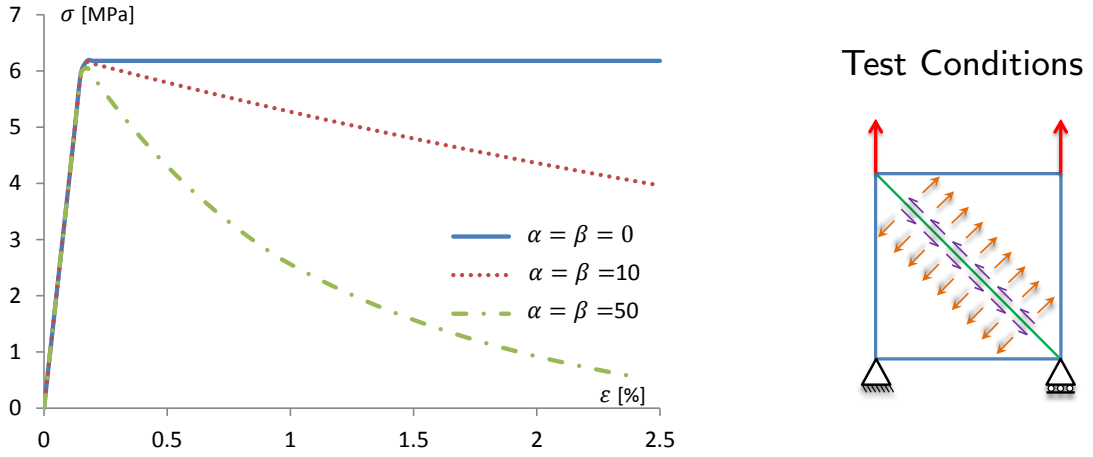

FIGURE 2.23: Uniaxial traction test of the interface with sensitivity of α and β

the material: the more the material is brittle the higher should be their values. As the shear band is set horizontally, there is no need here for a uniaxial compression test because the elastic threshold will never exceed. The importance of these two parameters can be again seen in the case of uniaxial compression (Fig. 2.22) and uniaxial traction (Fig. 2.23) tests to evaluate the behavior of the interface when confronted to both shear and normal stresses at the same time.

2.5.5 Finite element analysis of strain localization under plane strain compression

So far simulations have been performed on only one element. As it can be seen in Fig. 2.22 and Fig. 2.23, this leads to observe a sudden passage to softening behavior. By using just one element, when a crack is formed, it passes directly through the element making a sudden change to softening behavior. But in reality, when a micro-crack is generated at some point, it begins to propagate into the preferential direction to finally make a macro-crack that passes through the whole structure. This will not cause a sudden change anymore and a smooth softening is observed. Moreover, using only one element in the context of continuum mechanics makes impossible to visualize the shear band. Only the stress-strain relationship can be observed. That is why we need to use finite element method for the post localization, so that we can both simulate the propagation of micro-crack and also visualize the localized shear band on a structure.

The constitutive models for pre-localization and post-localization, introduced in sections 2.2 and 2.5 respectively, have been combined together and implemented in THMpasa FE code developed by our laboratory. The performance of the model has been verified

E(MPa)	ν	A	a_1	a_2	a_3	f_c(MPa)	η_c
4000	0.17	8.0e-4	1.6	1.2	0.2	27	0.55

TABLE 2.6: Set of parameters for the intact material

K_n(MPa/m)	K_t(MPa/m)	C_0(MPa)	B_0(MPa)	α	β	μ
12600	6300	2	7	10	10	0.25

TABLE 2.7: Set of parameters for the interface

through a series of plane-strain compression tests. It includes sensitivity of the model to the mesh, shear angle, characteristic length and confining pressure.

2.5.5.1 Mesh-sensitivity

A finite element analysis is performed to evaluate the mesh sensitivity of the model. The sample setup shown in Fig. 2.24 for different mesh sizes (10×20, 15×30 and 20×40), is 1m wide and 2m high. Uniform 4-noded plane strain elements are used for finite element simulations. After the application of constant confining pressure, a vertical displacement is applied on the top end of the sample by increment to ensure a quasi-static loading. The bottom is fixed to prevent vertical displacement and the bottom left node prevents the horizontal displacement. The set of parameters used for the intact material (pre-localization model) and the interface (post-localization model) are shown respectively in table 2.6 and 2.7.

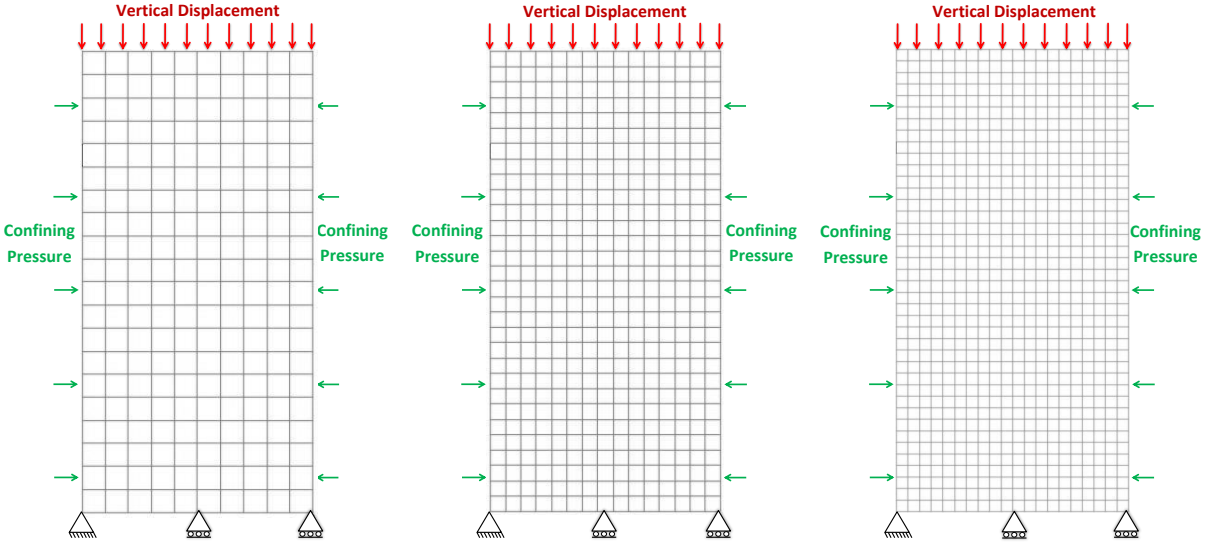

(a) 10 × 20 Elements (b) 15 × 30 Elements (c) 20 × 40 Elements

FIGURE 2.24: Mesh size and boundary conditions used for finite element analysis

Micro-cracks are formed during loading, leading to the appearance of shear bands on weaker planes. In order to artificially make the nucleation of micro-cracks into the creation of the shear band and produce inhomogeneity in the material, an element is deliberately given weaker properties than the others so that it attains the failure criterion faster, and consequently triggering the evolution of micro-cracks. When the weaker element nearly attains the elastoplastic failure criterion, this leads the interface model (see section 2.5), in which the deformations are more pronounced in the direction of the shear band, to be activated into the FE code. For the results of mesh sensitivity, the weaker element is situated at the left side of the structure and upper than the center line, the orientation of the interface being set to -45°.

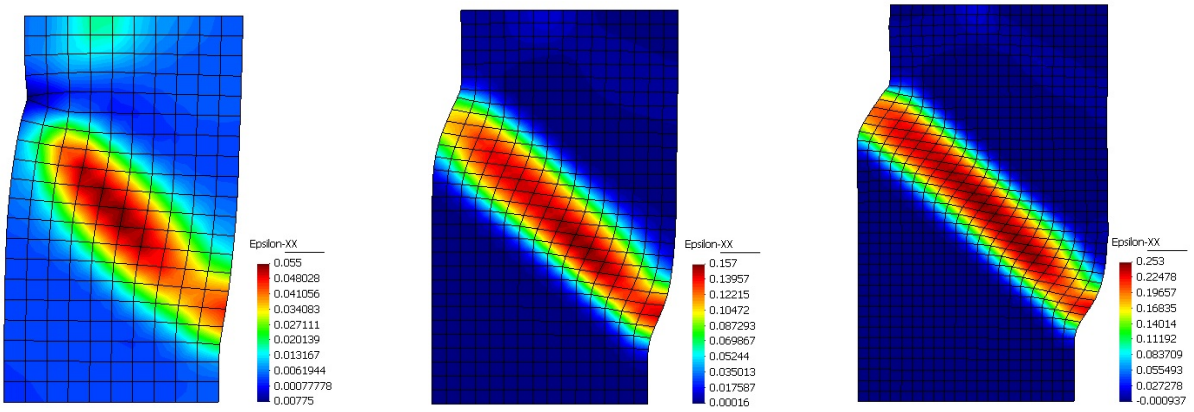

(a) 10 × 20 Elements (b) 15 × 30 Elements (c) 20 × 40 Elements

FIGURE 2.25: Horizontal deformation distribution for different mesh sizes

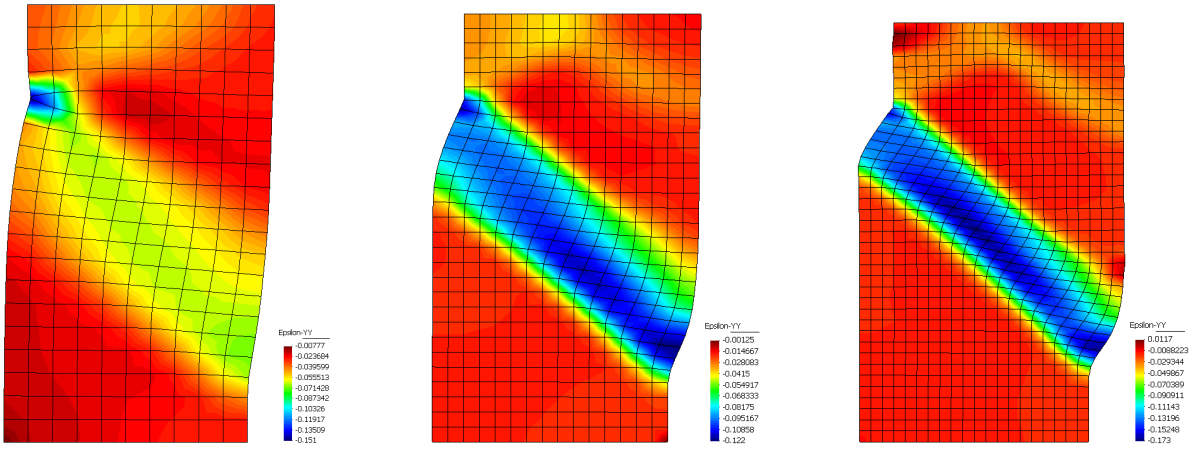

(a) 10 × 20 Elements (b) 15 × 30 Elements (c) 20 × 40 Elements

FIGURE 2.26: Vertical deformation distribution for different mesh sizes

Before the onset of localization, the macroscopic response of the structure shows to be independent of the mesh size. But after localization starts, the response depends on the mesh size due to the fact that the model is based on the classical continuum

mechanics approach. Even though it has been tried to homogenize the material through a characteristic length parameter introduced in the model, the equivalent plastic strain distributions are still influenced by the mesh size.

From Fig. 2.25 and Fig. 2.26 it is clearly seen that the finer the mesh, the thinner shear band becomes, but it starts to stabilize when the mesh size is big enough ($\geq 20\times40$). Hence, from now on we will take a mesh consisting of 20×40 elements as the reference for the future simulations.

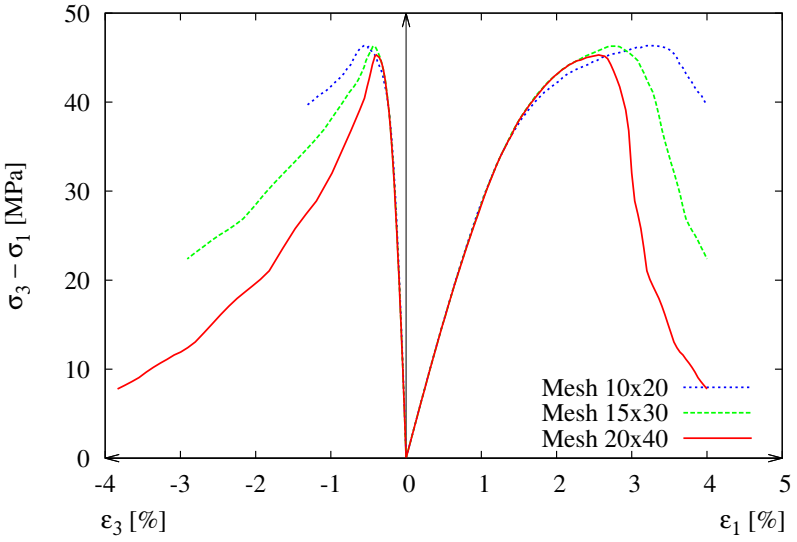

FIGURE 2.27: Comparison of mesh sensitivity for the macroscopic response of a structure under plane strain compression test

2.5.5.2 Shear band angle

Simulations in Fig. 2.28 and Fig. 2.29 show a good agreement between the fixed orientation of the shear band and the results. The shear plane orientation depends on different parameters. For instance, it may depend on boundary conditions imposed for the tests, whether a rough or a smooth boundary has been used. In particular, the inclination of the shear plane with respect to the major principal stress progressively decreases with increasing of the confining pressure. Several methods have been used in the literature to establish a localization condition for pressure sensitive elastoplastic materials. Among them, Rice [95] proposed a bifurcation criterion where the onset of localization and the shear band inclination can both be determined together. However, there is no analytical criterion for three dimensional conditions. Therefore, for the sake of simplicity, we will take a predefined 45° inclination for the localization plane.

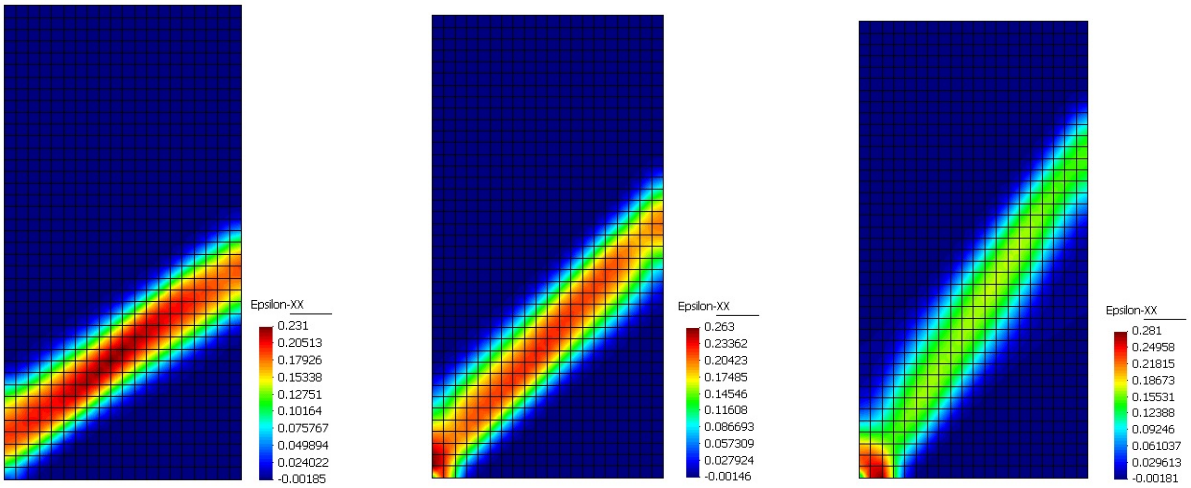

(a) 35° (b) 45° (c) 55°

FIGURE 2.28: Horizontal deformation distribution for different shear band angles

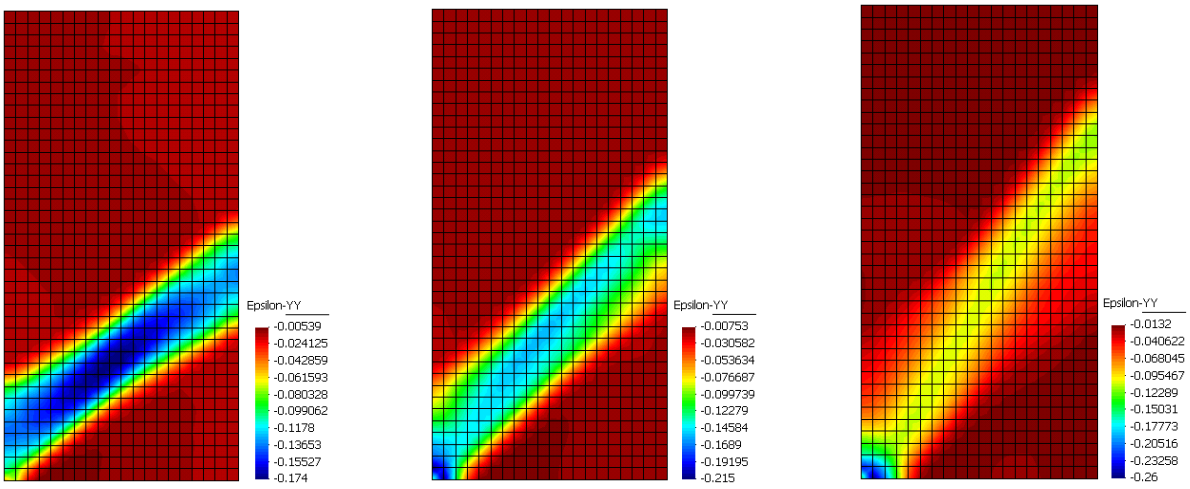

(a) 35° (b) 45° (c) 55°

FIGURE 2.29: Vertical deformation distribution for different shear band angles

The stress-strain curves in Fig. 2.30 shows clearly the relation between the shear band angle and softening behavior. The increase of the shear band angle softens the mechanical behavior.

2.5.5.3 Characteristic length

The characteristic length has a direct impact on the post-peak behavior of the material. This parameter has originally been introduced to homogenize the strains and stresses of the two distinct part of the material located on the shear band and the intact material, and to make it as one single material. It defines the ratio of the shear band surface of the element on its volume.

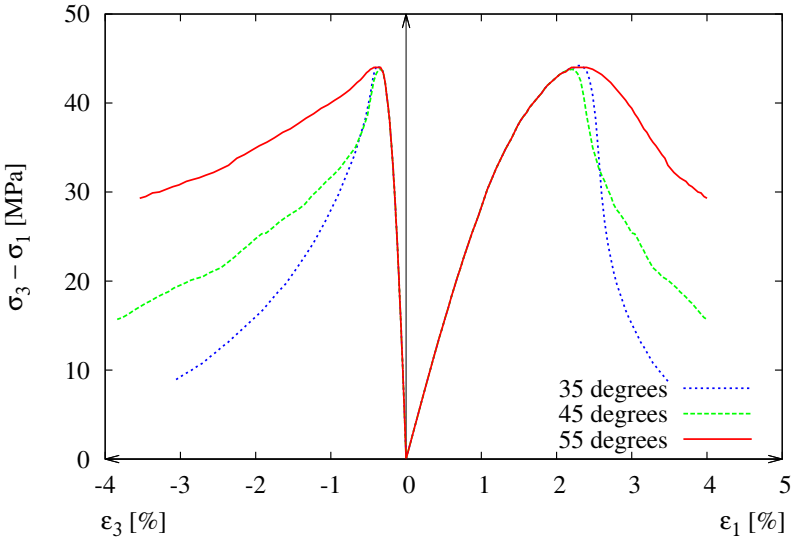

FIGURE 2.30: Comparison of different shear band angle for the macroscopic response of a structure under plane strain compression test

The macroscopic mechanical responses for different values of μ are compared in Fig. 2.31 to Fig. 2.33. From numerical results it can be concluded that μ has an important influence at the same time on the formation of the shear band, and on the macroscopic strain softening behavior of the structure. To be more precise, using a smaller value for μ leads to a shear band with slightly wider thickness and an earlier occurrence of strain softening, the mechanical strength remains identical.

In the context of finite element analysis the characteristic length should be related to the volume associated with each Gauss point within an equivalent sphere [96]:

$$\mu = \frac{1}{l} = \sqrt[3]{\frac{4\pi}{3V}} \tag{2.40}$$

Therefore, the characteristic length should be readjusted for different mesh sizes. When the mesh is finer, the equivalent sphere volume associated to each gauss point decreases, hence μ should be readjusted to a bigger value.

2.5.5.4 Confining pressure

It is well known that confining pressure changes the onset of localization and influences the softening behavior of the material. The same structure with 20×40 elements has been used for numerical simulation of tests with 0 and 20 MPa confining pressures. Numerical comparisons between macroscopic responses are shown in Fig. 2.34. It is obvious that the compressive strength increases with confining pressure and that the

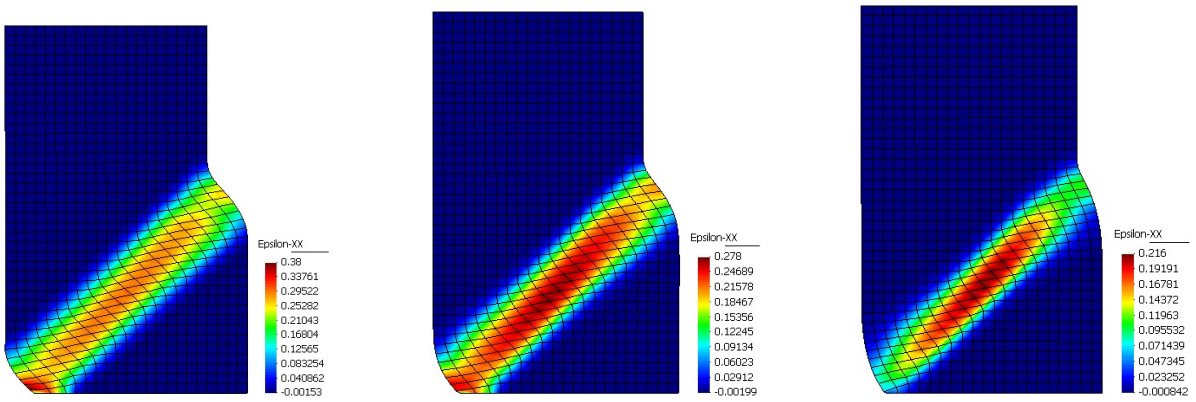

(a) μ=1/16 (b) μ=1/8 (c) μ=1/4

FIGURE 2.31: Horizontal deformation distribution for different characteristic lengths

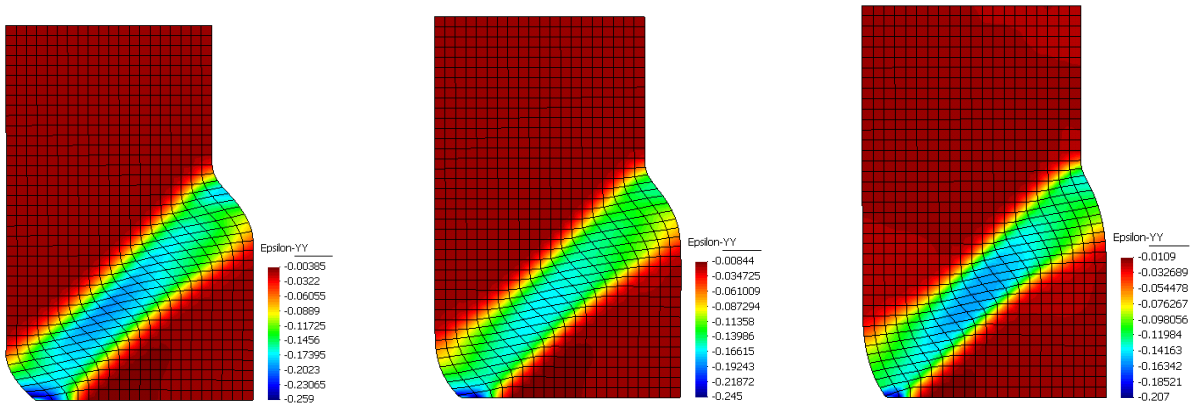

(a) μ=1/16 (b) μ=1/8 (c) μ=1/4

FIGURE 2.32: Vertical deformation distribution for different characteristic lengths

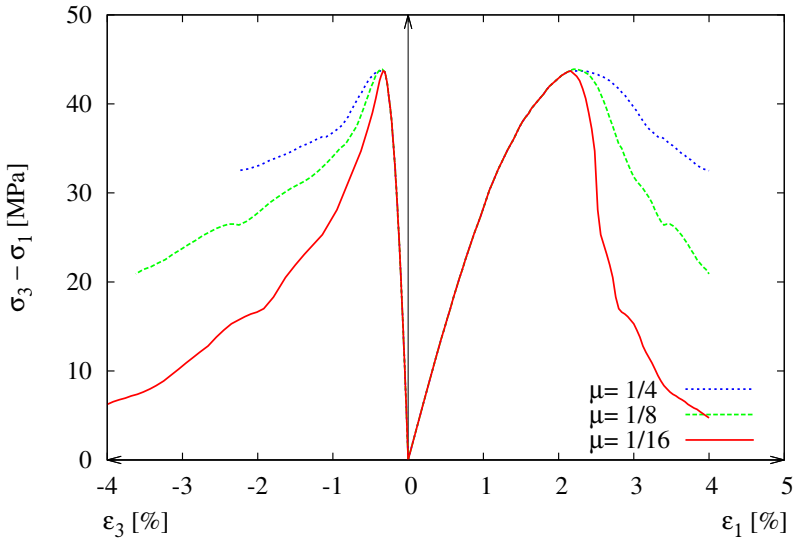

FIGURE 2.33: Comparison of different characteristic length for the macroscopic response of a structure under plane strain compression test

onset of localization happens in a much greater deviatoric stress conditions. As it can be seen in figure Fig. 2.34, the application of higher confining pressure also leads to observe a less pronounced lateral deformation (of minus sign in the figure) as the material is more compressed. In addition, the softening behavior becomes much smoother with higher confining pressure. Moreover, Fig. 2.35 illustrates that the thickness of the shear band is affected by the intensity of confining pressure. It becomes thinner with 20 MPa of confining pressure compared to the case of 0 MPa.

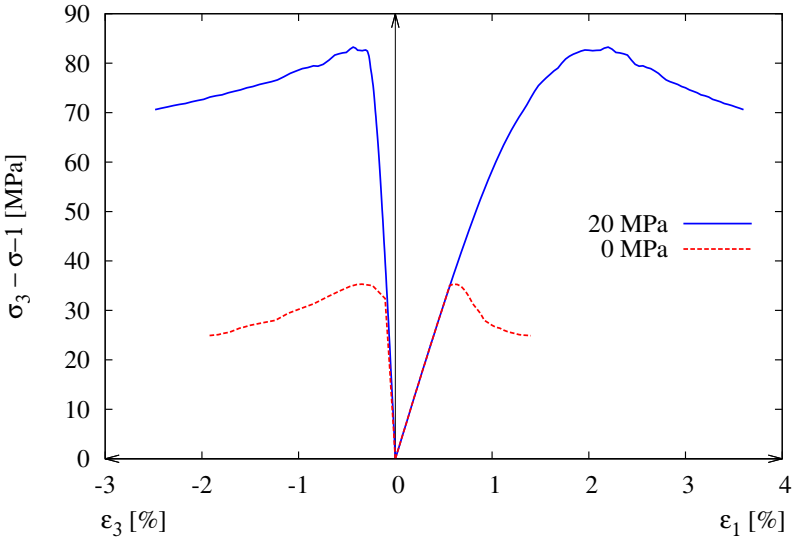

FIGURE 2.34: Comparison of different confining pressure for the macroscopic response of a structure under plane strain compression test

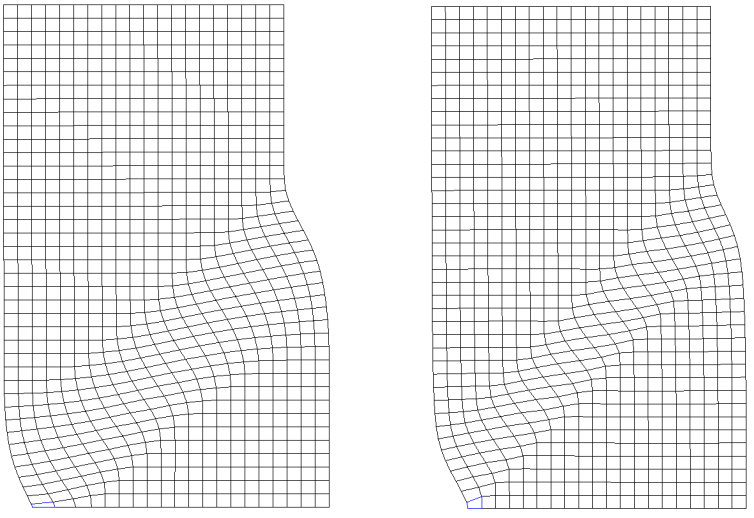

(a) 0 MPa confining pressure (b) 20 MPa confining pressure

FIGURE 2.35: Influence of confining pressure on mesh deformation

2.6 Numerical Simulations for Post-Peak Response

The problem we face here is that experimental compression tests for sound and carbonated samples have all been performed on triaxial conditions. To simulate the triaxial tests with THMpasa finite element code, a two dimensional sample with axisymmetric conditions is needed but this causes the created shear band to appear as a conic shape. Making a typical plane strain test to deal with this problem is not a good idea either. Indeed, in this case, the deformation in one of the axis is blocked making the need for a bigger deviator to have the same axial deformation as for a classical triaxial test, so there would not be any comparison between experimental data.

However, there are some solutions in the literature to make such comparisons. One of them is to decrease the confining pressure to regularize the test conditions to triaxial test, but this technique is not possible for uniaxial tests. Another method could have been the use of plane stress tests, where the deviatoric stress would remain the same since there is no restriction on deformations. Unfortunately, THMpasa FE code does not provide plane stress conditions. So the solution we were forced to adopt here was the use of a plane strain condition by decreasing the initial compressive strength calculated in section 2.3.1, to be able to make a qualitative comparison between the abilities of the model to describe the post-localization behavior of the material and experimental data.

Simulations have been performed for carbonated cement paste but not for leached cement paste that do not show softening behavior. For simulations of sound, partially and completely carbonated samples again a 1m by 2m sample with quadratic elements of mesh size 20×40 has been used. Plastic parameters were taken from table 2.1 and interface parameters were determined by fitting simulations to experimental data. Parameters used for the interface are shown in table 2.8. Fig. 2.36 to Fig. 2.39 show a comparison between simulations and experimental data. The results seem to be qualitatively good.

K_N (GPa.m^{-1})	K_T (GPa.m^{-1})	C_0 (MPa)	B_0 (MPa)	α	β	γ_1	γ_2	μ
12.6	6.3	3.0	6.0	10	1	1	1	0.25

TABLE 2.8: Interface parameters used for sound and carbonated samples

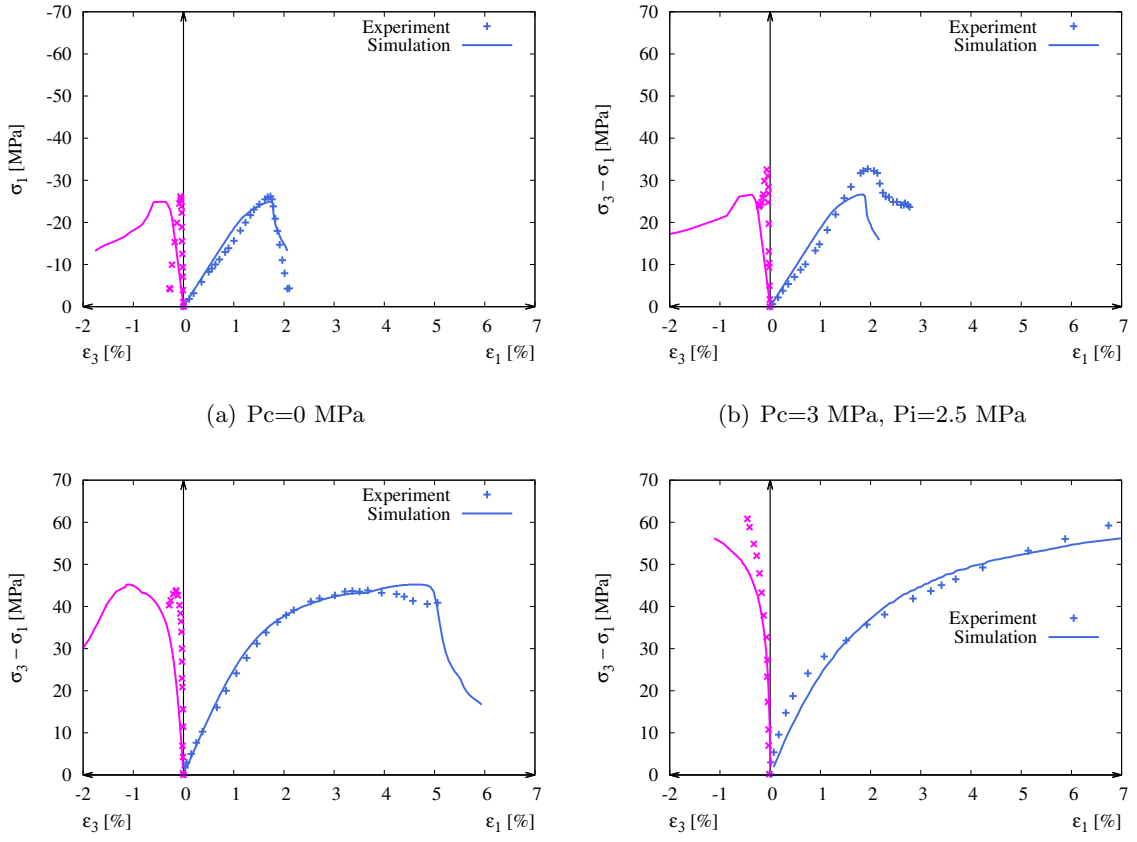

(a) Pc=0 MPa

(b) Pc=3 MPa, Pi=2.5 MPa

(c) Pc=10 MPa, Pi=2.5 MPa

(d) Pc=20 MPa, Pi=2.5 MPa

FIGURE 2.36: Uniaxial and Triaxial compression tests for sound samples ($\phi = 20\text{mm}, h = 22\text{mm}$) at different confining pressures

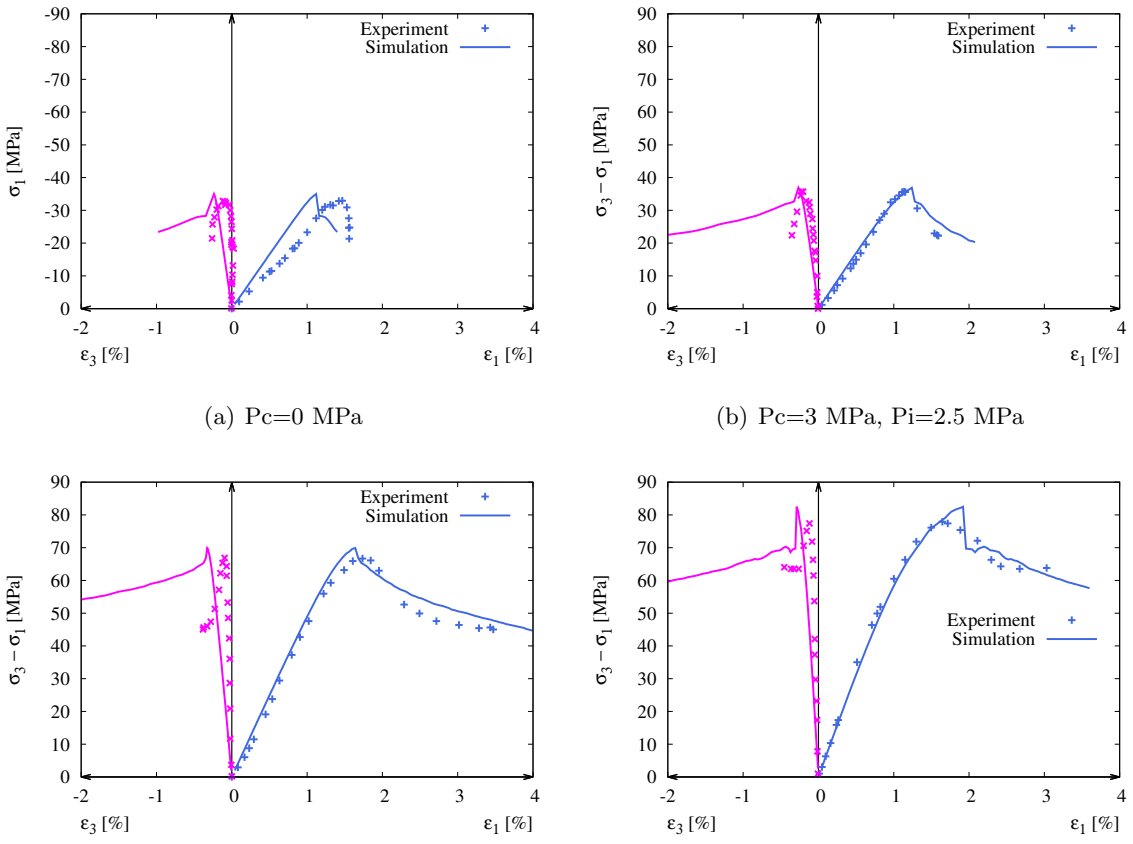

(a) Pc=0 MPa

(b) Pc=3 MPa, Pi=2.5 MPa

(c) Pc=10 MPa, Pi=2.5 MPa

(d) Pc=20 MPa, Pi=2.5 MPa

FIGURE 2.37: Uniaxial and Triaxial compression tests for 3mm carbonated samples ($\phi = 20\text{mm}, h = 22\text{mm}$) at different confining pressures

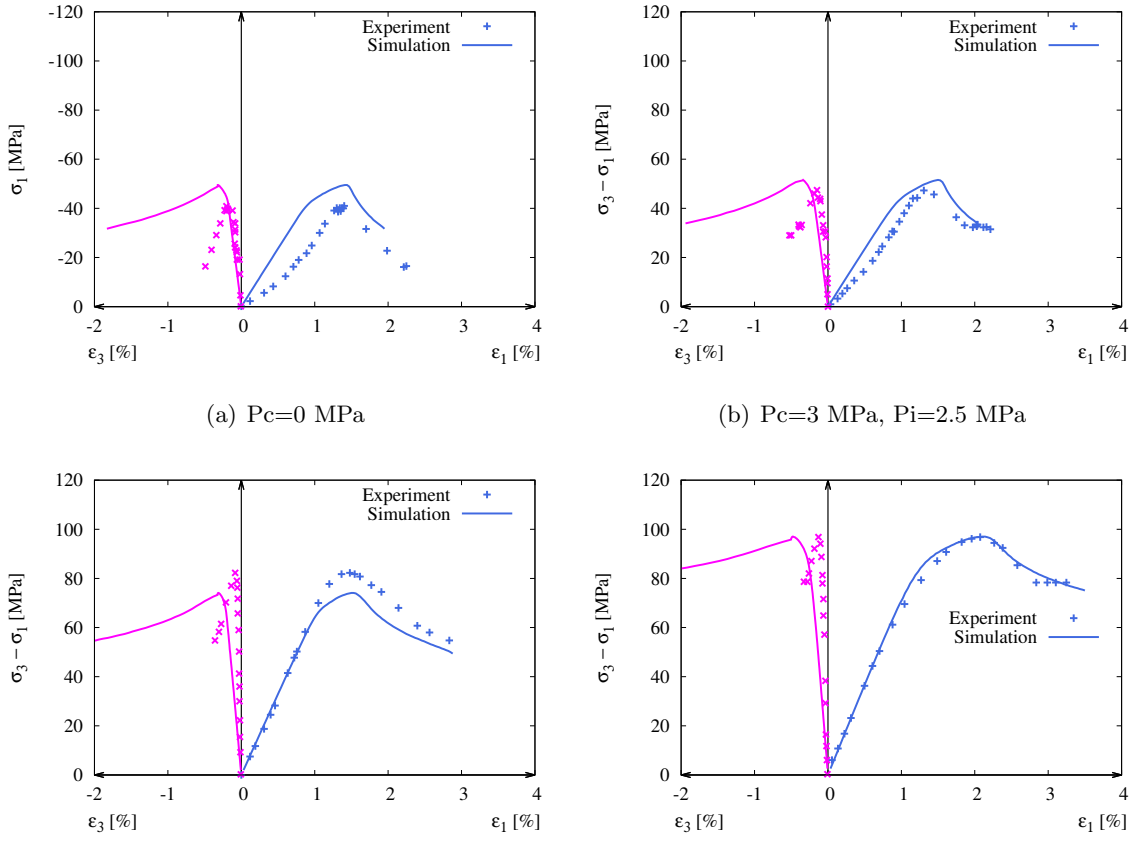

(a) Pc=0 MPa

(b) Pc=3 MPa, Pi=2.5 MPa

(c) Pc=10 MPa, Pi=2.5 MPa

(d) Pc=20 MPa, Pi=2.5 MPa

FIGURE 2.38: Uniaxial and Triaxial compression tests for 6mm carbonated samples ($\phi = 20\text{mm}, h = 22\text{mm}$) at different confining pressures

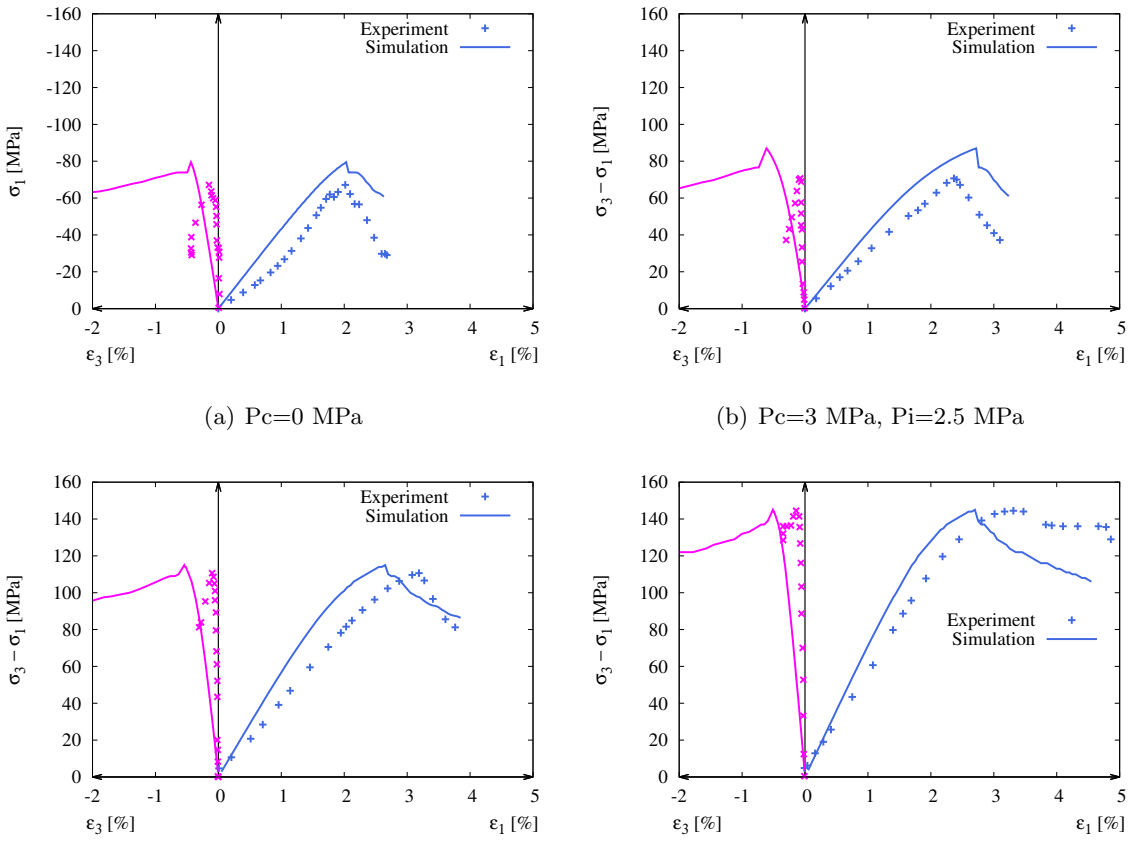

(a) Pc=0 MPa

(b) Pc=3 MPa, Pi=2.5 MPa

(c) Pc=10 MPa, Pi=2.5 MPa

(d) Pc=20 MPa, Pi=2.5 MPa

FIGURE 2.39: Uniaxial and Triaxial compression tests for 10mm carbonated samples ($\phi = 20\text{mm}, h = 22\text{mm}$) at different confining pressures

2.7 Conclusion

This chapter was devoted to modeling changes caused by carbonation and lixiviation in mechanical behavior of an oil-well cement paste. In the first part, an elastoplastic macroscopic model has been introduced and shown its abilities to take into account the mechanical behavior of sound, partially and completely degraded samples up to the peak point of the stress-strain curve. The proposed model is able to capture changes caused by carbonation or lixiviation on mechanical properties including compressive strength, elastic coefficients, confining pressure sensitivity, and transition from compressibility to dilatancy. The quadratic failure envelope put in light the transition from ductile to brittle behavior which happens during carbonation and brittle to ductile behavior with lixiviation through the change of its curvature.

It has been found that the two chemical degradation processes mainly affect the elastic modulus, uniaxial compressive strength and curvature of the failure surface. Concerning the relevant parameters which should be used to characterize the evolutions of material microstructure during chemical degradations, it is found that the increase of porosity is the main factor controlling the degradation of mechanical properties by chemical leaching. The change of porosity, related to the dissolution of solid calcium, can be used as the microstructural parameter in the development of multi-scale modelling in chapters 3 & 4. However, it is not easy to choose a single parameter to characterize the microstructural evolution due to carbonation. It seems that multiple factors should be considered such as the decrease of porosity, the production of carbonate particles and the reinforcement of solid matrix. Based on these observations, we shall develop a multi-scale approach for the mechanical modelling of cement pastes taking into account the microstructural evolution due to the chemical degradation.

In the second part, an interface model [96] based on a homogenization technique to estimate the average macroscopic response in the post-localized regime was proposed to simulate the post-peak behavior of the stress-strain curve by taking into account the softening behavior engendered by the localization of deformations. This became possible by establishing an interface plastic law. To be able to observe the shear band on a structure and simulate the nucleation of microcracks, the aforementioned model has been implemented into a THMpasa FE code using plane strain conditions. For this purpose, the elastoplastic and interface models were combined together and an imperfect element has been set up to trigger the localization. The mesh sensibility, shear plane angle, characteristic length and confining pressure have been analysed for the introduced theoretical model.

Finally FE structural simulations were performed on existing data from uniaxial and triaxial compression tests of sound and carbonated cement paste. Post localization part is rather used for carbonation since leached samples do not exhibit softening behavior. In conclusion, the proposed model is able to capture the main features of the mechanical behavior observed on sound and degraded cement paste. This is confirmed by comparisons between numerical results and existing experimental data which show a quite good agreement.

Part II

Microscopic Approach to Carbonation and Lixiviation of Cement and Concrete

Chapter 3

A Micromechanical Model for Cement Paste with Effects of Carbonation or Lixiviation

Contents

3.1 Introduction

Different kinds of constitutive models have been proposed for modeling the behavior of cement-based materials submitted to mechanical, hydrous, physical and chemical degradation mechanisms. In most cases, phenomenological elastoplastic and damage models have been used. The formulation of these models is essentially based on the standard framework of thermodynamics and experimental evidences. However, it is admitted that the mechanical behavior of cement-based materials is inherently related to the chemical composition and mechanical properties of constituents. The macroscopic response directly depends on the evolution of material microstructure such as the change of porosity, physical and chemical reactions, etc. Phenomenological models can not properly take into account such relationships between microstructure and macroscopic behavior. Some interesting works have been recently reported on the micromechanical modeling of elastoplastic behaviors of heterogeneous geomaterials [97–99].

The aim of this chapter is to propose a micromechanical model to describe the elastoplastic behavior of a cement paste, considering the effects of mechanical loading and chemical reactions of carbonation or lixiviation. In fact, carbonation leads to a drop of porosity in cement paste with generation of calcite ($CaCO_3$) whose size is much smaller than the one of pores. In contrast to that, lixiviation leads to an increase of porosity due to the calcium leaching. Due to these chemical reactions (carbonation or lixiviation), the microstructure of the cement paste will change.

Based on [2, 100], a two-step homogenization procedure (from microscale to mesoscale and from mesoscale to macroscale) is proposed to formulate a macroscopic plastic criterion for the macroscopic elastoplastic behavior of the studied cement-based materials, considering effects of porosity f and volume fraction of calcite ρ generated during the chemical reaction. With this procedure, the studied material can be seen as an "effective" porous medium composed of spherical pores and a matrix which is reinforced by small grains of calcite generated during the chemical reaction (see Fig. 3.1), here the solid phase is described by a pressure sensitive plastic model.

To model lixiviation effects on mechanical behavior of cement paste, we will directly use the criterion derived by [2] for the case of a matrix surrounding spherical pores.

3.2 Macroscopic Criterion for Cement Paste Under Carbonation Based on Maghous et al. [2]

Cement paste is a porous material. Due to carbonation process, the solid phase of cement paste is significantly and progressively reinforced by the new constituent $CaCO_3$ at microscale. In the framework of micro-macro approach, the studied material can be seen as a porous medium at the mesoscale with a reinforced matrix by small grains of $CaCO_3$ at microscale. For the sake of simplicity, pores and grains of calcite are assumed spherical. The representative volume element (RVE) of microstructural evolution due to carbonation process is represented in Fig. 3.1.

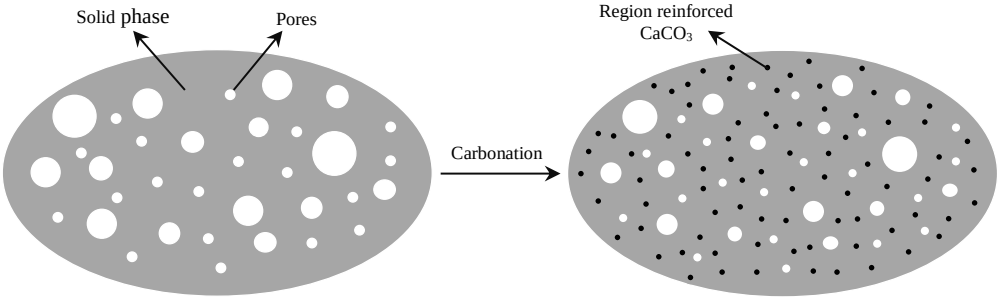

FIGURE 3.1: Schematization of microstructural evolution due to carbonation process

With the process of chemical reaction of carbonation, the studied cement-based material can be seen as an "effective" porous medium with a reinforced matrix (whose solid phase was reinforced by calcite grains generated during carbonation process). Elastic parameters of calcite ($E_i = 95GPa$, $\nu_i = 0.30$) are much larger than the ones of solid phase. The grains of calcite are assumed spherical rigid grains and randomly distributed in the matrix. A two-step homogenization procedure will be proposed for the formulation of a macroscopic plastic criterion for the macroscopic elastoplastic behavior of the studied composite. The first homogenization from micro to meso is for the influences of calcite grains generated during carbonation; the effects of spherical pores will be taken into account in the second homogenization from meso to macro. The volume fraction ρ of calcite $CaCO_3$ at microscale and the porosity f of the "effective" porous medium are given by (Fig. 3.1):

$$\rho = \frac{\Omega_i}{\Omega_i + \Omega_s}, \qquad f = \frac{\Omega_p}{\Omega_i + \Omega_s + \Omega_p} \tag{3.1}$$

where Ω_i, Ω_s and Ω_p are volumes of calcite, solid phase in the reinforced matrix and pores of the "effective" porous medium, respectively.

3.2.1 Homogenization from micro to meso for the effect of calcite

In this transition from micro to meso, the solid phase in the reinforced matrix is assumed to obey to a Drucker-Prager criterion:

$$\phi^s(\boldsymbol{\sigma}) = \sigma_d + T(\sigma_m - h) \leq 0 \tag{3.2}$$

where $\boldsymbol{\sigma}$ denotes the local stress in the solid phase at microscale, with correspondingly $\sigma_m = \text{tr}\boldsymbol{\sigma}/3$ the mean stress, and $\sigma_d = \sqrt{\boldsymbol{\sigma}' : \boldsymbol{\sigma}'}$ the equivalent stress (with $\boldsymbol{\sigma}' = \boldsymbol{\sigma} - \sigma_m \mathbf{1}$). Parameter h represents the hydrostatic tensile strength while T denotes the frictional coefficient.
For geomaterial, the plastic potential of the solid phase is given by:

$$g^s(\boldsymbol{\sigma}) = \sigma_d + t\sigma_m \tag{3.3}$$

here parameter t defines the dilatancy coefficient which controls the volumetric plastic strain.

For a solid phase reinforced by rigid inclusions, we take advantage of results obtained by [2] who made use of a non linear homogenization technique based on the so-called modified secant method. Note that this method was originally proposed by [101] and [102] as a variational method and was later interpreted as "a modified secant method" by [100], [103] and [104]. These authors obtained the criterion and the flow rule of the porous medium with a Drucker-Prager solid phase (3.2) in the context of non-associated plasticity of the solid phase (3.3).

Here we recall the main steps of the modified secant method used in [2]. With (3.2) and (3.3), the support function π^s can be calculated with the help of a sequence of potentials ψ_a using the technique proposed in [105]. Then the stress state is defined by means of a potential ψ_a and an isotropic prestress σ_0^p: $\boldsymbol{\sigma} = \frac{\partial \psi_a}{\partial \boldsymbol{d}} + \sigma_0^p \mathbf{1}$, which can be rewritten with the secant bulk and shear moduli and the isotropic prestress in the following form:

$$\boldsymbol{\sigma} = 2\mu^s \boldsymbol{d}' + \kappa^s d_v \mathbf{1} + \sigma^p \mathbf{1} \tag{3.4}$$

where μ^s, κ^s and σ^p are functions of plastic deformation $\boldsymbol{d}(d_v, d_d)$[1] which is non-uniform in the solid phase. For simplicity, an effective strain rate $\boldsymbol{d}^e$ (average of $\boldsymbol{d}$ over the matrix) is introduced. Then these three non-uniform moduli can be expressed in term of $\boldsymbol{d}^e$ ($\mu^s(\boldsymbol{d}) = \mu^s_{eq}$, $\kappa^s(\boldsymbol{d}) = \kappa^s_{eq}$ and $\sigma^p(\boldsymbol{d}) = \sigma^p_{eq}$). The homogenized behavior takes the

[1] where $d_v = \text{tr}\boldsymbol{d}$, $d_d = \sqrt{\boldsymbol{d}' : \boldsymbol{d}'}$ with $\boldsymbol{d}' = \boldsymbol{d} - \frac{d_v}{3}\mathbf{1}$

form:

$$\begin{aligned}&\tilde{\boldsymbol{\sigma}} = \mathbb{C}^{hom} : \boldsymbol{D} + \tilde{\sigma}^p \mathbf{1};\\ &\mathbb{C}^{hom}(d_v^e, d_d^e) = 3\kappa^{hom}(\kappa_{eq}^s, \mu_{eq}^s)\mathbb{J} + 2\mu^{hom}(\kappa_{eq}^s, \mu_{eq}^s)\mathbb{K}\end{aligned} \tag{3.5}$$

Clearly enough, the symbol "$\sim$" is used here in order to make difference between the mesoscopic stress field $\tilde{\boldsymbol{\sigma}}$ and the microscopic one in the solid phase $\boldsymbol{\sigma}$. $\boldsymbol{\Sigma}$ is used to denote the macroscopic stress of the composite.

Owing to the assumption of rigid inclusions, the macroscopic prestress simply reads $\tilde{\sigma}^p = \sigma_{eq}^p$. The state equations are expressed as:

$$\tilde{\sigma}_m = \kappa^{hom} D_v + \tilde{\sigma}^p; \qquad \tilde{\sigma}_d = 2\mu^{hom} D_d \tag{3.6}$$

Following [105], the relation between effective strain rates in the solid phase and the loading $\boldsymbol{D}$ is:

$$\begin{aligned}\frac{1}{2}(1-\rho)d_v^{e\,2} &= \frac{1}{2}\frac{\partial \kappa^{hom}}{\partial \kappa_{eq}^s} D_v^2 + \frac{\partial \mu^{hom}}{\partial \kappa_{eq}^s} D_d^2\\ (1-\rho)d_d^{e\,2} &= \frac{1}{2}\frac{\partial \kappa^{hom}}{\partial \mu_{eq}^s} D_v^2 + \frac{\partial \mu^{hom}}{\partial \mu_{eq}^s} D_d^2\end{aligned} \tag{3.7}$$

The homogenized secant moduli κ^{hom} and μ^{hom} are evaluated with help of the Mori-Tanaka scheme which coincides here (case of rigid inclusions) with the Hashin-Shtrikman lower bound:

$$\begin{aligned}\kappa^{hom} &= \frac{3\kappa_{eq}^s + 4\rho\mu_{eq}^s}{3(1-\rho)}\\ \mu^{hom} &= \mu_{eq}^s \frac{\kappa_{eq}^s(6+9\rho) + \mu_{eq}^s(12+8\rho)}{6(1-\rho)(\kappa_{eq}^s + 2\mu_{eq}^s)}\end{aligned} \tag{3.8}$$

The strength criterion and the plastic potential of the solid phase reinforced by rigid inclusions take the following form:

$$\begin{aligned}&\phi^m = \widetilde{\sigma}_d + \widetilde{T}(\widetilde{\sigma}_m - h) \le 0; \qquad \widetilde{T} = T\sqrt{1+\frac{3}{2}\rho}\ \frac{\sqrt{1-\frac{2}{3}\rho t^2}}{1-\frac{2}{3}\rho t T}\\ &g^m = \widetilde{\sigma}_d + \widetilde{t}\widetilde{\sigma}_m; \qquad \widetilde{t} = t\sqrt{\frac{1+\frac{3}{2}\rho}{1-\frac{2}{3}\rho t^2}}\end{aligned} \tag{3.9}$$

3.2.2 Homogenization from meso to macro for the effect of pores

In the second homogenization, effect of pores in the "effective" porous medium will be considered. The reinforced matrix is described by (3.9). Comparing equations (3.9) with (3.2) and (3.3), the same forms are found for the criterion and the plastic potential,

respectively. The non-linear homogenization technique proposed by [2] for the porous medium will be adopted here.

Different with the case of a solid phase reinforced by rigid inclusion, the macroscopic prestress changes to $\Sigma^p = \frac{\kappa^{hom}}{\kappa_{eq}^{em}}\tilde{\sigma}_{eq}^p$, the state equation (3.6) becomes:

$$\Sigma_m = \kappa^{hom}\left(D_v + \frac{\tilde{\sigma}_{eq}^p}{\kappa_{eq}^{em}}\right); \qquad \Sigma_d = 2\mu^{hom} D_d \tag{3.10}$$

With the effective strain rates in the "effective" matrix [2] [106]:

$$\begin{aligned}\frac{1}{2}(1-f)d_v^{eff\,2} &= \frac{1}{2}\frac{\partial\kappa^{hom}}{\partial\kappa_{eq}^{mp}}\left(D_v + \frac{\sigma_{eq}^p}{\kappa_{eq}^{em}}\right)^2 - \frac{\kappa^{hom}}{\kappa_{eq}^{em\,2}}\sigma_{eq}^p D_v \\ &\quad + \frac{1}{2}\left(1-f-2\frac{\kappa^{hom}}{\kappa_{eq}^{em}}\right)\left(\frac{\sigma_{eq}^p}{\kappa_{eq}^{em}}\right)^2 + \frac{\partial\mu^{hom}}{\partial\kappa_{eq}^{em}}D_d^2 \\ (1-f)d_d^{eff\,2} &= \frac{1}{2}\frac{\partial\kappa^{hom}}{\partial\mu_{eq}^{em}}\left(D_v + \frac{\sigma_{eq}^p}{\kappa_{eq}^{em}}\right)^2 + \frac{\partial\mu^{hom}}{\partial\mu_{eq}^{em}}D_d^2\end{aligned} \tag{3.11}$$

and the Hashin-Shtrikman upper bounds for the homogenized secant moduli κ^{hom} and μ^{hom}:

$$\begin{aligned}\kappa^{hom} &= \kappa_{eq}^{em}\frac{4(1-f)\mu_{eq}^{em}}{3f\kappa_{eq}^{em} + 4\mu_{eq}^{em}} \\ \mu^{hom} &= \mu_{eq}^{em}\frac{(1-f)(9\kappa_{eq}^{em} + 8\mu_{eq}^{em})}{\kappa_{eq}^{em}(9+6f) + \mu_{eq}^{em}(8+12f)}\end{aligned} \tag{3.12}$$

The macroscopic criterion of the "effective" porous medium with a reinforced matrix is obtained in the following form[3]:

$$\Phi_c = \frac{1+\frac{2}{3}f}{\widetilde{T}^2}\,\Sigma_d^2 + \left(\frac{3f}{2\widetilde{T}^2} - 1\right)\Sigma_m^2 + 2(1-f)h\Sigma_m - (1-f)^2h^2 = 0 \tag{3.13}$$

The macroscopic plastic potential for a non-associated flow rule is given by:

$$G_c = \frac{1+\frac{2}{3}f}{\widetilde{T}\widetilde{t}}\,\Sigma_d^2 + \left(\frac{3f}{2\widetilde{T}\widetilde{t}} - 1\right)\Sigma_m^2 + 2(1-f)h\Sigma_m - (1-f)^2h^2 \tag{3.14}$$

where $\widetilde{T} = T\sqrt{1+\frac{3}{2}\rho}\sqrt{1-\frac{2}{3}\rho t^2}/(1-\frac{2}{3}\rho tT)$ and $\widetilde{t} = t\sqrt{(1+\frac{3}{2}\rho)/(1-\frac{2}{3}\rho tT)}$, T and t are the properties of the solid phase.

Yield surfaces of the criterion (3.13) are illustrated in Fig. 3.2 with different values of T, porosity f and volume fraction of rigid inclusions ρ. One can clearly see that the effect

[2] κ_{eq}^{em}, μ_{eq}^{em} and $\tilde{\sigma}_{eq}^p$ are the equivalent secant bulk, shear moduli and the isotropic prestress of the reinforced matrix.

[3] More details can be found in [2]

of f and ρ on the macroscopic plastic criterion (3.13) is significant. Material strength increases with the raise of ρ and with the reduce of f.

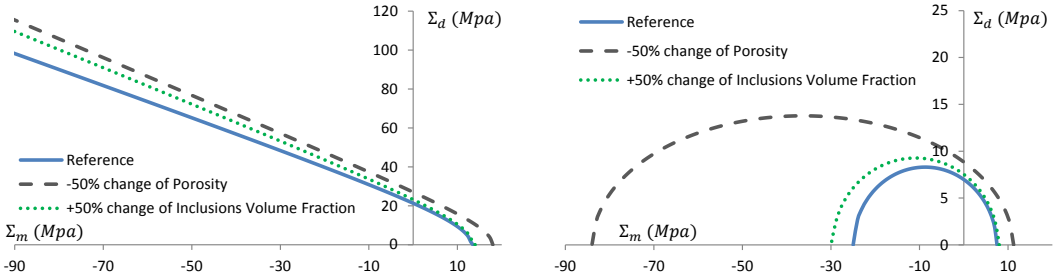

(a) With great value for T_m=0.9 (b) With small value for T_m=0.3

FIGURE 3.2: Yield surface of (3.13) with different values of T, f and ρ (Reference values: $f = 0.3$, $\rho = 0.3$)

3.2.3 Non-associated model for the reinforced cement paste

The macroscopic criterion (3.13) and the macroscopic potential (3.14) will be used here to describe the macroscopic plastic behavior of the cement-based material considering the effect of carbonation. For cement paste, the plastic hardening here is described by the evolution of the frictional coefficient T and that of the dilatancy coefficient t which are functions of the equivalent plastic strain ε^p, the following forms are proposed:

$$\hat{T} = T_m - (T_m - T_0)e^{-b_1\varepsilon^p} \ , \qquad \hat{t} = t_m - (t_m - t_0)e^{-b_2\varepsilon^p} \tag{3.15}$$

The plastic flow rule is given by:

$$\boldsymbol{D}^p = \dot{\lambda}\frac{\partial G}{\partial \boldsymbol{\Sigma}}(\boldsymbol{\Sigma}, f, \rho, \hat{T}, \hat{t}) \tag{3.16}$$

The equivalent plastic strain of the solid matrix is given by:

$$\dot{\varepsilon}^p = \frac{\boldsymbol{\Sigma} : \boldsymbol{D}^p}{(1-f)(1-\rho)\left[\hat{T}h + (\hat{t} - \hat{T})\frac{\Sigma_m}{(1-f)(1-\rho)}\right]} \tag{3.17}$$

The evolution of porosity and the inclusion are determined as:

$$\begin{aligned} \dot{f} &= (1-f)\mathrm{tr}\mathbf{D}^p - (1-f)(1-\rho)\hat{t}\dot{\varepsilon}^p \\ \dot{\rho} &= -\rho(1-\rho)\hat{t}\dot{\varepsilon}^p \end{aligned} \tag{3.18}$$

3.2.4 Experimental Validation of the Proposed Model

The experimental data on oil-well cement paste [33, 54] are again used here in order to evaluate the capacity of the proposed model. It is recalled that four different states are studied experimentally (sound, 3mm, 6mm and 10mm carbonated samples) (see also section 1.3.7.2). In the first series, the samples are not exposed to carbonation process. The other three series of samples are subjected to an accelerated carbonation process in order to reach three different levels of carbonation measured by the depth of carbonated zone in each sample.

As indicated previously, the porosity f and the volume fraction of new component (calcite) ρ of the studied composite change during the process of carbonation, the obtained values are given in Table 3.1. $E_c = 95$ GPa and $\nu_c = 0.3$ are taken as the elastic parameters of calcite grains. More details are given in Appendix C. The elastic and plastic parameters of cement paste are determined from sound samples without carbonation process. The equivalent elastic parameters of the material are estimated through a Mori-Tanaka homogenization scheme (see (3.19) and (3.20)):

$$k^{hom} = \left(\sum_{r=0} f_r \frac{k_r}{3k_r + 4\mu_0}\right)\left(\sum_{s=0} \frac{f_s}{3k_s + 4\mu_0}\right)^{-1} \tag{3.19}$$

$$\mu^{hom} = \left(\sum_{r=0} f_r \frac{\mu_r}{\mu_0(9k_0 + 8\mu_0) + 6\mu_r(k_0 + 2\mu_0)}\right)\left(\sum_{s=0} f_s \frac{\mu_r}{\mu_0(9k_0 + 8\mu_0) + 6\mu_s(k_0 + 2\mu_0)}\right)^{-1} \tag{3.20}$$

where k_r and μ_r respectively denote the bulk and shear moduli of the phase r, while k^{hom} and μ^{hom} those of the homogenized medium.

Parameters	Solid phase	Calcite
Elastic parameters	E_s=20GPa, ν_s=0.2	E_i=95GPa, ν_i=0.3
Plastic parameters	T_0=0.01 T_m=1.21 b_1=500 t_0=-1 t_m=0.15 b_2=120 h = 20	
porosity and calcite		
sound samples	f=0.3516	ρ=0
3mm carbonated samples	f=0.3	ρ=0.12
6mm carbonated samples	f=0.286	ρ=0.25
10mm carbonated samples	f=0.286	ρ=0.50

TABLE 3.1: Typical values of parameters of the non-associated model

With the macroscopic criterion (3.13) and parameters given in Table 3.1, Fig. 3.3 shows the failure envelopes for four groups of samples with different carbonation depths and

different confining pressures. There is an overall good concordance between numerical simulation and experimental data. Effects of porosity f, calcite volume fraction ρ and confining pressure are correctly accounted. This presents a significant advantage with respect to phenomenological models. The proposed model has the capacity to describe the macroscopic elastoplastic behavior of the studied cement-based material considering the effects of chemical reactions throughout carbonation.

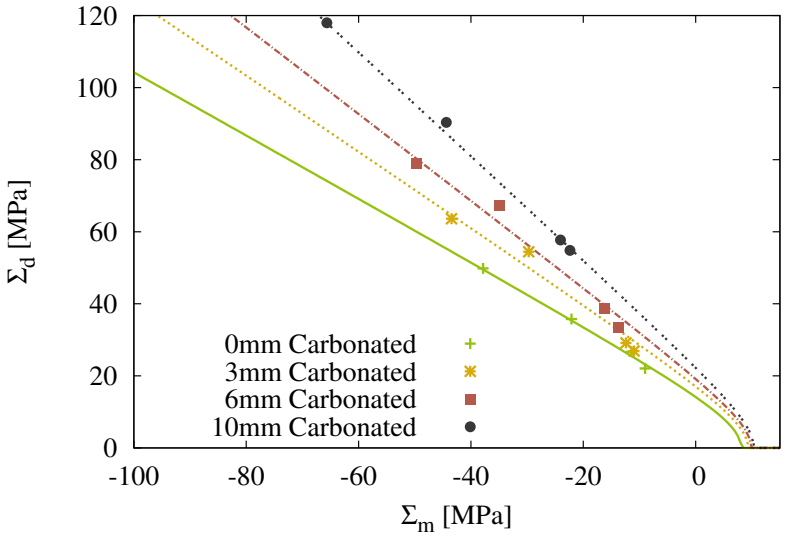

FIGURE 3.3: Failure envelopes for sound, 3mm, 6 mm and 10 mm carbonated samples

Fig. 3.4 illustrates numerical predictions of uniaxial compression tests with different states of carbonation. The proposed model is sensitive to the change of porosity f and the volume fraction of calcite ρ. The mechanical strength increases with the diminution of f and with the increase of ρ.

In order to validate the proposed non-associated model, comparisons between numerical simulations and experimental data for uniaxial and triaxial compression tests with different confining pressures (3MPa, 10MPa and 20MPa) and different states of carbonation are studied. The same set of elastic and plastic parameters (see Table 3.1) is used for all simulations. In Fig. 3.5, we show the comparisons for the case of sound material without chemical reaction. The macroscopic responses of partially and fully carbonated samples are illustrated, respectively, in Fig. 3.6 to Fig. 3.8. One can see that a good agreement is found for both axial and lateral strains. The proposed micromechanical model correctly takes into account the influence of calcite generated by the chemical reaction and the effect of porosity on the macroscopic behavior of reinforced cement paste. Compared with classical phenomenological models, carbonation effects which are inherently related to the evolution of mineral compositions and microstructure are properly taken into account in this constitutive modeling through a clear homogenization procedure.

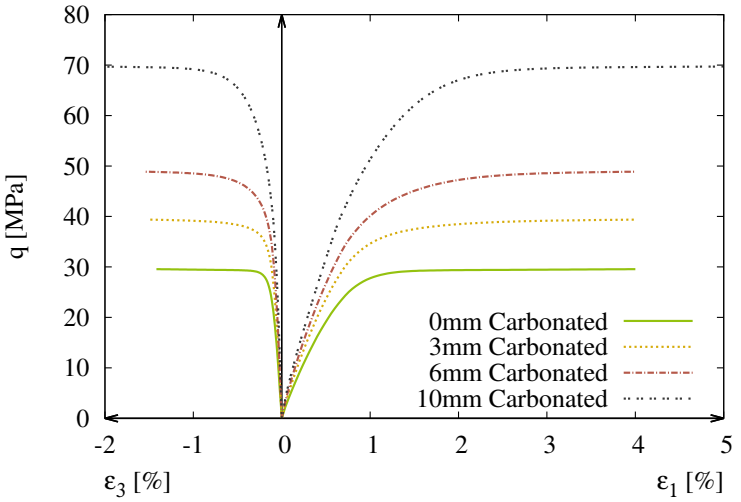

FIGURE 3.4: Numerical predictions with uniaxial compression for different states of carbonation

In Fig. 3.9, we show evolutions of porosity f and the calcite volume fraction ρ in the "reinforced" matrix during triaxial compression tests with different confining pressures performed on a totally carbonated sample (10 mm). Although the changes of f and ρ are very small, they have a great influence on the macroscopic behavior of the studied composite.

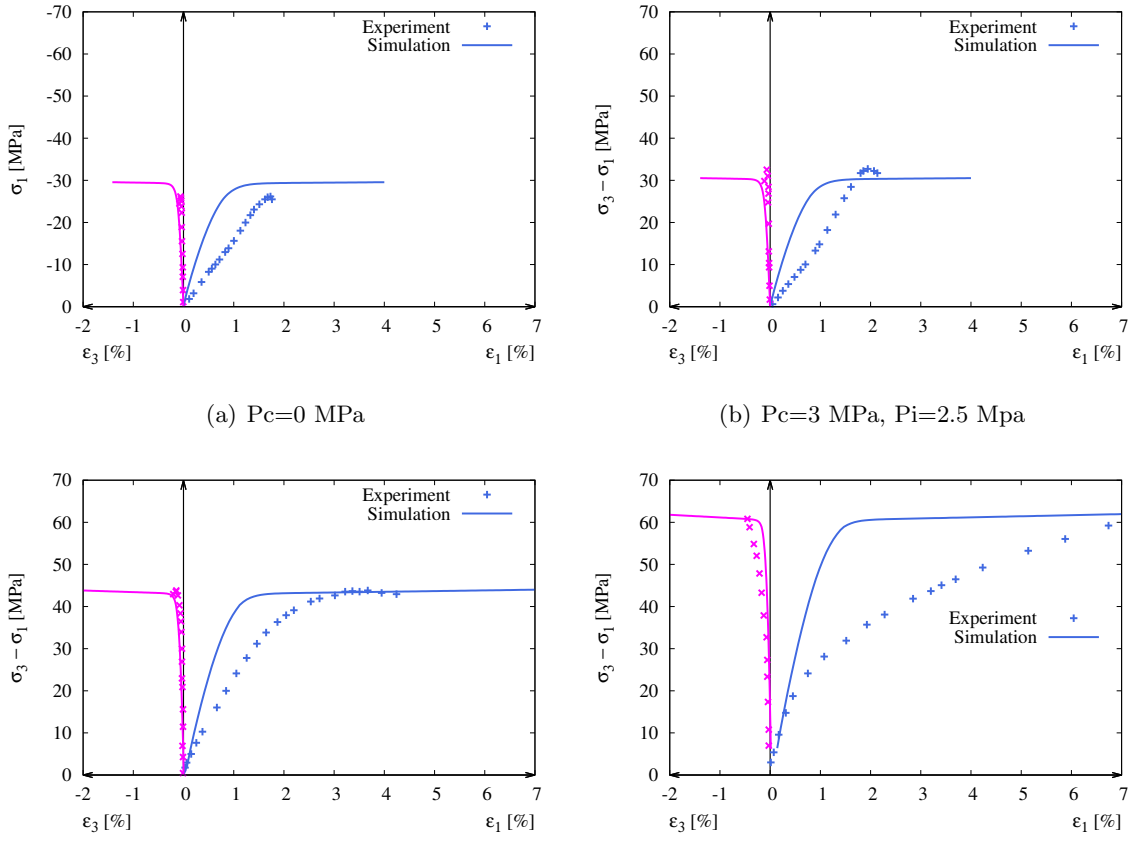

(a) Pc=0 MPa

(b) Pc=3 MPa, Pi=2.5 Mpa

(c) Pc=10 MPa, Pi=2.5 Mpa

(d) Pc=20 MPa, Pi=2.5 Mpa

FIGURE 3.5: Uniaxial and Triaxial compression tests for sound samples at different confining pressures

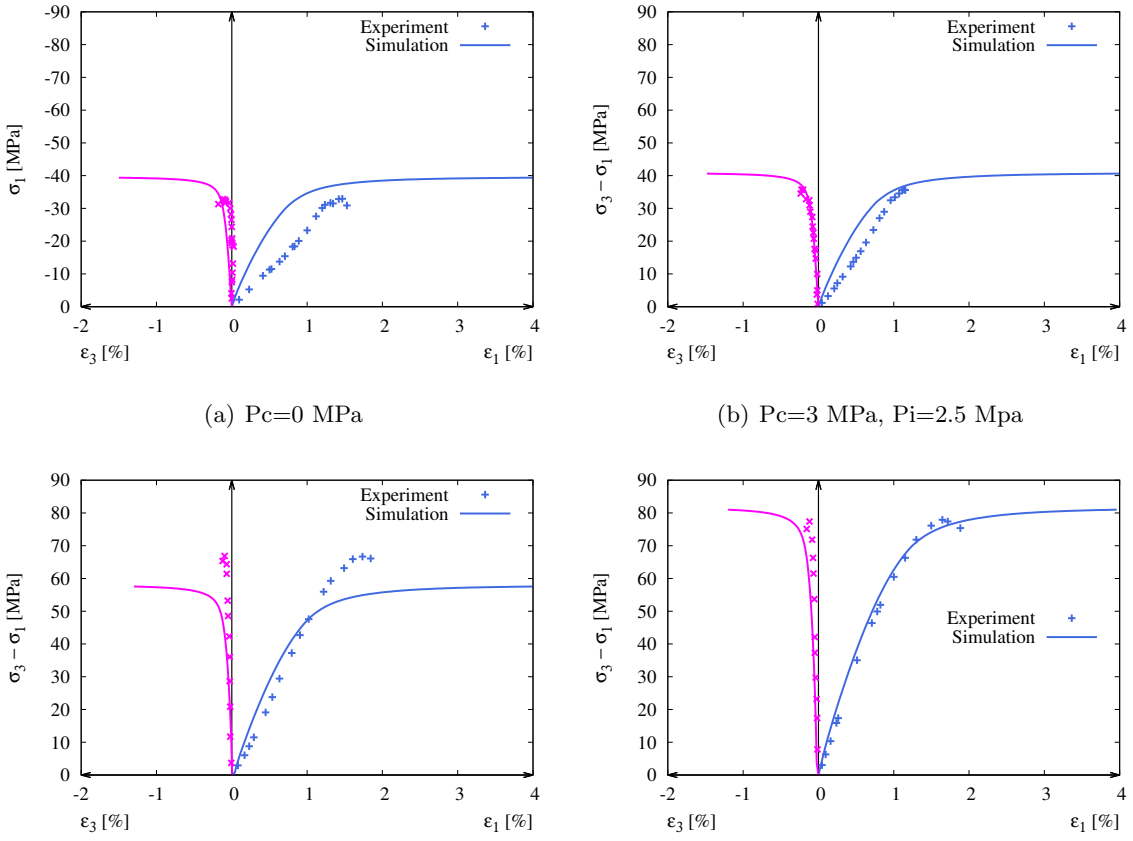

(a) Pc=0 MPa

(b) Pc=3 MPa, Pi=2.5 Mpa

(c) Pc=10 MPa, Pi=2.5 Mpa

(d) Pc=20 MPa, Pi=2.5 Mpa

FIGURE 3.6: Uniaxial and Triaxial compression tests for 3mm carbonated samples at different confining pressures

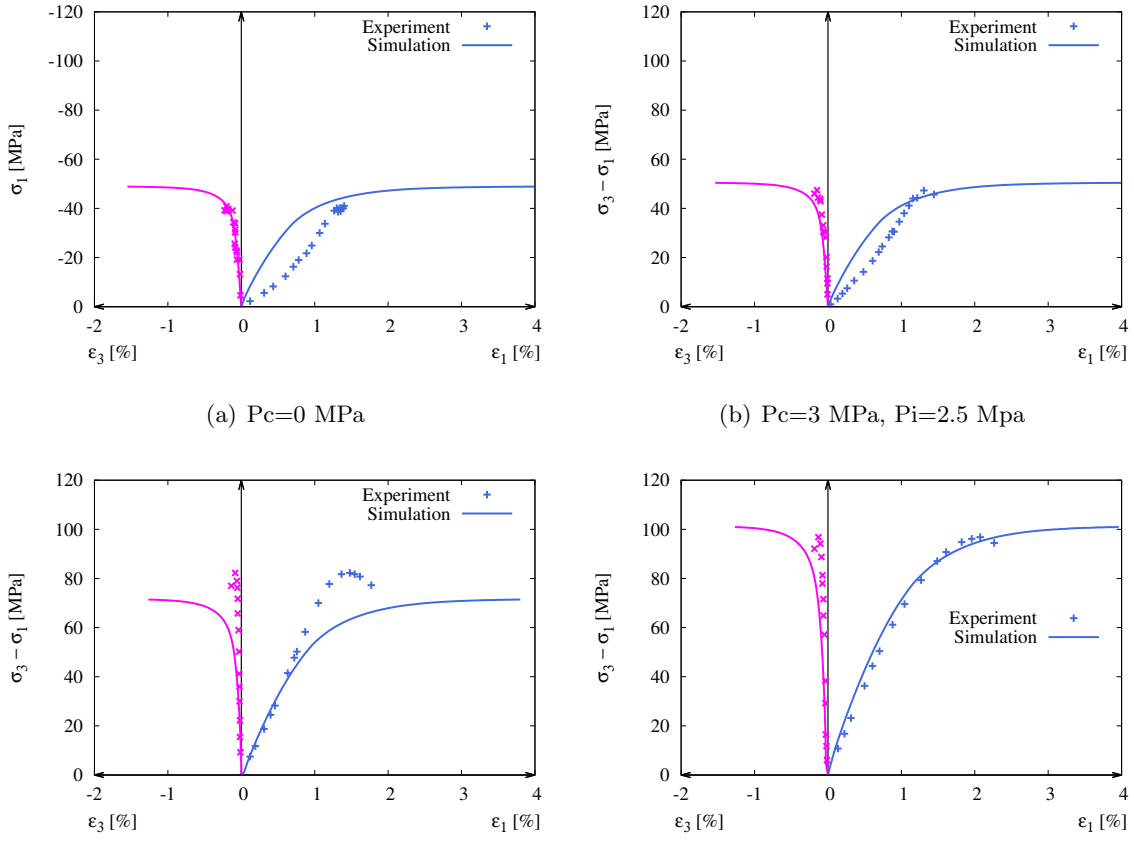

(a) Pc=0 MPa

(b) Pc=3 MPa, Pi=2.5 Mpa

(c) Pc=10 MPa, Pi=2.5 Mpa

(d) Pc=20 MPa, Pi=2.5 Mpa

FIGURE 3.7: Uniaxial and Triaxial compression tests for 6mm carbonated samples at different confining pressures

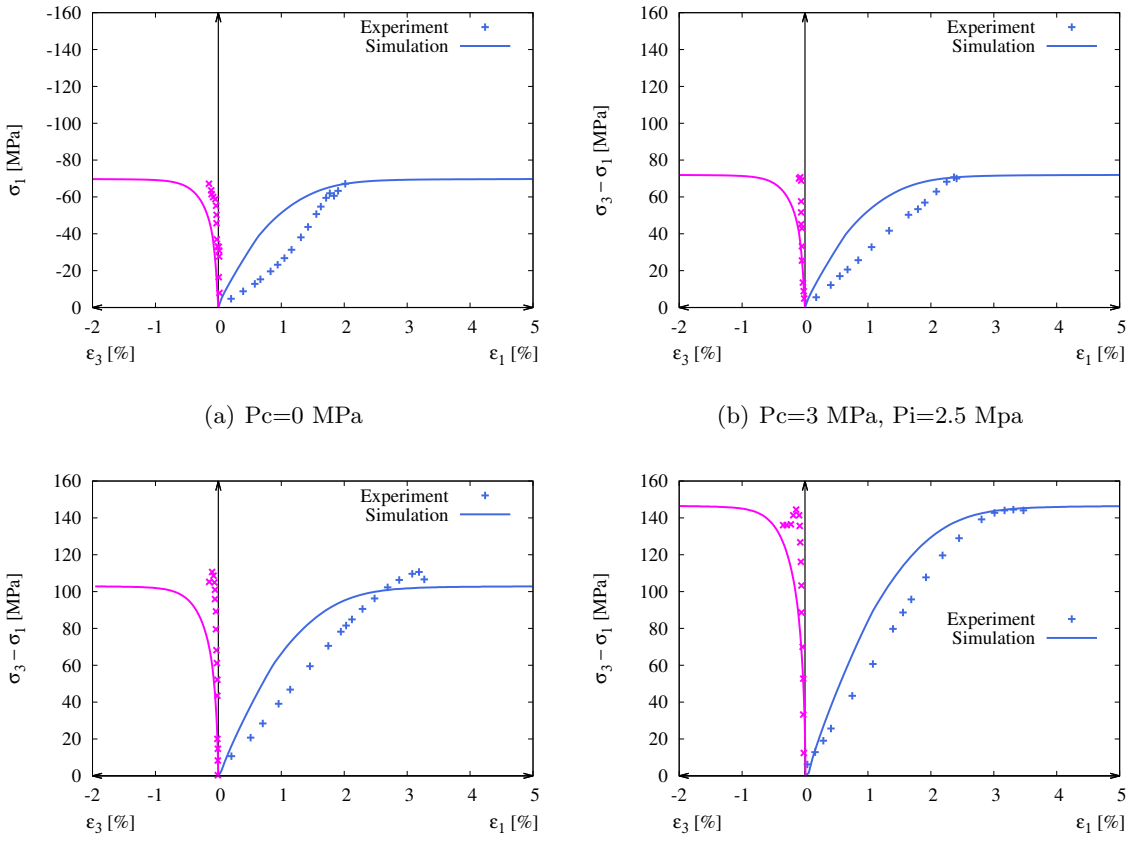

(a) Pc=0 MPa

(b) Pc=3 MPa, Pi=2.5 Mpa

(c) Pc=10 MPa, Pi=2.5 Mpa

(d) Pc=20 MPa, Pi=2.5 Mpa

FIGURE 3.8: Uniaxial and Triaxial compression tests for 10mm carbonated samples at different confining pressures

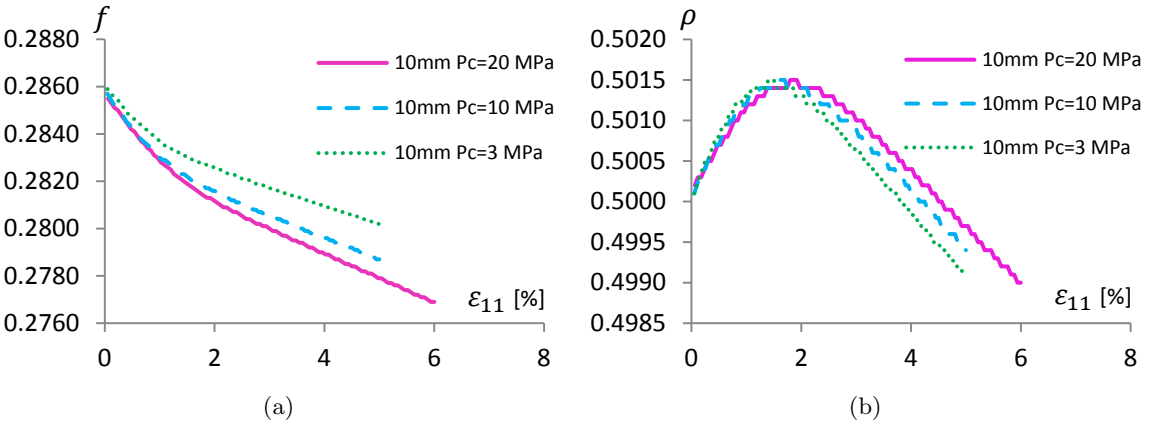

(a)

(b)

FIGURE 3.9: Evolutions of porosity and the volume fraction of calcite with axial strain performed on a totally carbonated sample

3.3 Case of the Cement Paste Lixiviation

As indicated earlier, lixiviation provokes the leaching of calcium from the cement paste matrix and leads to a significant increase of material porosity. This results in a loss of strength and stiffness properties of the cement paste. In the framework of micro-macro approach, the studied material can be seen as a randomly distributed 2 phase composite; a solid phase and pores, where the solid phase represents the cement and surrounds pores. For simplicity, pores are assumed to be spherical. The representative volume element (RVE) of microstructural evolution during lixiviation process is represented in Fig. 3.10.

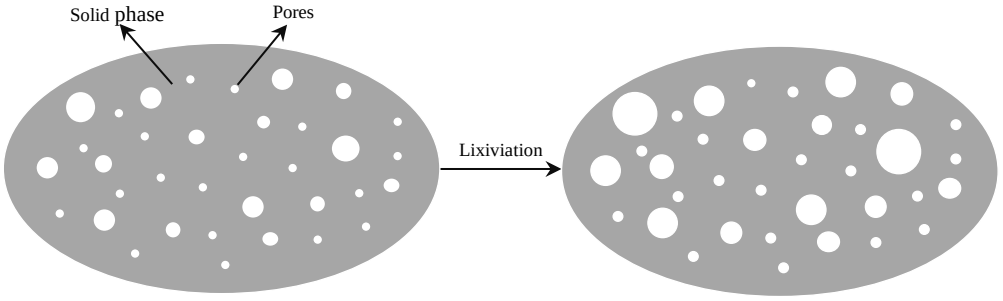

FIGURE 3.10: Schematization of microstructural evolution due to lixiviation process

Considering that the solid phase obeys to a Drucker-Prager criterion, we can take advantage of the criterion proposed by [2] for a solid phase surrounding randomly distributed spherical pores (see section 3.2.2):

$$\Phi_l = \frac{1+\frac{2}{3}f}{T^2}\,\Sigma_d^2 + \left(\frac{3f}{2T^2}-1\right)\Sigma_m^2 + 2(1-f)h\Sigma_m - (1-f)^2h^2 = 0 \tag{3.21}$$

where T and t are respectively the frictional and dilation coefficients of the solid phase. This coincides with (3.13), when the volume fraction of inclusions $\rho = 0$. The macroscopic plastic potential for a non-associated flow rule is given by:

$$G_l = \frac{1+\frac{2}{3}f}{Tt}\,\Sigma_d^2 + \left(\frac{3f}{2Tt}-1\right)\Sigma_m^2 + 2(1-f)h\Sigma_m - (1-f)^2h^2 \tag{3.22}$$

3.3.1 Experimental validation: data from [78]

The manufacturing and experimental procedure has been explained in chapter 1. The porosity f of cement paste changed during the leaching process. Obtained values of porosity from experimental data are given in table 3.2. A lot of studies highlight that during lixiviation, because of calcium leaching, cement-based materials exhibit de-cohesion

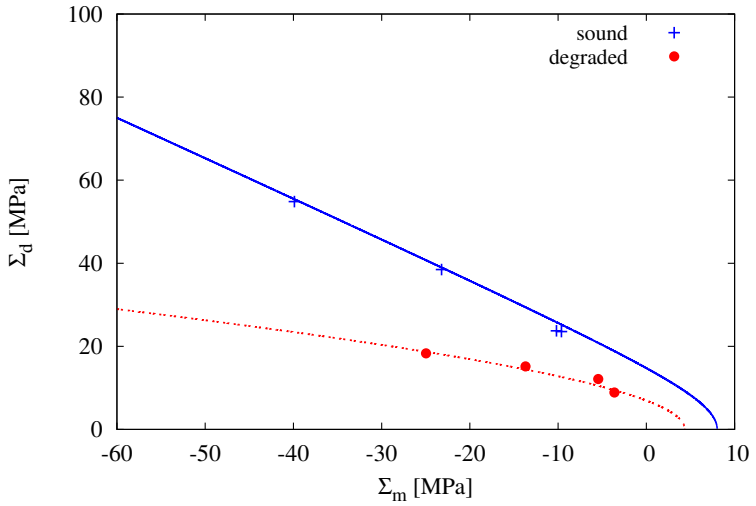

FIGURE 3.11: Representation of failure surface for the sound and degraded cement paste

and frictional softening [78, 80]. Accordingly, as shown in table 3.2, the frictional coefficient also decreases during lixiviation. All other elastic and plastic parameters of cement paste are determined from sound samples. Equivalent elastic parameters of the material are estimated through a Mori-Tanaka homogenization scheme.

Parameters	Solid phase
Elastic parameters	E_s=20GPa, ν_s=0.2
Plastic parameters	T_0=0.01 T_m(sound)=1.3 T_m(degraded)=0.95 b_1=250 t_0=-1.1 t_m=0.2 b_2=1000 h = 20
porosity	
sound	f=0.37
degraded	f=0.56

TABLE 3.2: Typical values of parameters of the non-associated model

Fig. 3.11 shows the comparison between experimental failure envelope and the model failure criterion (3.21) using values given in table 3.2. The same set of elastic and plastic parameters is used for all simulations. In Fig. 3.12 and Fig. 3.13 , we show comparisons of the elastoplastic behavior for the case of sound and leached cement paste respectively. Generally, a good agreement is found between experimental data and numerical simulations.

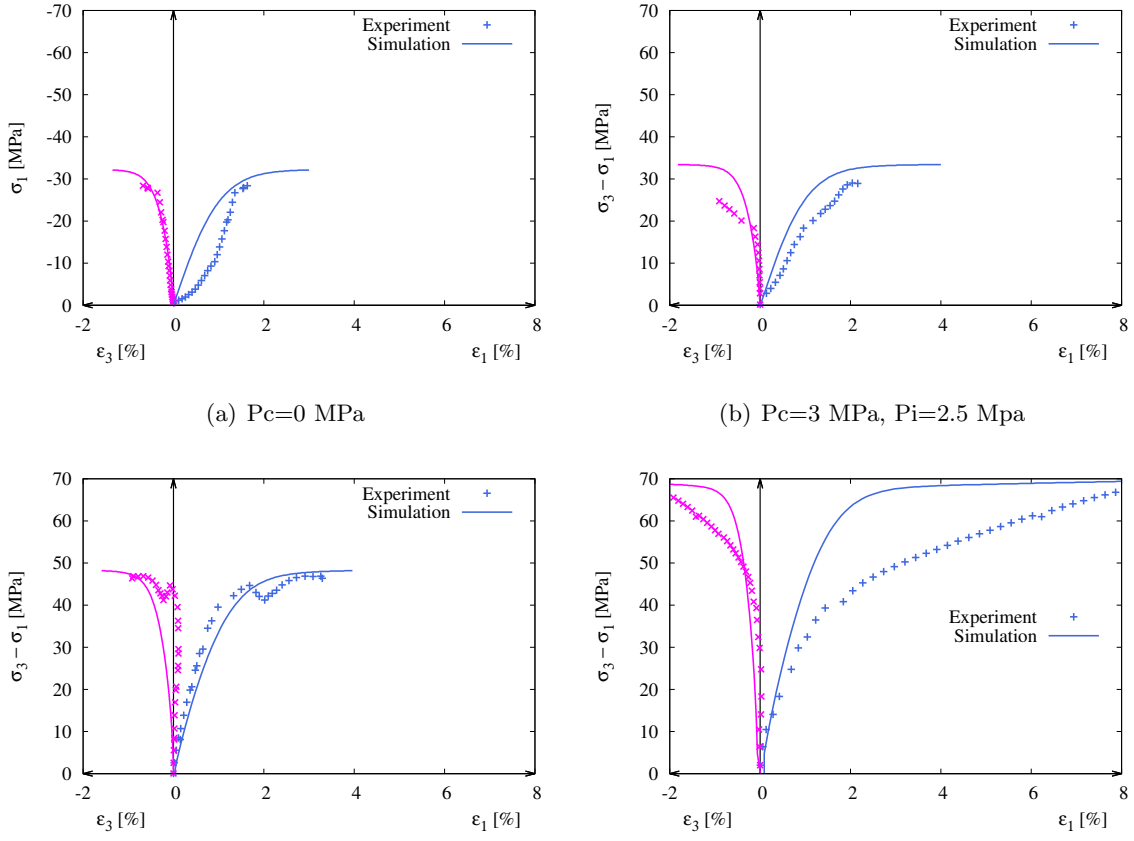

(a) Pc=0 MPa

(b) Pc=3 MPa, Pi=2.5 Mpa

(c) Pc=10 MPa, Pi=2.5 Mpa

(d) Pc=20 MPa, Pi=2.5 Mpa

FIGURE 3.12: Uniaxial and Triaxial compression tests for sound samples at different confining pressures

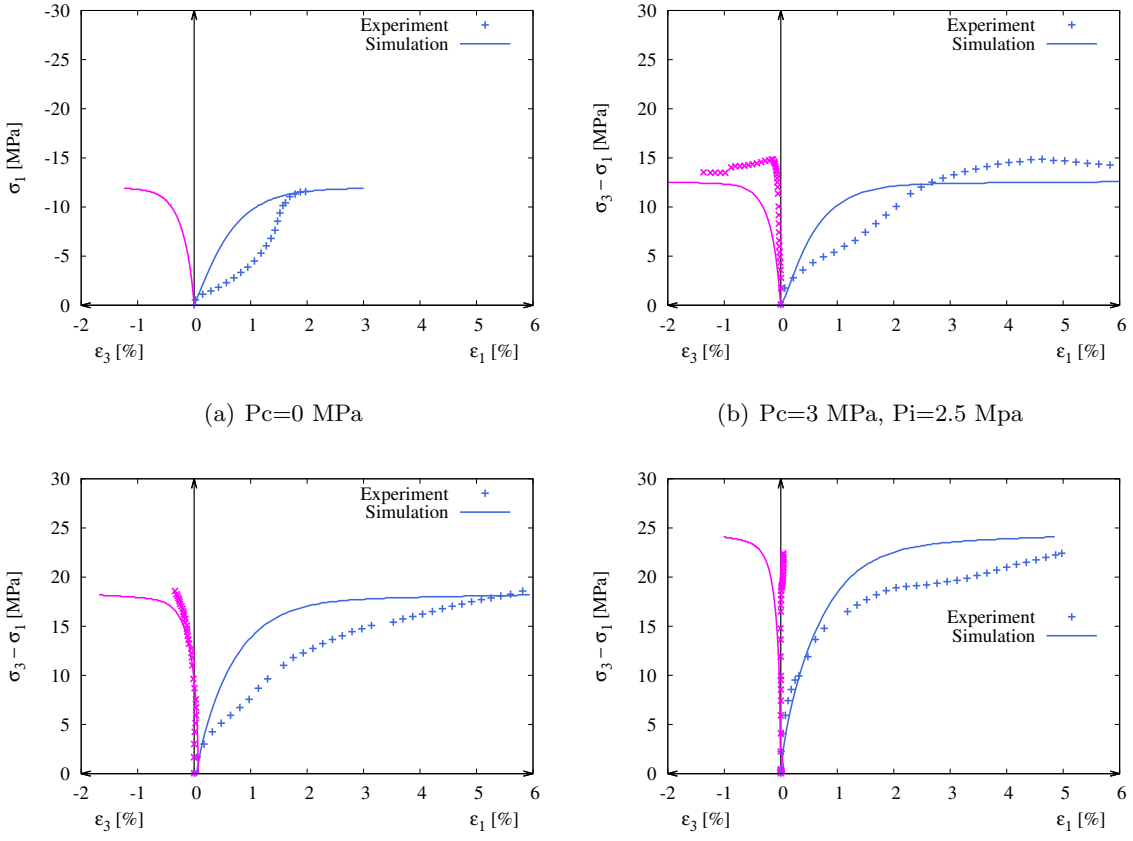

(a) Pc=0 MPa

(b) Pc=3 MPa, Pi=2.5 Mpa

(c) Pc=10 MPa, Pi=2.5 Mpa

(d) Pc=20 MPa, Pi=2.5 Mpa

FIGURE 3.13: Uniaxial and Triaxial compression tests for leached samples at different confining pressures

3.3.2 Experimental validation: data from [65]

Yurtdas and al. [78] have studied the effect of lixiviation on triaxial mechanical behavior by considering the sound and completely leached states. However, Carde [65] has evaluated this effect at various degradation rates, but only under uniaxial compression. These experimental data presented in chapter 1 (section 1.4.2) will be used here to assess and validate the micromechanical model. The author determined the porosity on test samples of diameter of 10, 12, 14 and 20 mm according to the degradation rate [74]. However, there is no data on the porosity of test samples of diameter 30 mm that are used here. Nevertheless, the porosity of specimens of diameter 10, 12, 14 and 20 mm increases linearly with the rate of degradation. Therefore, the porosity of the 30 mm test samples is deduced from the degradation rate and reported in table 3.3.

The porosity of sound samples are approximately determined to be 42 %.

Parameters	Sound	Degraded [%]				
		25	39	54	72	100
Elastic	E_s=40000 MPa; ν_s=0.3					
Plastic	T_m^0=1.76	T_m^{25}=1.7	T_m^{39}=1.64	T_m^{54}=1.61	T_m^{72}=1.55	T_m^{100}=1.2
	T_0=0.01 ; t_0=-0.5 ; t_m=0.3 ; b_1=2250 ; b_2=5000 ; h=20 MPa					
Porosity [%]	41.9	46.1	49.1	52.3	56.1	62.1

TABLE 3.3: Set of parameters used for simulations on [65]

As mentioned before, there is a significant decrease of frictional coefficient during calcium leaching. This has been taken into consideration in table 3.3. Fig. 3.14 shows the impact of calcium leaching on the failure envelope of the studied cement paste. A comparison between predictive capacities of the model and the existing experimental data of the stress-strain curves is shown in Fig. 3.15. Simulations show a good agreement with the elastoplastic behavior and strength properties of the cement paste.

The effective elastic modulus of cement paste changes with porosity. With the elastic moduli E_s and ν_s of the solid phase, and the porosity (see table 3.3), the effective modulus of the cement paste can be calculated by using a Mori-Tanaka homogenization scheme. The comparisons between the estimations and experimental data are shown in Fig. 3.16.

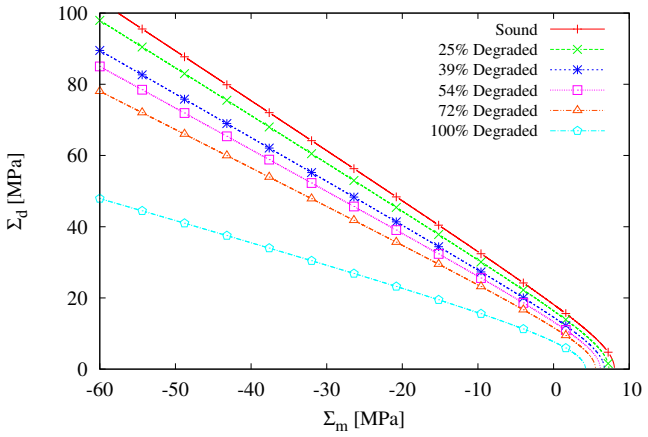

FIGURE 3.14: Representation of failure surface cement paste from sound state to completely degraded state

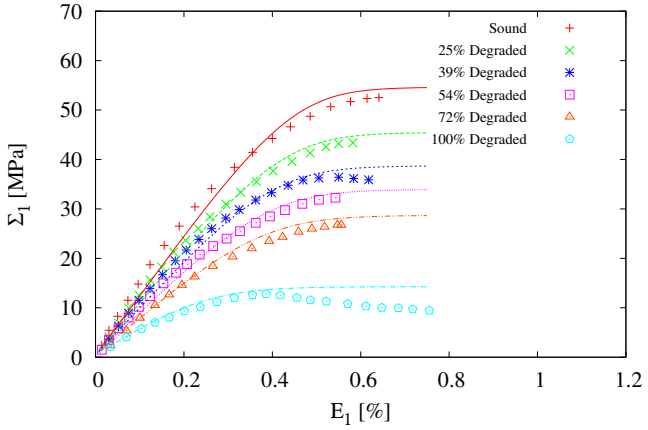

FIGURE 3.15: Uniaxial compression tests of cement paste from sound state completely degraded samples state

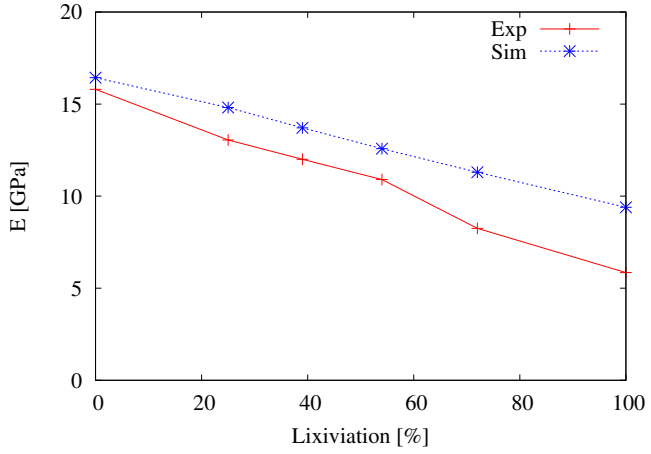

FIGURE 3.16: Comparison between the Mori-Tanaka estimation of Young's modulus and experimental data

3.4 Conclusion

A micromechanical non-associated model is proposed to describe the macroscopic behavior of cement paste considering effects of carbonation or lixiviation. Due to these chemical reactions, the material undergoes changes. In the case of carbonation the generated calcite reinforces the cement paste. The studied cement-based material can be seen as an "effective" porous medium whose matrix is reinforced by calcite grains. With the process of carbonation, the porosity f will reduce and the volume fraction of calcite will increase. With a two-step homogenization procedure, a macroscopic criterion and a macroscopic plastic potential are proposed based on [2]. The proposed model is implemented in a conventional finite element computation code. A series of comparison between numerical simulations and experimental data for uniaxial and triaxial compression tests are carried out for different states of carbonation. This model is able to describe the main features of mechanical behavior of cement paste such as strong dependency on confining pressure, transition from volumetric compressibility to dilatancy. The influences of porosity and the grains of calcite generated during carbonation are simultaneously taken into account. In the case of lixiviation, the cement paste is assumed as a two phase composite, composed of a solid phase and spherical pores. During the leaching of calcium the porosity increases and the frictional coefficient decreases. The proposed criterion in [2] has been used for the case of a solid phase surrounding pores. Two series of comparison have been realized for two sets of experimental data. The first one focuses on the behavior of sound and totally degraded cement paste in different confining pressure, while the other one focuses on the effects of lixiviation in different steps of degradation. Generally, the agreement between the numerical results and experimental data is found to be satisfactory. Further works could include extensions of the proposed model to time dependent behaviors.

Chapter 4

Multiscale Modeling of Concrete Behavior Subjected to Carbonation or Lixiviation

Contents

4.1 Introduction

In Chapter 3, two micro-macro models have been proposed to describe the non-linear behavior of cement paste with chemical degradations. The aim of this chapter is to extend the proposed models to the case of concrete. Three homogenization steps are made from microscale to macroscale based on the modified secant method, in order to numerically represent the macroscopic elastoplastic behavior of carbonated concrete. The macroscopic criterion takes into account the volume fraction of calcite grains (formed during carbonation process), the porosity and aggregates volume fraction. The same model can be applied for lixiviation. However there is an increase of porosity during decalcification. By taking a zero value for calcite grains volume fraction, the proposed model turns into the model derived by [99, 107] in case of a porous matrix reinforced by big inclusions. A non-associated plastic flow rule is also proposed for the transition from plastic compressibility to dilatancy. The proposed model is then implemented into a convenient Finite Element code which allows us to compare the main features of the mechanical behaviour of sound and degraded concrete with experimental data.

4.2 Micro-Macro Model for Concrete Carbonation

4.2.1 Microstructure of carbonated concrete

Concrete is a composite material consisting of aggregates (sand and gravel) and cement paste. Small calcite grains are also formed in the microstructure of concrete during carbonation. From this point of view, concrete is considered as a 4 phases composite material made of a solid phase representing cement, micro inclusions ($\sim \mu$m) representing calcite grains, mesopores (μm – mm) and meso inclusions (mm – cm) representing aggregates.

As shown in Fig. 4.1, at microscopic scale, the cement matrix is composed of an assembly of continuous cement particles (solid phase) which are reinforced by small inclusions (calcite grains) formed during carbonation process. At mesoscopic scale, concrete is a porous medium reinforced by big inclusions representing aggregates.

As a consequence, the macroscopic mechanical behavior depends on aggregates volume fraction, calcite grains formed during carbonation and change of porosity of cement paste. It is assumed that pores and inclusions are randomly distributed in space so that the macroscopic behavior remains isotropic. For the sake of simplicity, calcite grains,

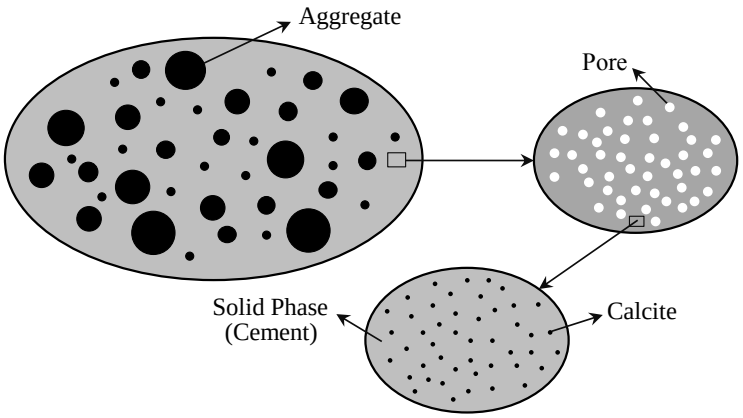

FIGURE 4.1: Representative volume element (RVE) of carbonated concrete

pores and aggregates are all assumed to be spherical. Inclusions are assumed to be rigid and have a perfect bounding with the surrounding matrix.

4.2.2 Macroscopic criterion of porous medium reinforced by small and big inclusions

A three-step homogenization procedure will be proposed for the formulation of a macroscopic plastic criterion for the studied composite. The first homogenization from micro to mesoscale is for the influence of calcite grains generated during carbonation. The effects of spherical pores and aggregates will be taken into account in the second and third homogenization from meso to macroscale (see Fig. 4.2). The volume fraction of calcite grains $CaCO_3$ (ρ_c) at microscale and the porosity (f) of the reinforced porous medium at mesoscale and aggregates volume fraction (ρ_a) at macroscale are given by:

$$\rho_c = \frac{\Omega_c}{\Omega_s + \Omega_c}, \quad f = \frac{\Omega_p}{\Omega_s + \Omega_c + \Omega_p}, \quad \rho_a = \frac{\Omega_a}{\Omega_s + \Omega_c + \Omega_p + \Omega_a} \tag{4.1}$$

where Ω_c, Ω_s, Ω_p and Ω_a are respectively volumes of calcite, solid phase in the matrix, pores of the reinforced porous medium and aggregates.

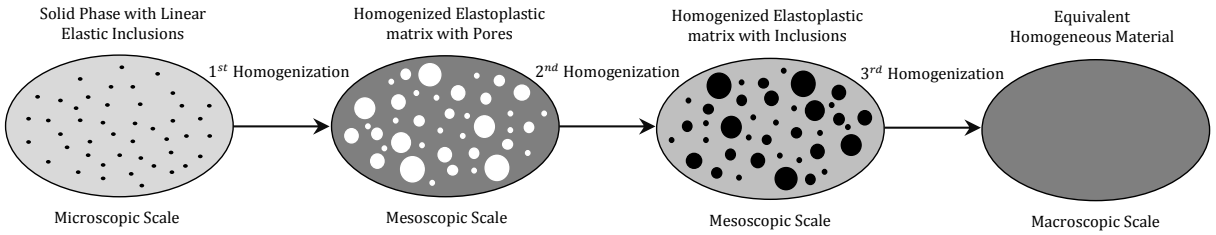

FIGURE 4.2: Schematic representation of homogenization procedure

4.2.2.1 First homogenization for the effect of calcite

For the first homogenization, the solid phase of the cement matrix is assumed to obey to a Drucker-Prager criterion:

$$\varphi^s(\boldsymbol{\sigma}) = \sigma_d + T(\sigma_m - h) \leq 0 \tag{4.2}$$

where $\boldsymbol{\sigma}$ is the local stress tensor of the solid phase at microscale, $\sigma_m = \frac{1}{3}\text{tr}\boldsymbol{\sigma}$ is the mean stress and $\sigma_d = \sqrt{\boldsymbol{\sigma}_d : \boldsymbol{\sigma}_d}$ is the equivalent stress (with $\boldsymbol{\sigma}_d = \boldsymbol{\sigma} - \sigma_m \mathbf{1}$). $\mathbf{1}$ is the second order identity tensor, h represents the hydrostatic tensile strength and T denotes the frictional coefficient. Due to contractant-dilatant behavior of geomaterials, a plastic potential is considered for the solid phase and is given by equation (4.3):

$$g^s(\boldsymbol{\sigma}) = \sigma_d + t\sigma_m \tag{4.3}$$

where t defines the dilatancy coefficient which controls volumetric plastic strains.

For a solid phase reinforced by rigid inclusions, we take advantage of results obtained by [2] who made use of a non linear homogenization technique based on the so-called modified secant method which was originally proposed by [108].

At the end of the first homogenization, the following criterion was obtained by [2] for a solid phase reinforced by rigid inclusions.

$$\varphi^{si} = \widetilde{\sigma}_d + \widetilde{T}(\widetilde{\sigma}_m - h) = 0 \tag{4.4}$$

$$g^{si} = \widetilde{\sigma}_d + \widetilde{t}\widetilde{\sigma}_m \tag{4.5}$$

where $\widetilde{T}$ and $\widetilde{t}$ are friction and dilation coefficients at mesoscale by considering the effect of calcite grains embedded into the solid phase. "si" superscript is used to indicate the reinforced matrix (solid phase + small inclusions generated during carbonation).

$$\widetilde{T} = T\sqrt{1 + \frac{3}{2}\rho_c}\ \ \frac{\sqrt{1 - \frac{2}{3}\rho_c t^2}}{1 - \frac{2}{3}\rho_c tT}; \qquad \widetilde{t} = t\sqrt{\frac{1 + \frac{3}{2}\rho_c}{1 - \frac{2}{3}\rho_c tT}} \tag{4.6}$$

Equation (4.6) shows that if the solid phase at microscale has a non-associated plastic behavior, then the reinforced matrix at mesoscale would also be non-associated.

4.2.2.2 Second homogenization for the effect of pores

For the second homogenization we are dealing with a reinforced matrix surrounding pores. By applying the normality rule to equation (4.5), one gets the strain rate in the reinforced matrix:

$$\boldsymbol{d} = d_d\left(\frac{\boldsymbol{\sigma}_d}{\sigma_d} + \frac{\widetilde{t}}{3}\mathbf{1}\right) \tag{4.7}$$

where, $d_d = \sqrt{\boldsymbol{d}_d : \boldsymbol{d}_d}$ and $\boldsymbol{d}_d = \boldsymbol{d} - d_m\mathbf{1}$ represents deviatoric part of $\boldsymbol{d}$ and $d_m = \frac{1}{3}\mathrm{tr}\boldsymbol{d}$.

The support function π^{si} can be determined with the help of a sequence of potentials ψ^a [109]. Then the stress-strain relationship can be derived from the support function. It is possible to rearrange in the form shown in equation (4.8). This requires the secant bulk and shear moduli and the isotropic prestress:

$$\widetilde{\boldsymbol{\sigma}} = \frac{\partial \pi^{si}}{\partial \boldsymbol{d}} = 2\mu^{si}\boldsymbol{d}_d + k^{si}d_v\mathbf{1} + \widetilde{\sigma}^p\mathbf{1} \tag{4.8}$$

where d_v is the local volume strain ($\mathrm{tr}\boldsymbol{d}$) and k^{si}, μ^{si} and $\widetilde{\sigma}^p$ are respectively bulk modulus, shear modulus and isotopic prestress of the reinforced matrix. The symbol "$\sim$" is used here for the mesoscopic stress field.

The non-linear behavior of the reinforced matrix is described by its dependence on the local volume and deviatoric strain rates d_v and d_d. The strain rate $\boldsymbol{d}(d_v, d_d)$ is non-uniform in the reinforced matrix. Consequently the moduli (k^{si}, μ^{si}) and the prestress $\widetilde{\sigma}^p$ are not uniform as well, making the reinforced matrix appear as a heterogeneous material. The idea is then to resort the so-called modified secant method proposed by [110]. This method is based on the concept of effective strain rate and on the implementation of a linear homogenization scheme in which the local behavior non-linearly depends on the loading parameters. In this method, given a macroscopic strain rate $\boldsymbol{D}$ the effective values of deformation invariants, d_v and d_d are calculated:

$$d_v^e = \sqrt{\langle d_v^2\rangle_{\Omega_{si}}}\ ; \quad d_d^e = \sqrt{\langle d_d^2\rangle_{\Omega_{si}}} \tag{4.9}$$

Then the bulk and shear moduli and the prestress can be expressed in terms of the equivalent strain $\boldsymbol{d}^e$:

$$\text{For any } x \in \Omega_{si}: \quad \begin{aligned} \mu^{si}(\boldsymbol{d}(x)) &= \mu^{si}(\boldsymbol{d}^e) = \mu^{si}_{eq} \\ k^{si}(\boldsymbol{d}(x)) &= k^{si}(\boldsymbol{d}^e) = k^{si}_{eq} \\ \widetilde{\sigma}^p(\boldsymbol{d}(x)) &= \widetilde{\sigma}^p(\boldsymbol{d}^e) = \widetilde{\sigma}^p_{eq} \end{aligned}$$

The homogenized behavior can now be written in this form:

$$\widetilde{\boldsymbol{\Sigma}} = \mathbb{C}^{mp} : \boldsymbol{D} + \widetilde{\Sigma}^p \mathbf{1} \tag{4.10}$$

$$\mathbb{C}^{mp}(d^e_v, d^e_d) = 3k^{mp}(k^{si}_{eq}, \mu^{si}_{eq})\mathbb{J} + 2\mu^{mp}(k^{si}_{eq}, \mu^{si}_{eq})\mathbb{K} \tag{4.11}$$

where $\tilde{\boldsymbol{\Sigma}}$ is the stress field of the porous matrix. $\mathbb{J} = \frac{1}{3}\mathbf{1} \otimes \mathbf{1}$ and $\mathbb{K} = \mathbb{I} - \mathbb{J}$ are respectively the isotropic symmetric forth order spherical and deviatoric operators, $\mathbf{1}$ and $\mathbb{I}$ are respectively the second and forth order identity tensors. The superscript "mp" indicates a matrix surrounding pores.

The elastic properties of a porous medium are related to those of its matrix and affected by its porosity. For this purpose we adopt the Hashin-Shtrikman [111] upper bounds which are known to reasonably model the linear elastic properties of isotropic porous media (this corresponds to the Mori-Tanaka homogenization scheme):

$$k_{mp} = k^{si}_{eq} \frac{4(1-f)\mu^{si}_{eq}}{3fk^{si}_{eq} + 4\mu^{si}_{eq}} \qquad \mu^{mp} = \mu^{si}_{eq} \frac{(1-f)(9k^{si}_{eq} + 8\mu^{si}_{eq})}{k^{si}_{eq}(9+6f) + \mu^{si}_{eq}(8+12f)} \tag{4.12}$$

The prestress in the homogenized behavior of (4.11) is deduced from the Levins's theorem:

$$\widetilde{\Sigma}^p = \frac{k^{mp}}{k^{si}_{eq}} \widetilde{\sigma}^p_{eq} \tag{4.13}$$

The state equation can now be expressed as:

$$\widetilde{\Sigma}_m = k^{mp} D_v + \widetilde{\Sigma}^p, \qquad \widetilde{\Sigma}_d = 2\mu^{mp} D_d \tag{4.14}$$

For a porous medium, the effective strain rates in the reinforced matrix are related to $\boldsymbol{D}$ [112]:

$$\frac{1}{2}(1-f)d_v^{e\,2} = \frac{1}{2}\frac{\partial k^{mp}}{\partial k_{eq}^{si}}\left(D_v + \frac{\tilde{\Sigma}_{eq}^{p}}{k_{eq}^{si}}\right)^2 - \frac{k^{mp}}{k_{eq}^{si\,2}}\tilde{\Sigma}_{eq}^{p} D_v + \frac{1}{2}\left(1-f-2\frac{k^{mp}}{k_{eq}^{si}}\right)\left(\frac{\tilde{\Sigma}_{eq}^{p}}{k_{eq}^{si}}\right)^2 + \frac{\partial \mu^{mp}}{\partial k_{eq}^{si}} D_d^2$$

$$(1-f)d_d^{e\,2} = \frac{\partial k^{mp}}{\partial \mu_{eq}^{si}}\left(D_v + \frac{\tilde{\Sigma}_{eq}^{p}}{k_{eq}^{si}}\right)^2 + \frac{\partial \mu^{mp}}{\partial \mu_{eq}^{si}} D_d^2 \tag{4.15}$$

By using equations (4.12), (4.13), (4.15) into equation (4.14) and making mathematical juggling inspired from the approach used in [2], the following criterion of the porous medium with reinforced matrix can be obtained [1].

$$\varphi^{mp} = \frac{1+\frac{2}{3}f}{\widetilde{T}^2}\,\widetilde{\Sigma}_d^2 + \left(\frac{3f}{2\widetilde{T}^2} - 1\right)\widetilde{\Sigma}_m^2 + 2(1-f)h\widetilde{\Sigma}_m - (1-f)^2h^2 = 0 \tag{4.16}$$

4.2.2.3 Third homogenization for the effect of aggregates

Similarly to [2, 99] by calculating the strain rate and the support function π^{mp} and by making an effective average for deviatoric and volume deformations, the macroscopic criterion can be obtained.

Here, we take advantage of equation (4.16) to quantify the effect of aggregates on the macroscopic criterion of concrete. An associated plastic flow rule is also considered. Based on the criterion (4.16), the rate of deformations in the porous medium can be written as follows:

$$\widetilde{\boldsymbol{d}} = \frac{\widetilde{T}^2}{1+\frac{2f}{3}}\frac{\widetilde{d}_d}{2\widetilde{\Sigma}_d}\left[\frac{1+\frac{2f}{3}}{\widetilde{T}^2}2\widetilde{\boldsymbol{\Sigma}}_d + \left(\frac{3f}{2\widetilde{T}^2}-1\right)\frac{2}{3}\widetilde{\Sigma}_m\mathbf{1} + \frac{2(1-f)h}{3}\mathbf{1}\right] \tag{4.17}$$

The support function of the criterion (4.16) can be calculated as follow:

[1] More details can be found in [2]

$$\begin{aligned}\pi^{mp}(\widetilde{\boldsymbol{d}}) &= \widetilde{\boldsymbol{\Sigma}} : \widetilde{\boldsymbol{d}} \\ &= \frac{\widetilde{T}^2}{1+\frac{2f}{3}}\frac{\widetilde{d}_d}{2\widetilde{\Sigma}_d}\left[\frac{1+\frac{2f}{3}}{\widetilde{T}^2}2\widetilde{\Sigma}_d^2+\left(\frac{3f}{2\widetilde{T}^2}-1\right)2\widetilde{\Sigma}_m^2+2(1-f)h\widetilde{\Sigma}_m\right] \\ &= (1-f)h\sqrt{\frac{3f}{3f-2T^2}\frac{T^2}{1+\frac{2f}{3}}}\sqrt{\widetilde{d}_d^2+\frac{1+\frac{2f}{3}}{\frac{3f}{2}-T^2}\widetilde{d}_v^2}-(1-f)h\frac{2T^2}{3f-2T^2}\widetilde{d}_v\end{aligned} \tag{4.18}$$

In line with the approach proposed by [2], the state equation can be expressed by means of secant modulus and a spherical prestress:

$$\widetilde{\boldsymbol{\Sigma}} = \frac{\partial \pi^{mp}}{\partial \boldsymbol{d}} = 2\mu^{mp}\widetilde{\boldsymbol{d}}_d + k^{mp}\widetilde{d}_v\mathbf{1} + \widetilde{\Sigma}^p\mathbf{1} \tag{4.19}$$

$$\begin{aligned}&\mu^{mp} = \frac{N}{2M}; \quad k^{mp} = B\frac{N}{M}; \quad \widetilde{\Sigma}^p = -(1-f)h\frac{2T^2}{3f-2T^2} \\ &N = (1-f)h\sqrt{\frac{3f}{3f-2T^2}\frac{T^2}{1+\frac{2f}{3}}}; \quad M = \sqrt{\widetilde{d}_d^2+B\widetilde{d}_v^2}; \quad B = \frac{1+\frac{2f}{3}}{\frac{3f}{2}-T^2}\end{aligned} \tag{4.20}$$

Again the effective volume and deviatoric strain rates should be calculated for the porous matrix by means of the modified secant method to capture the effect of loading on non-linear properties:

$$d_v^{eff} = \sqrt{\langle\widetilde{d}_v^2\rangle_{\Omega_{mp}}}\ ; \quad d_d^{eff} = \sqrt{\langle\widetilde{d}_d^2\rangle_{\Omega_{mp}}} \tag{4.21}$$

Using effective deformations to calculate bulk and shear moduli and the prestress in terms of the equivalent strain $\boldsymbol{d}^{eff}$, the homogenized behavior can be described by:

$$\boldsymbol{\Sigma} = \mathbb{C}^{hom} : \boldsymbol{D} + \Sigma^p\mathbf{1} \tag{4.22}$$

$$\mathbb{C}^{hom}(d_v^e, d_d^e) = 3k^{hom}(k_{eq}^{mp}, \mu_{eq}^{mp})\mathbb{J} + 2\mu^{hom}(k_{eq}^{mp}, \mu_{eq}^{mp})\mathbb{K} \tag{4.23}$$

where $\boldsymbol{\Sigma}$ is the macroscopic stress field and Σ^p is the macroscopic isotropic prestress. The assumption of rigid inclusions and consideration of homogeneous behavior makes it possible to demonstrate that the macroscopic prestress Σ^p is equal to $\widetilde{\Sigma}_{eq}^p$ and $\widetilde{\Sigma}^p$. The macroscopic potential of composite can be written in the following form:

$$W = \frac{1}{2}\boldsymbol{D} : \mathbb{C}^{hom} : \boldsymbol{D} + \Sigma^p \mathrm{tr}\boldsymbol{D} \tag{4.24}$$

The corresponding state equations are expressed as:

$$\Sigma_m = k^{hom} D_v + \Sigma^p \; ; \quad \Sigma_d = 2\mu^{hom} D_d \tag{4.25}$$

Following [109], relation between the effective strain rates in the porous matrix and the loading is described by:

$$\begin{aligned} \frac{1}{2}(1-\rho) d_v^{eff\,2} &= \frac{1}{2}\frac{\partial k^{hom}}{\partial k_{eq}^{mp}} D_v^2 + \frac{\partial \mu^{hom}}{\partial k_{eq}^{mp}} D_d^2 \\ (1-\rho) d_d^{eff\,2} &= \frac{1}{2}\frac{\partial k^{hom}}{\partial \mu_{eq}^{mp}} D_v^2 + \frac{\partial \mu^{hom}}{\partial \mu_{eq}^{mp}} D_d^2 \end{aligned} \tag{4.26}$$

Because of matrix inclusion morphology, the homogenized secant moduli k^{hom} and μ^{hom} are evaluated by Mori-Tanaka scheme:

$$\begin{aligned} k^{hom} &= \frac{3k_{eq}^{mp} + 4\rho\mu_{eq}^{mp}}{3(1-\rho)} \\ \mu^{hom} &= \mu_{eq}^{mp} \frac{k_{eq}^{mp}(6+9\rho) + \mu_{eq}^{mp}(12+8\rho)}{6(1-\rho)(k_{eq}^{mp} + 2\mu_{eq}^{mp})} \end{aligned} \tag{4.27}$$

Introducing (4.20) and (4.27) into (4.26) one gets:

$$\begin{aligned} d_v &= \sqrt{\frac{Dv^2}{(1-\rho)^2} + \frac{10\rho\, Dd^2}{3\,(1-\rho)^2\,(2\,B+2)^2}} \\ d_d &= \sqrt{\frac{2\rho\, Dv^2}{3\,(1-\rho)^2} + \frac{(4\,(6+9\,\rho)\,B^2 + (16\,\rho+24)\,(2\,B+1))\,Dd^2}{6\,(1-\rho)^2\,(2\,B+2)^2}} \end{aligned} \tag{4.28}$$

Using equations (4.20), (4.25), (4.27) and (4.28), the macroscopic criterion can be obtained in the following form:

$$F = \frac{\frac{1+\frac{2}{3}f}{\widetilde{T}^2} + \frac{2}{3}\rho_a\left(\frac{3f}{2\widetilde{T}^2} - 1\right)}{\frac{4\widetilde{T}^2-12f-9}{6\widetilde{T}^2-13f-6}\rho_a + 1}\Sigma_d^2 + \left(\frac{3f}{2\widetilde{T}^2} - 1\right)\Sigma_m^2 + 2(1-f)h\Sigma_m - \left(\frac{3f\rho_a}{3+2f} + 1\right)(1-f)^2h^2 = 0 \tag{4.29}$$

Inspired from [2], [107] a non-associate plastic flow rule is proposed here in order to describe the volume deformations observed in experimental investigations on geomaterials :

$$G = \frac{\frac{1+\frac{2}{3}f}{\widetilde{T}\widetilde{t}} + \frac{2}{3}\rho_a\left(\frac{3f}{2\widetilde{T}\widetilde{t}} - 1\right)}{\frac{4\widetilde{T}\widetilde{t}-12f-9}{6\widetilde{T}\widetilde{t}-13f-6}\rho_a + 1}\Sigma_d^2 + \left(\frac{3f}{2\widetilde{T}\widetilde{t}} - 1\right)\Sigma_m^2 + 2(1-f)h\Sigma_m - \left(\frac{3f\rho_a}{3+2f} + 1\right)(1-f)^2h^2 \tag{4.30}$$

4.2.3 Elastoplastic behavior

The macroscopic plastic criterion (4.29) is now applied to describe the elastoplastic behavior of sound and carbonated concrete, taking into account the effects of cement paste, porosity, calcite grains and aggregates.

The plastic hardening is taken into account via the evolution of the frictional coefficient T and dilatancy parameter t as a function of the equivalent plastic strain ε^p.

$$\hat{T} = T_m - (T_m - T_0)e^{-b_1\varepsilon^p}; \qquad \hat{t} \;=\; t_m - (t_m - t_0)e^{-b_2\varepsilon^p} \tag{4.31}$$

where T_0 and T_m are respectively the initial threshold and asymptotic values for the frictional coefficient of cement matrix and t_0 and t_m are parameters describing the transition between volumetric contraction and dilatancy.

The evolution of plastic parameters are given in the following equations:

$$\boldsymbol{D}^p = \dot{\lambda}\frac{\partial G}{\partial \boldsymbol{\Sigma}}(\boldsymbol{\Sigma}, \rho_c, f, \rho_a, \hat{T}, \hat{t}) \tag{4.32}$$

Where $\boldsymbol{D}^p$ is the macroscopic plastic strain rate and $\dot{\lambda}$ is the plastic multiplier.

$$\begin{cases} \dot{\lambda} = 0 & \text{if} \quad F < 0 \quad \text{or if} \quad F = 0 \quad \text{and} \quad \dot{F} \leq 0 \\ \dot{\lambda} \geq 0 & \text{if} \quad F = 0 \quad \text{and} \quad \dot{F} > 0 \end{cases} \tag{4.33}$$

According to (4.2), evolution of the stress flow in the porous matrix can be written as follows:

$$\boldsymbol{\Sigma} : \boldsymbol{D}^p = \frac{1}{\Omega}\int_{\Omega_s} \boldsymbol{\sigma} : \boldsymbol{d}\, d\Omega = \frac{1}{\Omega}\int_{\Omega_s} \dot{\varepsilon}^p \left(\hat{T}h + (\hat{t} - \hat{T}\sigma_m\right) \tag{4.34}$$

The equivalent plastic deformation of the solid matrix is given by equation (4.34).

$$\dot{\varepsilon}^p = \frac{\Sigma : D^p}{(1-f)(1-\rho_a)(1-\rho_c)\left[\hat{T}h + (\hat{t}-\hat{T})\dfrac{\Sigma_m}{(1-f)(1-\rho_a)(1-\rho_c)}\right]} \tag{4.35}$$

The evolution of porosity and inclusions during loading is determined as:

$$\dot{\rho_c} = -\rho_c(1-\rho_c)\hat{t}\dot{\epsilon}^p; \quad \dot{\rho_a} = -\rho_a \,\mathrm{tr}D^p \tag{4.36}$$

$$\dot{f} = \frac{1-f}{1-\rho_a}\mathrm{tr}D^p - (1-f)(1-\rho_c)\hat{t}\dot{\epsilon}^p \tag{4.37}$$

4.2.4 Parameter analysis of the model

To better understand the behavior of the proposed model, we need to analyse the influence and sensitivity of parameters on the mechanical behavior. This is performed in three different parts. The first analysis is conducted on the effect of material properties to the failure criterion. The second analysis emphasizes the difference between associated and non-associated plastic flow rule on the mechanical behavior. Finally, because this model can be applied to 4 phases rock-like materials with two different inclusions sizes like concrete, it is convenient to analyse the behavior of the model under different confining pressures.

4.2.4.1 Sensitivity of material properties on the macroscopic criterion

In Fig. 4.3 to Fig. 4.7 the effect of porosity, small inclusions, big inclusions, friction coefficient and the hydrostatic tensile strength are analysed for the macroscopic criterion (4.29). The reference values for these parameters used here are given in Table 4.1. As it is shown in these figures, the macroscopic criterion has an elliptic form due to the effect of pores. However, when the porosity tends to 0 ($f \to 0$) or when the friction coefficient increases significantly, we approach to the Drucker-Prager criterion (see Fig. 4.3 and Fig. 4.6).

f	ρ_c	ρ_a	T	h
0.2	0.3	0.3	0.3	10

TABLE 4.1: Model parameters used for sensitivity analysis

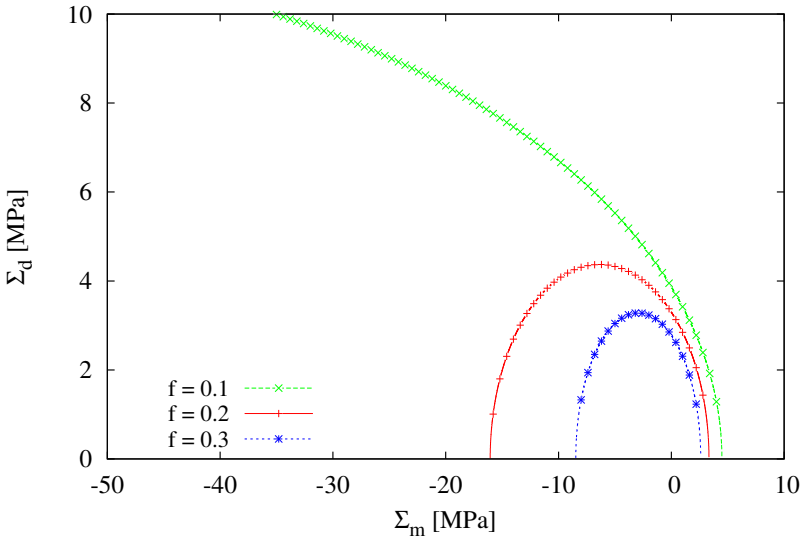

FIGURE 4.3: Effect of the porosity on the failure criterion

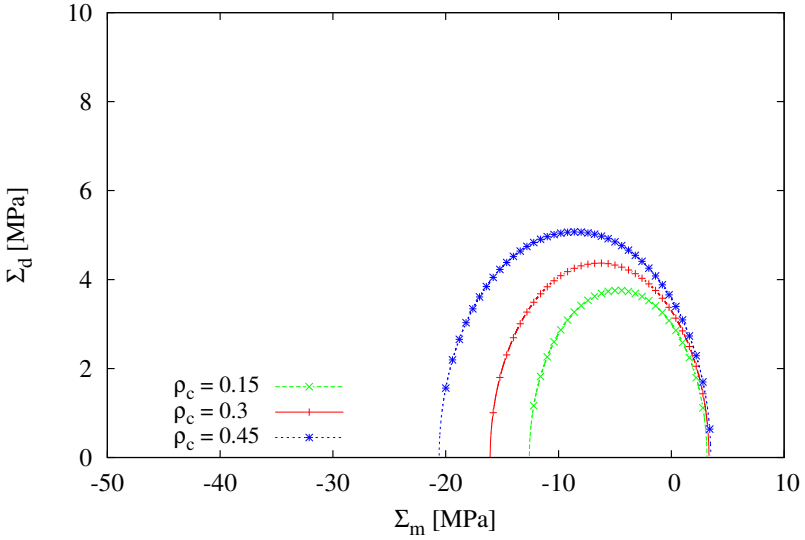

FIGURE 4.4: Effect of the small inclusions on the failure criterion

4.2.4.2 Effect of the non-associated plastic flow rule on mechanical response

The simulations here are performed using the set of parameters given in Table 4.4 with $f = 0.234$, $\rho_c = 0.08$ and $\rho_a = 0.67$. Fig. 4.8(a) shows the stress-strain behavior, which overestimates the lateral strain and volumetric dilatancy. Such a result can be mainly explained by the fact that an associated flow rule is used in the plastic modeling of the composite. This is mainly because the yield criterion generally provides overall too stiff yield stresses. To overcome this problem a non-associated plastic flow rule (4.30) has been proposed. Fig. 4.8(b) shows the ability of the model to take into account the

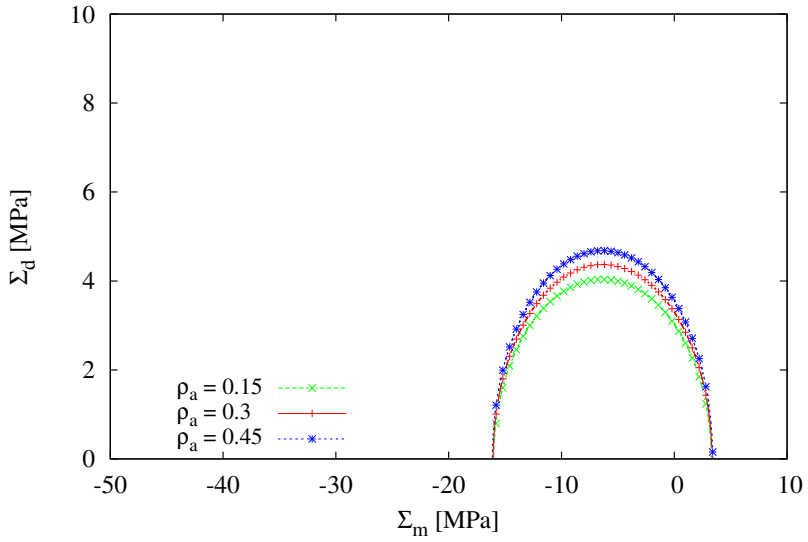

FIGURE 4.5: Effect of big inclusions on the failure criterion

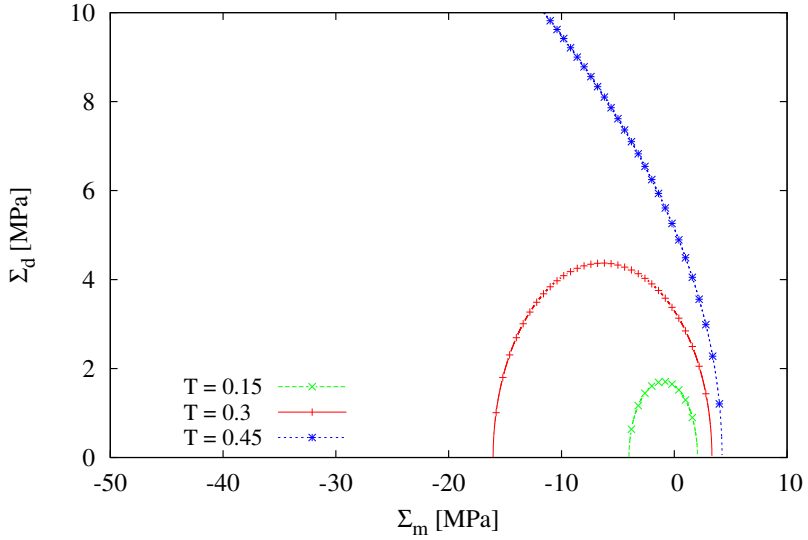

FIGURE 4.6: Effect of frictional coefficient on the failure criterion

contractant behavior seen in geomaterials at the first stages of loading and a transition to dilatant behavior at the end stages of loading.

Fig. 4.9 shows the differences between associated and non-associated model during loading (evolution of volume deformations, porosity, small and big inclusions). Fig. 4.9(a) clearly shows that if a non-associated behavior is adopted for the solid phase (4.3), the macroscopic behavior is also non-associated. Fig. 4.9(c) and Fig. 4.9(d) reflect the change of the volume fraction of small and big inclusions. It seems that inclusions are increasing in the sample when using a non-associated flow rule and then they start to

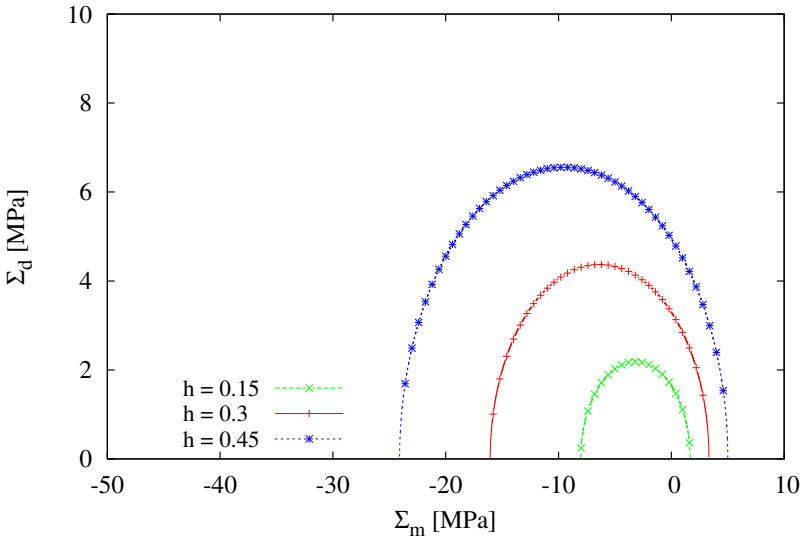

FIGURE 4.7: Effect of the hydrostatic tensile strength on the failure criterion

decrease. This is due to the fact that the solid phase contracts more by using a non-associated flow rule, so its volume decreases making artificially appear that inclusions volume increase during loading. Because the dilation is less pronounced for the solid phase of a non-associated model, a moderate decrease of porosity, small and big inclusions volume fraction is observed during loading with a non-associated model (see Fig. 4.9(b), Fig. 4.9(c) and Fig. 4.9(d)). This explains the noticeable difference between maximum value of the deviatoric stress of the associated and non-associated model (see Fig. 4.8(a) and Fig. 4.8(b)). In fact, when dilation is more pronounced (in case of associated flow rule), the porosity decreases faster, hence, material strength reaches biggest values.

4.2.4.3 Effect of confining pressure on the evolution of plastic behavior

Fig. 4.10 shows the effect of confining pressure on the evolution of volume deformations, porosity, small and big inclusions. The results correspond to those expected. Moreover, as we can see in Fig. 4.10(a), for a given strain, the dilatancy is higher at lower confining pressure. This has been seen in a lot of studies for geomaterials, for instance [113, 114].

4.2.5 Experimental validation of the proposed model

The proposed model is implemented into THMpasa Finite Element code developed in our laboratory. The experimental data of Chang and al. [52] presented in Chapter 1 are

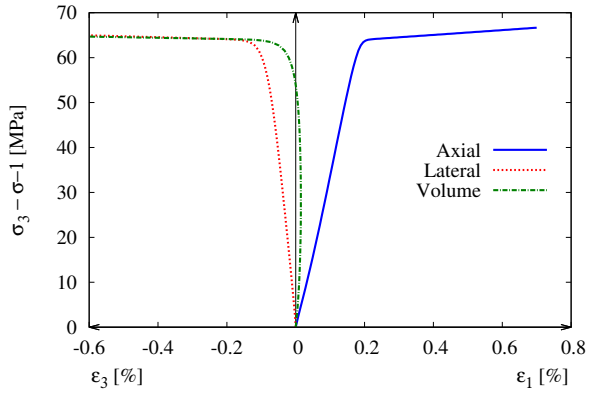

(a) associated plastic flow rule; $T_0 = t_0 = 0.03$, $T_m = t_m = 0.91$

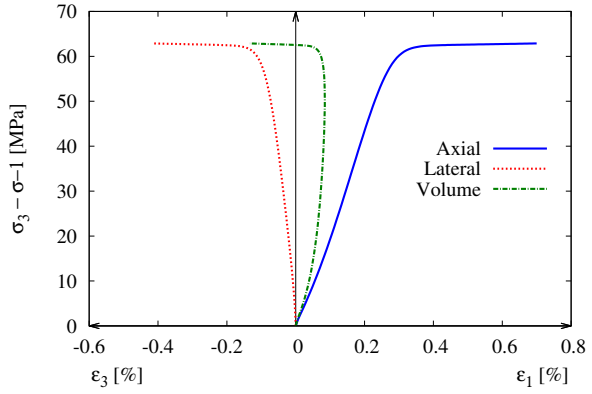

(b) non-associated plastic flow rule; $T_0 = 0.03$, $T_m = 0.91$, $t_0 = -1$, $t_m = 0.5$

FIGURE 4.8: stress-strain behavior comparison between associated and non-associated plastic flow rule

used for modeling purposes. Table 4.2 shows the composition of concrete and density of each constituents.

	kg/m^3			
	Cement	Water	Coarse Aggregate	Fine Aggregate
Mixture Proportion	307	200	1035	745
Density	3120	1000	2650	2630

TABLE 4.2: Mixture proportion and density [115]

The volume fraction of calcite grains at microscale and mesoscale porosity needed for numercial simulations can then be calculated from equation (4.1). This is done by taking into account the decrease in porosity due to the effect of hydration that occurs during carbonation process (see Fig. 1.8). The volume fraction of aggregates can be determined knowing the density of concrete constituents.

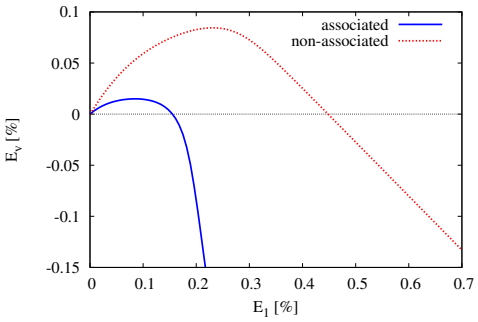

(a) Volume deformation E_v

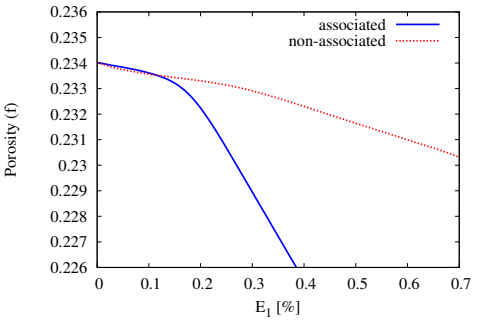

(b) Porosity f

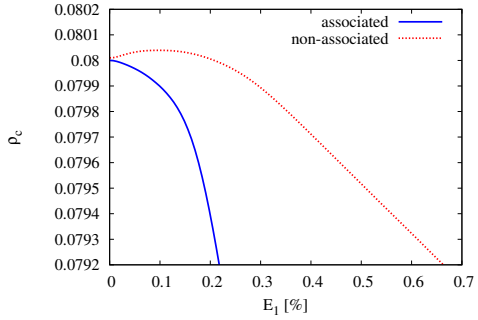

(c) Small inclusions volume fraction ρ_c

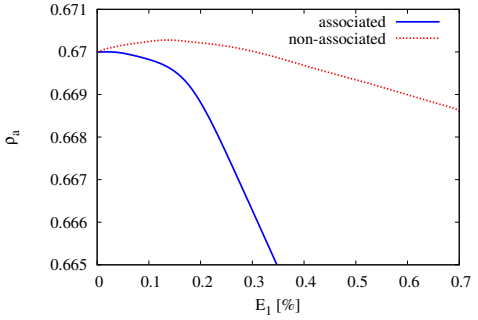

(d) Big inclusions volume fraction ρ_a

FIGURE 4.9: Difference between associated and non-associated behavior during loading

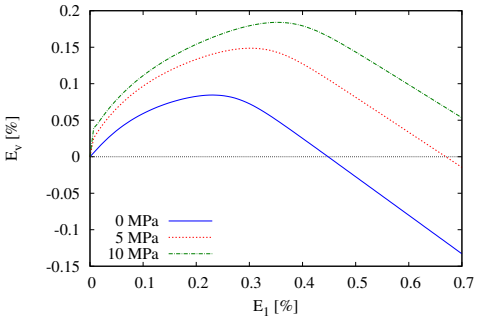

(a) Volume deformation E_v

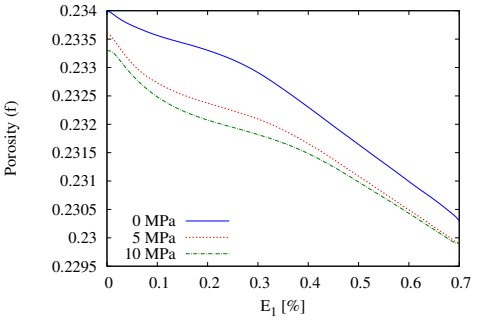

(b) Porosity f

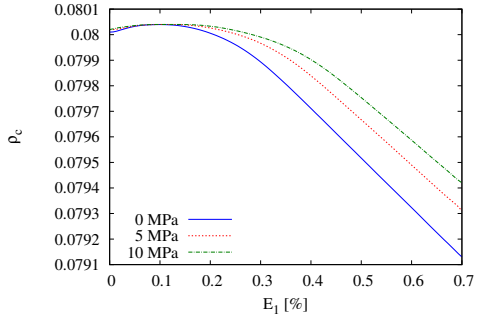

(c) Small inclusions volume fraction ρ_c

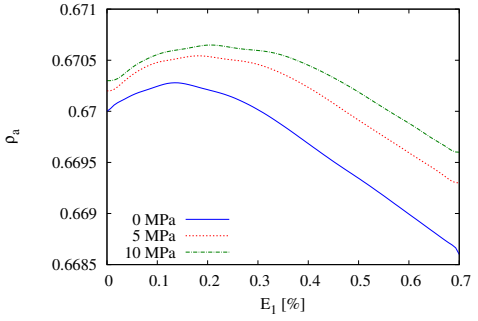

(d) Big inclusions volume fraction ρ_a

FIGURE 4.10: Effect of confining pressure on a non-associated behavior during loading

$$\Omega_{ca} = 0.39\ m^3\ ; \quad \Omega_{fa} = 0.28\ m^3 \tag{4.38}$$

where, "ca" and "fa" stands for coarse aggregate and fine aggregate. To simplify, their sum is taken as the volume of aggregates; $\Omega_a = 0.67\ m^3$. Calcites, pores and aggregates volume fractions for each state of carbonation using (4.1) and (4.38) are recapped in table 4.3. They are employed into the macroscopic criterion (4.29) by considering a frictional coefficient $T = 0.91$ and a hydrostatic tensile strength $h = 15$ MPa (table 4.4) for the cement phase (4.2).

Carbonation	0%	25%	42%	66%	84%	100%
Calcite volume fraction of the matrix (ρ_c)	0	0.129	0.188	0.228	0.234	0.239
Porosity of the reinforced matrix Matrix (f)	0.385	0.316	0.291	0.269	0.252	0.234
Aggregates volume fraction of concrete (ρ_a)	0.67	0.67	0.67	0.67	0.67	0.67

TABLE 4.3: Calcite, porosity and aggregates volume fraction of concrete

	Cement	Calcite	Aggregate
Elastic Parameters	$E_s = 27$ GPa	$E_c = 95$ GPa	$E_a = 75$ GPa
	$\nu_s = 0.27$	$\nu_c = 0.3$	$\nu_a = 0.2$
Plastic Parameters	$T_0 = 0.3$		
	$T_m = 0.91$		
	$b_1 = 750$		
	$h = 15$ MPa		

TABLE 4.4: Set of Parameters for sound to carbonated samples

As explained earlier, carbonated concrete is supposed to be composed of a solid phase, pores and two different types of inclusions. Each of these phases has its proper elastic moduli. Because of the changes of the microstructure throughout carbonation, the overall elastic moduli or effective elastic moduli of concrete also changes. Considering these phases to be isotropic and their distribution being random and homogeneous, a Mori-Tanaka scheme [116] is adopted here to evaluate the homogenized elastic moduli of concrete.

Elastic properties of cement, calcite and aggregates are crucial for numerical simulations. As there is no precise data and direct measurement on elastic properties of the solid phase of cement paste at microscopic scale, a close approximation on elastic properties will be made by using the inverse linear procedure of Mori-Tanaka method. According to experimental results of Haecker and al. [87] on a cement paste similar to the one used in Chang and al. [52] study, a macroscopic elastic modulus of about 12000 MPa could be assumed for W/C=0.65. As the porosity of this cement paste at mesoscale is known, $f = 0.385$, the elastic properties of the solid phase can be obtained by using Mori-Tanaka homogenization scheme [116] which corresponds to the upper bound of Hashin and Shtrikman [111]:

$$k_m = \frac{4(1-f)k_s\mu_s}{4\mu_s + 3fk_s}; \quad \mu_m = \frac{(1-f)\mu_s}{1 + 6f\frac{k_s+2\mu_s}{9k_s+8\mu_s}} \tag{4.39}$$

Using the above mentioned procedure, one obtains the following typical values for the solid phase of cement matrix: $k_s = 20.1$ GPa, $\mu_s = 10.6$ GPa or equivalently $E_s = 27$ GPa and $\nu_s = 0.27$.

$E_c = 95$ GPa and $\nu_c = 0.3$ are taken as elastic parameters of calcite grains. More details are given in Appendix C. Chang and al. [52] used river sand and coarse aggregates to fabricate the concrete. The elastic modulus and Poisson's ratio of aggregates (big inclusions) are assumed to be $E_a = 75$ GPa and $\nu_a = 0.2$ according to some data found [117–119].

Numerical simulations have been performed using the set of parameters from tables 4.3 and 4.4. Note that as there is no data of the lateral behavior of the concrete under uniaxial compression only the associated model is used ($T = t$).

Fig. 4.11 shows the effect of the microstructural change during carbonation on the macroscopic failure criterion (4.29).

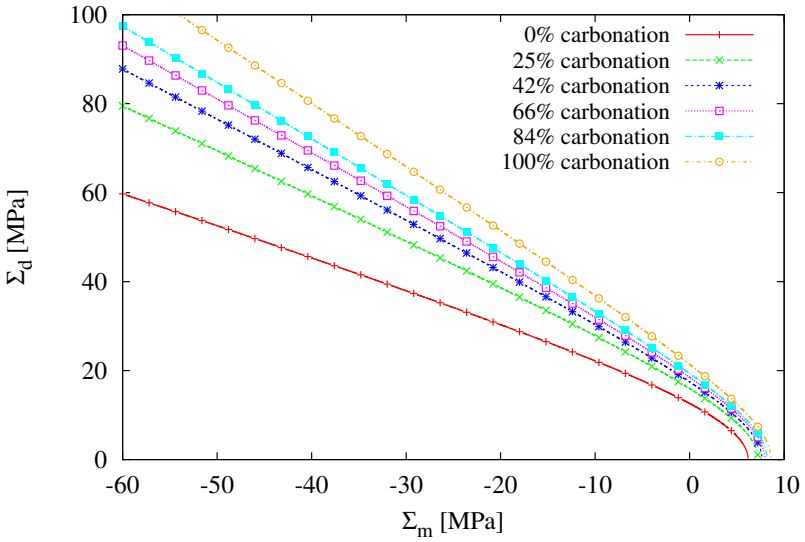

FIGURE 4.11: Failure envelopes for sound and carbonated concrete

Fig. 4.12 shows comparison between experimental stress-strain results and predictions of the model. We can see that the model is able to take into account the overall elastoplastic behavior of concrete during carbonation. Comparisons show a good agreement between experimental data and strength predictions of the model (see Fig. 4.13).

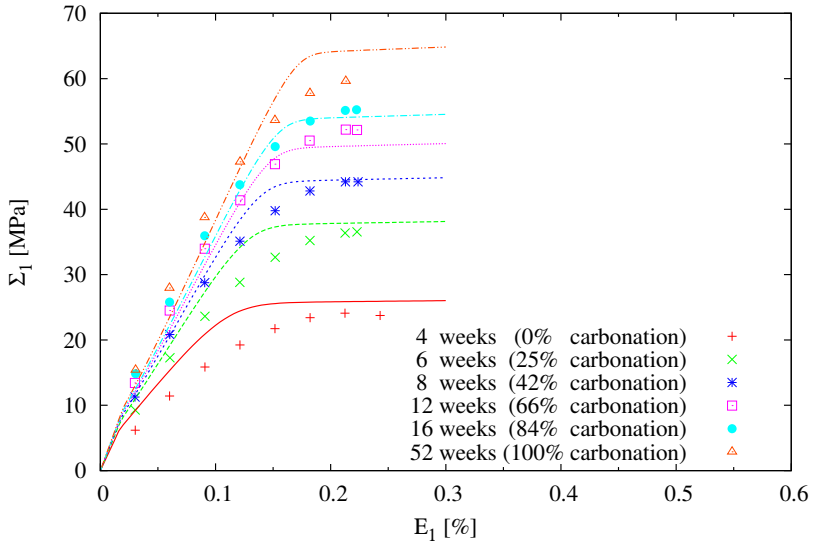

FIGURE 4.12: stress-strain relationship of sound and carbonated concrete

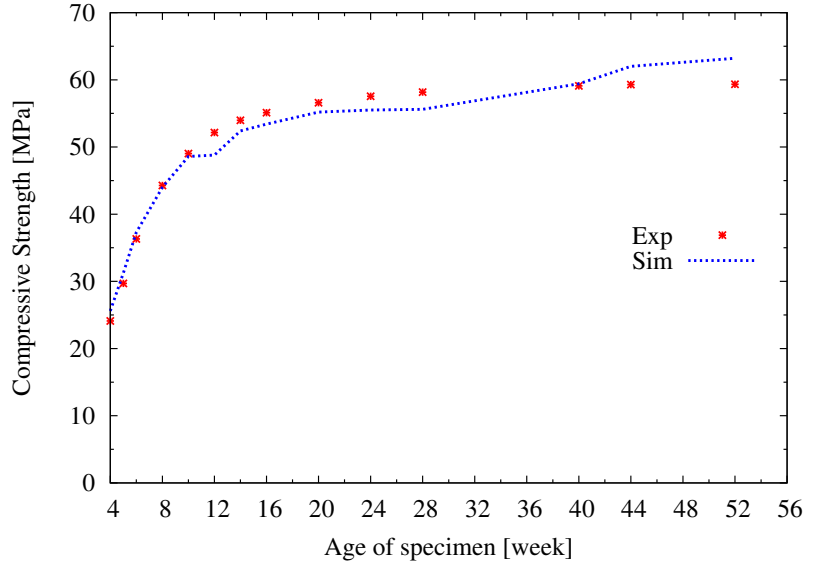

FIGURE 4.13: Relationship between compressive strength and carbonation of concrete taking into account the effects of hydration

Moreover, the evolution of Young's modulus as a function of carbonation predicted by the model (that uses the Mori-Tanaka scheme) is presented in Fig. 4.14. The effect of carbonation is correctly taken into account.

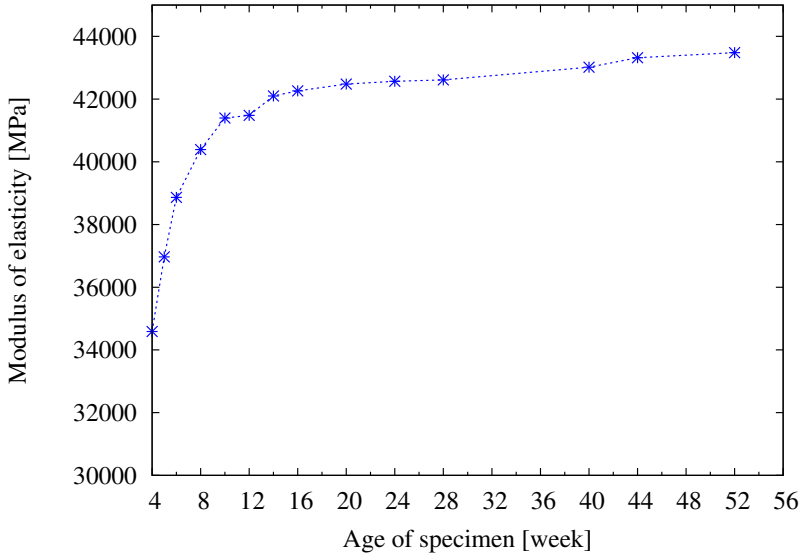

FIGURE 4.14: Model prediction of the evolution of elasticity modulus with carbonation of concrete taking into account the effect of hydration

4.3 Micro-Macro Model for Concrete Lixiviation

4.3.1 Microstructure of leached concrete

In general concrete can be assumed as a three phase material composed of aggregate particles dispersed in a porous cement matrix. An important simplification here is that we replaced sand and gravel into equivalent randomly distributed spherical inclusions so that the global behavior remains isotropic. The effect of lixiviation on concrete is to increase porosity by leaching the calcium of cement paste hydrates.

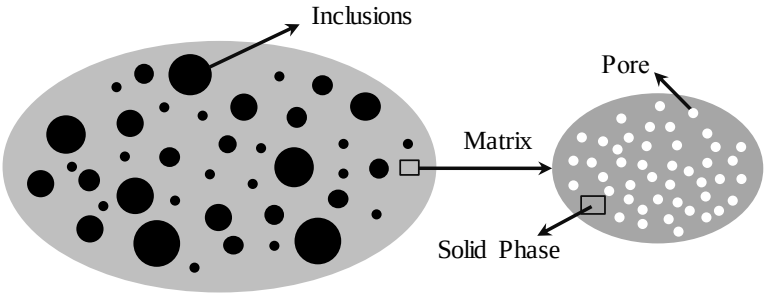

FIGURE 4.15: Representative volume element of concrete

Considering this RVE and the effect of lixiviation on it, we can use the same criterion introduced in section 4.2.2.3 by eliminating small inclusions that reinforce the matrix. In this case, the criterion obtained coincides exactly to the criterion obtained by [99] for a porous medium reinforced by rigid inclusions.

4.3.2 Experimental validation

For lixiviation the results obtained by [63, 71] are used to assess the mechanical behavior with chemical degradation (see Chapter 1). Table 4.5 presents the composition of concrete which has a W/C=0.6. The volume fraction of coarse aggregates, fine aggregates and cement paste are 40%, 26% and 34% respectively. Thus, the aggregates represent 66% of the total volume.

kg/m^3			
Cement	Water	Coarse Aggregate	Fine Aggregate
375	225	1050	684

TABLE 4.5: Composition of concrete [63]

Water porosity of cement paste at sound state is 39.3% and at totally degraded states is 68.7%. The porosity has not been measured in different intervals of degradation. However, we need to know the porosity for each state of degradation to make simulations. According to [74], the increase in water porosity is a linear function of the degradation ratio of cement paste. Knowing water porosity at sound and degraded states, and degradation ratio for each state of lixiviation we can obtain a value close to the real porosity of cement paste for each state. Parameters used for simulations are presented in table 4.6. Once again, due to the lack of lateral deformations we will only use the associated model ($T = t$).

Parameters	Sound	Degraded [%]				
		55	74	84	97	100
Elastic	E_s=40000 MPa; ν_s=0.3; E_a=75000 MPa; ν_a=0.2					
Plastic	T_m=1	T_m=1	T_m=1	T_m=1	T_m=1	T_m=0.9
	T_0=0.01 ; b_1=2250 ; h=20 MPa					
Porosity [%]	39.3	53	58	63	67.5	68.7
Aggregates [%]	66	66	66	66	66	66

TABLE 4.6: Set of parameters used for simulations of concrete lixiviation

Fig. 4.16 shows the effect of the chemical degradation (by NH_4NO_3 solution) leading to porosity increase on the failure criterion.

A comparison of stress- strain curves from experiments and simulations are shown in Fig. 4.17 for each state of degradation. The experimentally obtained Young's modulus are compared with predictions in Fig. 4.18. The effective Concrete Young's modulus is obtained by a Mori-Tanaka homogenization scheme. These comparisons show the ability of the model to take into account the evolution of strength and stiffness from sound to totally degraded state.

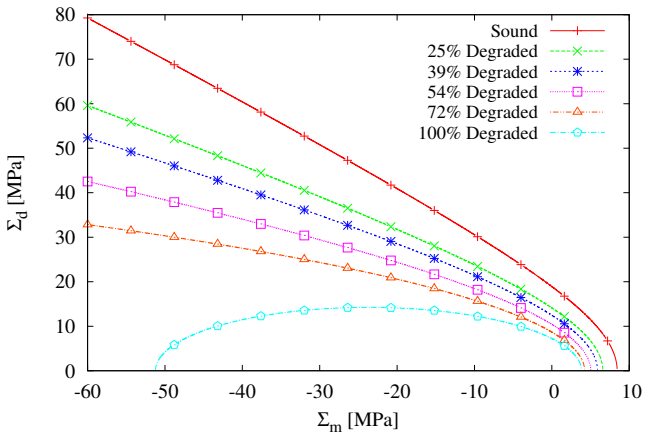

FIGURE 4.16: Failure envelopes for sound and leached concrete

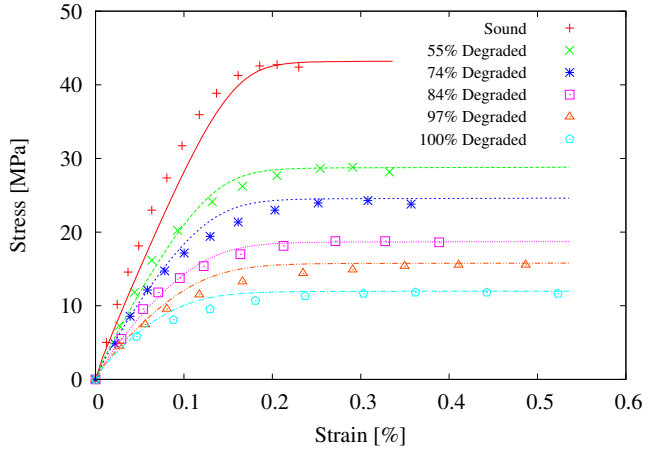

FIGURE 4.17: Stress-strain relationship of sound and leached concrete

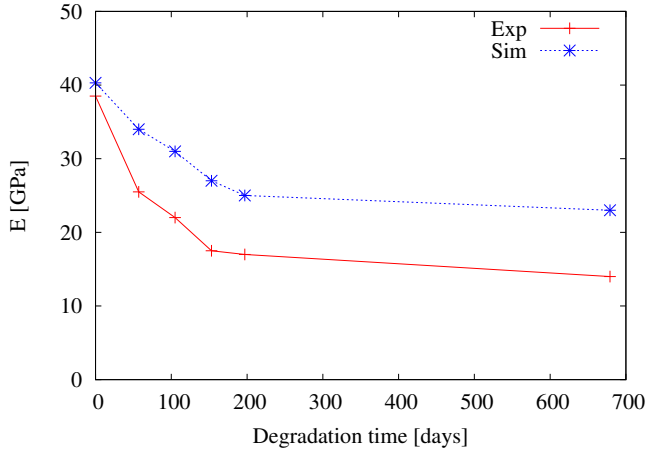

FIGURE 4.18: Comparison between the evolution of Young's modulus obtained by experimental tests and numerical predictions

4.4 Conclusion

In this chapter, a micromechanical based criterion with a non-associated flow rule was proposed to model the elastoplastic macroscopic behavior of a 4 phases material composed of a porous matrix reinforced with small and big inclusions. This new proposed model is in the first place applied for a concrete submitted to carbonation. Three homogenization steps, from microscale to macroscale were required using the so-called modified secant method. After the first homogenization, as the solid phase has been assumed to obey a Drucker-Prager criterion, the reinforced matrix also obeys the Drucker-Prager criterion with an increased frictional coefficient because of the effect of small inclusions. However, after the second homogenization by including the effect of pores the failure criterion changes to an elliptical form. For the elastoplastic modeling, an elastic threshold is supposed by means of the frictional coefficient of the solid phase. The hardening is taken into account by increase of the frictional coefficient with the equivalent plastic deformation. The evolution of porosity and inclusions during loading is taken into account in function of the evolution of the dilatancy coefficient of solid phase and the equivalent plastic deformation. A parameter analysis has been performed to assess the effect of material properties on the failure criterion. The porosity and frictional coefficient proved to be more influential. The macroscopic criterion explicitly takes into account the porosity of the cement matrix, calcite grains and aggregates volume fractions. The strength of carbonated concrete can be evaluated by the model, knowing its microstructural properties. This new micro-macro approach brings more physical relation between the model and the strength of carbonated concrete. In a second time, the model has been used for lixiviation of concrete by neglecting effects of small inclusions and by increasing porosity throughout degradation. It is seen that the proposed model predicts well the main features observed in concrete carbonation and lixiviation.

Conclusion générale et perspertives

Ce travail de thèse a été dédié essentiellement à la modélisation du comportement mécanique des matériaux cimentaires, tel que la pâte de ciment et le béton qui sont soumis à la carbonatation ou à la lixiviation. Nous avons dans un premier temps considéré un modèle phénoménologique et dans un deuxième temps des modèles basés sur la micromécanique.

Dans la partie préliminaire de ce travail de thèse, la modélisation macroscopique du comportement élastoplastique d'une pâte de ciment pétrolier sous compression uniaxial et triaxial a été réalisée en utilisant un modèle de comportement phénoménologique de base. Les influences des dégradations chimiques sur les paramètres du modèle ont été identifiées. Une loi d'évolution a été proposée en fonction des paramètres pertinent estimé liée aux changements de la microstructure. Cette loi d'évolution a permis de rendre compte de l'effet de la porosité et de la calcite formée sur les réponses non-linéaire de la pâte de ciments sous l'effet de ces dégradations. Ce modèle a été pris par la suite comme base de modélisation de la localisation des déformations.

Pour simuler la rupture et l'instabilité des matériaux cimentaires, la localisation des déformations est étudiée. Cette méthode est basée sur une technique d'homogénéisation, qui prend en compte l'effet de l'affaiblissement par les microfissures locales provoquant une macrofissure. Le modèle a été implémenté dans un code de calcul par éléments finis et des applications numériques ont été réalisées sur des structures qui sont supposées être homogènes et isotropes. La sensibilité au maillage, l'effet du paramètre de longueur caractéristique, l'orientation de la fissure et la pression de confinement ont été analysés successivement. Une série d'essais de compression uniaxiale et triaxiale sont simulés pour identifier les paramètres de l'interface intervenant dans la localisation des déformations. Un très bon accord entre les prédictions numériques et les résultats expérimentaux est obtenu.

Afin de justifier le choix des approches multi-échelles, nous avons présenté au premier chapitre, une analyse bibliographique sur les hydrates et la microstructure de la pâte de ciment et sur leurs évolutions ainsi que sur celle de la microstructure durant les réactions chimiques induites par la carbonatation et lixiviation. En effet, la modification de la microstructure affecte le comportement mécanique macroscopique. Il est donc primordial, pour une modélisation plus rigoureuse, de les lier en proposant des modèles

micros-macros. Si un modèle macroscopique classique est utilisé, comme celui proposé dans le premier chapitre, il est alors nécessaire d'identifier les paramètres du modèle pour les différents taux de carbonatation ou de lixiviation. Cependant, l'utilisation d'une approche micro-macro permet d'établir explicitement la relation entre les deux. Une approximation a été réalisée pour les constituants du milieu hétérogène des matériaux cimentaires, deux échelles paraissent être essentielles. À une échelle microscopique, le matériau est considéré comme une phase solide représentée par le ciment qui entoure des grains de calcite si la carbonatation a lieu. À une échelle plus grande, c'est-à-dire mésoscopique, le matériau peut être approché par une matrice cimentaire poreuse qui est renforcée par des granulats systématiquement plus grands que les pores. Il est donc essentiel de prendre en compte l'effet de ces constituants sur le comportement mécanique. En ce qui concerne le comportement mécanique des constituants, il existe un fort contraste entre eux. Le comportement des grains de calcite et les granulats peut être considéré comme rigide. En revanche, la phase solide (ciment) est compressible et subit des déformations plastiques. Celle-ci est supposée obéir à un critère de Drucker-Prager.

Dans le Chapitre 3, un critère basé sur la micromécanique a été proposé pour décrire le comportement mécanique à la rupture d'une pâte de ciment soumise à la carbonatation. Les effets de la porosité et l'impact des grains de calcite formés durant la carbonatation sont explicitement pris en compte par le critère macroscopique. Deux homogénéisations basées sur [2] ont été nécessaires pour aboutir à ce critère. L'effet des pores dans la deuxième homogénéisation donne une forme elliptique au critère.

Pour le comportement élastoplastique, un seuil initial de la plasticité a été introduit à travers le coefficient de frottement de la phase solide. L'écrouissage plastique est pris en compte avec l'évolution du coefficient de frottement en fonction de la déformation plastique équivalente.

En effectuant quelques simulations numériques, une surestimation de déformation volumique a été constatée. Ce qui a motivé le développement d'un modèle micro-macro non associé en se basant principalement sur les résultats de Maghous and al. [2].

Tout au long de la carbonatation, le modèle est parfaitement capable de prédire le comportement du matériau en diminuant la porosité et en augmentant la fraction volumique de la calcite. Toutefois, pour la lixiviation, l'augmentation de la porosité seule ne suffit pas pour pouvoir prédire le comportement du matériau, il faut en effet aussi diminuer

le coefficient de frottement qui se dégrade au cours de la lixiviation. L'introduction d'une règle d'écoulement macroscopique non-associé a permis l'obtention de très bonnes prédictions.

Par la suite dans le chapitre 4, le modèle est étendu au cas des bétons. Une 3 ème homogénéisation a été effectuée pour prendre en compte l'effet des granulats. Une analyse paramétrique du modèle a été effectuée. Les effets du coefficient de frottement, de la porosité, de petites inclusions et de grosses inclusions sur le critère ont été montrés.

De façon générale, les résultats obtenus dans le cadre de ce travail sont convaincants et encourageants. Ils montrent une très bonne entente entre la finesse de description et la simplicité. Le choix des hypothèses de pores et inclusions sphériques semble approprié pour les matériaux isotropes étudiés dans cette thèse, ils conduisent à des résultats relativement simples et utiles pour des applications pratiques. Toutefois, un certain nombre de travaux futurs peuvent être envisagés:

Dans ce travail de thèse, durant les simulations numériques, nous avons considéré que des échantillons étaient homogènes. La porosité et la fraction volumique de la calcite sont des valeurs moyennes de la partie saine, partiellement dégradée et complètement dégradée. Il sera donc convenable de mettre en œuvre des calculs de structures pour prendre en compte la différence de comportement entre les différentes parties du matériau.

Ces modèle micro-macro pourrons également être couplés avec un modèle chimique qui donne la description quantitative des processus de dissolution et de carbonatation.

Pour l'instant l'interface matrice/inclusions et considérée comme étant parfaite. Pour le comportement radoucissant après le pic, il sera intéressant de prendre en compte l'effet de "debounding" ou autrement dit la décohésion entre la matrice et les inclusions.

Appendix A

Integration algorithm of the elastoplastic macroscopic model

A.1 Integration Algorithm

Schematic Integration diagram and Computation Procedures of the elastoplastic behavior of the constitutive model described in section 2.2 are presented here. The problem is as follow:

$$\begin{cases} \boldsymbol{\sigma}_{n+1} = \mathbb{C} : \left(\boldsymbol{\varepsilon}_{n+1} - \boldsymbol{\varepsilon}^p_{n+1}\right) \\ \boldsymbol{\varepsilon}^p_{n+1} = \boldsymbol{\varepsilon}^p_n + \Delta\boldsymbol{\varepsilon}^p \quad \text{with} \quad \Delta\boldsymbol{\varepsilon}^p = \Delta\lambda \dfrac{\partial G}{\partial \boldsymbol{\sigma}} \\ \gamma^p_{n+1} = \gamma^p_n + \Delta\gamma^p \\ F\left(\boldsymbol{\sigma}, \gamma^p\right) = 0 \\ \text{where} \quad \boldsymbol{\varepsilon}_{n+1} = \boldsymbol{\varepsilon}_n + \Delta\boldsymbol{\varepsilon} \quad \text{are known} \end{cases} \tag{A.1}$$

Having knowledge of $\boldsymbol{\varepsilon}$, the plastic deformation $\boldsymbol{\varepsilon}^p$ and the isotropic hardening γ^p_n at step n and the increment of deformation $\Delta\boldsymbol{\varepsilon}$, the values $\boldsymbol{\varepsilon}_{n+1}$, $\boldsymbol{\varepsilon}^p_{n+1}$ and γ^p_{n+1} as well as $\boldsymbol{\sigma}_{n+1}$ are to be determined while considering $\Delta\lambda$ by regarding it as unknown factor. This scheme is explicit and follows an algorithm of the type "Cutting Plane Algorithm " [120].

A.1.1 Elastic Prediction (Trial Stress)

It is primarily supposed that the increment is elastic, it is deduced that $\Delta\lambda = 0$ and $\boldsymbol{\varepsilon}^p_{n+1} = \boldsymbol{\varepsilon}^p_n$, one finds that $\boldsymbol{\sigma}_{n+1} = \mathbb{C} : \left(\boldsymbol{\varepsilon}_{n+1} - \boldsymbol{\varepsilon}^p_{n+1}\right)$. If the trial stress verifies $F\left(\boldsymbol{\sigma}, \gamma^p\right) \leq 0$, then the assumption of elastic stress is valid and the procedure for the current step is completed, otherwise the current step has to be corrected for plastic strain.

A.1.2 Plastic Correction

The plastic correction is carried out through an iterative procedure. For an iteration i, $\Delta\lambda^i$ is known and $\Delta\lambda^{i+1}$ is sought. It is defined that:

$$\begin{aligned}
&\boldsymbol{\sigma}^{(i+1)}_{n+1} = \mathbb{C} : \left(\boldsymbol{\varepsilon}_{n+1} - \boldsymbol{\varepsilon}^{p,(i)}_{n+1}\right) - \Delta\lambda^{(i+1)}\mathbb{C} : \frac{\partial G}{\partial \boldsymbol{\sigma}} \\
&\gamma^{p^{(i+1)}}_{n+1} = \gamma^{p^{(i)}}_n + \Delta\lambda^{(i+1)}\sqrt{\mathrm{dev}\frac{\partial G}{\partial \boldsymbol{\sigma}} : \mathrm{dev}\frac{\partial G}{\partial \boldsymbol{\sigma}}}, \quad \mathrm{dev}\frac{\partial G}{\partial \boldsymbol{\sigma}} = \frac{\partial G}{\partial \boldsymbol{\sigma}} - \left(\frac{\partial G}{\partial \sigma_m}\right)\boldsymbol{\delta} \\
&F\left(\boldsymbol{\sigma}^{(i+1)}_{n+1}, \gamma^{p^{(i+1)}}_{n+1}\right) = F^{(i+1)}_{n+1}
\end{aligned} \tag{A.2}$$

it is possible to solve this problem by using Taylor's series:

$$F^{(i+1)}_{n+1} = \frac{\partial F^{(i)}_{n+1}}{\partial \boldsymbol{\sigma}}\ \delta\boldsymbol{\sigma} + \frac{\partial F^{(i)}_{n+1}}{\partial \beta(\gamma^p)}\ \delta\beta + F^{(i)}_{n+1} = 0 \tag{A.3}$$

$$\delta(\Delta\lambda)\left[-\frac{\partial F}{\partial \boldsymbol{\sigma}} : \mathbb{C} : \frac{\partial G}{\partial \boldsymbol{\sigma}} + \frac{\partial F}{\partial \beta}\frac{\partial \beta}{\partial \gamma^p}\sqrt{\mathrm{dev}\frac{\partial G}{\partial \boldsymbol{\sigma}} : \mathrm{dev}\frac{\partial G}{\partial \boldsymbol{\sigma}}}\right] + F^{(i)}_{n+1} = 0 \tag{A.4}$$

where:

$$\delta(\Delta\lambda) = \frac{F^{(i)}_{n+1}}{\frac{\partial F}{\partial \boldsymbol{\sigma}} : \mathbb{C} : \frac{\partial G}{\partial \boldsymbol{\sigma}} - \frac{\partial F}{\partial \beta}\frac{\partial \beta}{\partial \gamma^p}\sqrt{\mathrm{dev}\frac{\partial G}{\partial \boldsymbol{\sigma}} : \mathrm{dev}\frac{\partial G}{\partial \boldsymbol{\sigma}}}} \tag{A.5}$$

one obtains then:

$$\Delta\lambda^{(i+1)} = \Delta\lambda^{(i)} + \delta(\Delta\lambda) \tag{A.6}$$

The corresponding algorithm is clarified through this synopsis:

1. Input data : $\boldsymbol{\varepsilon}_n, \boldsymbol{\varepsilon}_n^p, \Delta\boldsymbol{\varepsilon}$ *and* γ_n^p

2. Calculating the deformation at step $n+1$: $\varepsilon_{n+1} = \boldsymbol{\varepsilon}_n + \Delta\boldsymbol{\varepsilon}$

3. Initialize : $i = 0, \boldsymbol{\varepsilon}_{n+1}^{p^{(0)}} = \boldsymbol{\varepsilon}_n^p, \Delta\gamma_{n+1}^{(0)}$

$$\boldsymbol{\sigma}_{n+1}^{(0)} = \mathbb{C} : \left(\boldsymbol{\varepsilon}_{n+1} - \boldsymbol{\varepsilon}_{n+1}^{p^{(0)}}\right)$$

$$F_{n+1}^{(i)} = F(\boldsymbol{\sigma}_{n+1}^{(i)}, \gamma_{n+1}^{p^{(i)}})$$

IF $F_{n+1}^{(i)} \leq$ Tolerance THEN: EXIT

ELSE:

4. $$\delta(\Delta\lambda) = \frac{F_{n+1}^{(i)}}{\frac{\partial F}{\partial \boldsymbol{\sigma}} : \mathbb{C} : \frac{\partial G}{\partial \boldsymbol{\sigma}} - \frac{\partial F}{\partial \beta}\frac{\partial \beta}{\partial \gamma^p}\sqrt{\mathrm{dev}\frac{\partial G}{\partial \boldsymbol{\sigma}} : \mathrm{dev}\frac{\partial G}{\partial \boldsymbol{\sigma}}}}$$

5. Calculate new values for each iteration:

$$\boldsymbol{\sigma}_{n+1}^{(i+1)} = \boldsymbol{\sigma}_{n+1}^{(i)} - \delta(\Delta\lambda)\mathbb{C} : \frac{\partial F_{n+1}^{(i)}(\boldsymbol{\sigma}_{n+1}^{(i)}, \gamma_{n+1}^{p^{(i)}})}{\partial \boldsymbol{\sigma}}$$

$$\gamma_{n+1}^{p^{(i+1)}} = \gamma_n^{p^{(i)}} + \delta(\Delta\lambda)\sqrt{\mathrm{dev}\frac{\partial G}{\partial \boldsymbol{\sigma}} : \mathrm{dev}\frac{\partial G}{\partial \boldsymbol{\sigma}}}$$

$$\Delta\lambda^{i+1} = \lambda^i + \delta(\Delta\lambda)$$

$$\boldsymbol{\varepsilon}_{n+1}^{p^{(i+1)}} = \boldsymbol{\varepsilon}_n^{p^{(i)}} + \delta(\Delta\lambda)\frac{\partial G}{\partial \boldsymbol{\sigma}}$$

Set $i \leftarrow i+1$

ENDIF

6. EXIT

End of Algorithm

Appendix B

Localization Model

B.1 Model Implementation in THMpasa FE Code

THMpasa Finite Element Code

⋮

Element Loop

⋮

IF *Element is cracked*, THEN

⋆ Make average for σ, ε, $\Delta\varepsilon$ and Hardening Parameters

&

⋆ Enter just one time in Gauss Loop

END IF

⋮

Gauss Loop

IF *Element is Cracked* → Go to Interface model

ELSE → Go to Elastoplastic Macroscopique model

END IF

Models
- Elastoplastic Macroscopic Model
- Interface Model

IF *Interface Has Elastic Behavior* → Go back to Elastoplastic model

IF *Element is cracked*, → Affect results to all Gauss points

⋮

B.2 Interface Model Algorithm

1. Input data : ε_n, $\Delta\varepsilon$, σ_n, κ, t_n, g_n
2. $\varepsilon_{n+1} = \varepsilon_n + \Delta\varepsilon_n$

Elastic Process

3. $i = 0$

$[S] = \left([K^e] + \mu[N]^T[D][N]\right)^{-1}[N]^T[D]$

$\Delta g = [S]\Delta\varepsilon$

$$\text{Initialize} \begin{cases} t_{n+1}^{(0)} = t_n + [K^{ep}]\Delta g \\ \kappa_{n+1}^{(0)} = \kappa_n \\ \Delta\lambda^{(0)} = 0 \end{cases}$$

IF $f_{n+1}^{(i)} \leq$ Tolerance $\rightarrow$ THEN: Goto Step 5

ELSE: Start Plastic Process

Plastic Process

4. IF $f_{n+1}^{(i)} \leq$ Tolerance $\rightarrow$ Goto Step 5

$[S] = \left([K^{ep}] + \mu[N]^T[D][N]\right)^{-1}[N]^T[D]$

$\Delta g = [S]\Delta\varepsilon$

$$\delta(\Delta\lambda) = \frac{f_{n+1}^{(i)}}{\frac{\partial f}{\partial \boldsymbol{t}} \cdot \boldsymbol{K}^e \cdot \frac{\partial f}{\partial \boldsymbol{t}} - \frac{\partial f}{\partial \kappa}\sqrt{\frac{\partial f}{\partial \boldsymbol{t}} \cdot \frac{\partial f}{\partial \boldsymbol{t}}}}$$

$$t_{n+1}^{(i+1)} = t_{n+1}^{(i)} - \delta(\Delta\lambda)\boldsymbol{K}^e \cdot \frac{\partial f}{\partial \boldsymbol{t}}$$

$$\kappa_{n+1}^{(i+1)} = \kappa_{n+1}^{(i)} + \sqrt{\frac{\partial f}{\partial \boldsymbol{t}} \cdot \frac{\partial f}{\partial \boldsymbol{t}}}$$

$\Delta\lambda^{i+1} = \Delta\lambda^i + \delta(\Delta\lambda)$

Set $i \leftarrow i + 1$

ENDIF; Goto Step 4

Appendix C

Elastic Moduli of Calcite

C.1 Elastic moduli of calcite

By knowing elastic constants C_{ij} of calcite cristals from the literature, it becomes possible to calculate the effective shear and bulk modulus of calcite. In trigonal symmetry, like the case of calcite structure the stiffness matrix is represented here:

$$[C_{trigonal}] = \begin{bmatrix} C_{11} & C_{12} & C_{13} & C_{14} & 0 & 0 \\ C_{12} & C_{11} & C_{13} & -C_{14} & 0 & 0 \\ C_{13} & C_{13} & C_{33} & 0 & 0 & 0 \\ C_{14} & -C_{14} & 0 & C_{44} & 0 & 0 \\ 0 & 0 & 0 & 0 & C_{44} & C_{14} \\ 0 & 0 & 0 & 0 & C_{14} & C_{66} \end{bmatrix} \tag{C.1}$$

with the diagonal symmetry conditions $C_{ij} = C_{ji}$ and $C_{66} = \frac{1}{2}(C_{11} - C_{12})$

According to [121], voigt values of the effective shear and bulk modulus corresponding to the upper bound of effective moduli can be expressed by the following equations:

$$\mu = \frac{A - B + 3C}{5}; \quad k = \frac{A + 2B}{3} \tag{C.2}$$

where A,B,C are given by:

$$A = \frac{2C_{11} + C_{33}}{3}; \quad B = \frac{C_{12} + 2C_{13}}{3}; \quad C = \frac{2C_{44} + 0.5(C_{11} - C_{12})}{3}$$

Using equation (C.2) with $C_{11} = 148, C_{12} = 56, C_{13} = 55, C_{14} = -20, C_{33} = 85, C_{44} = 33$ which are taken from [122], gives the following moduli: $\mu_c = 37$ GPa and $k_c = 79$ GPa.

Knowing this, it becomes possible to find elastic modulus and poisson coefficient through the following equation:

$$E = \frac{9k\mu}{3k + \mu}; \quad \nu = \frac{3k - E}{6k} \tag{C.3}$$

Hence, $E_c = 95$ GPa and $\nu_c = 0.3$ are taken as the elastic parameters of calcite grains.

Appendix D

Synthetic Results of Carbonation and Lixiviation on Cement Paste from Chapter 2 and Chapter 3

D.1 Introduction

In Chapter 2 and Chapter 3 the effects of chemical degradations have been separately illustrated for each mechanical test. Here, the results of mechanical tests with the same confining pressure are gathered in one figure in order to provide more synthetic comparison of the effect of carbonation and lixiviation.

D.2 Results from chapter 2

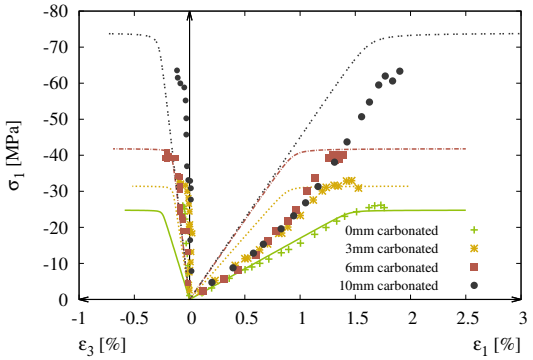

FIGURE D.1: Stress-strain curves of sound to carbonated cement paste in uniaxial compression test (Pc=0, Pi=0)

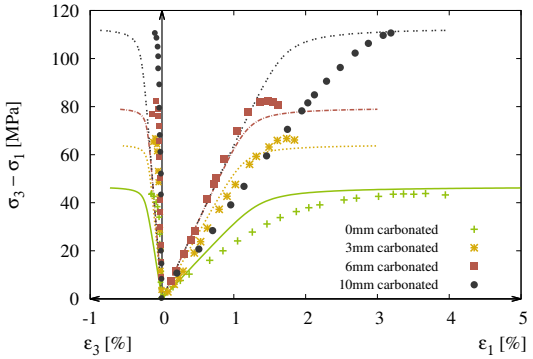

FIGURE D.2: Stress-strain curves of sound to carbonated cement paste in triaxial compression test (Pc=10, Pi=2.5)

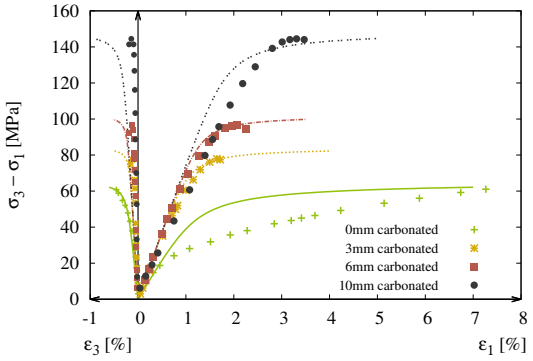

FIGURE D.3: Stress-strain curves of sound to carbonated cement paste in triaxial compression test (Pc=20, Pi=2.5)

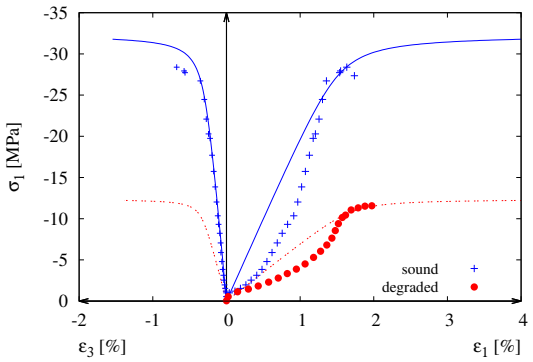

FIGURE D.4: Stress-strain curves of the sound and leached cement pastes in uniaxial compression test (Pc=0 MPa, Pi=0 MPa)

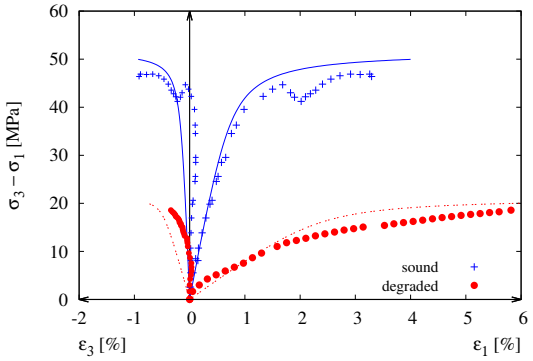

FIGURE D.5: Stress-strain curves of the sound and leached cement pastes in triaxial compression test (Pc=10 MPa, Pi=2.5 MPa)

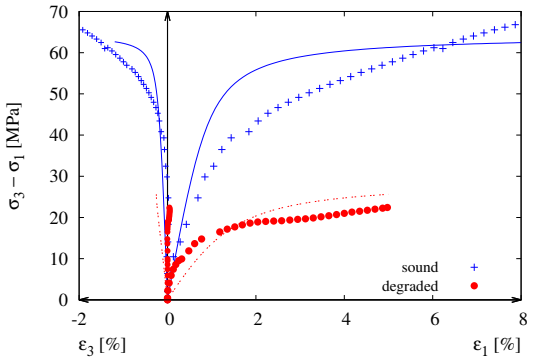

FIGURE D.6: Stress-strain curves of the sound and leached cement pastes in triaxial compression test (Pc=20 MPa, Pi=2.5 MPa)

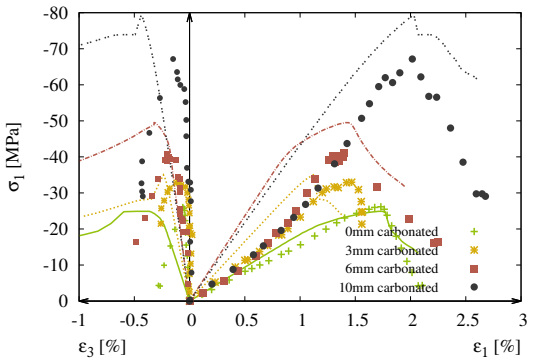

FIGURE D.7: Stress-strain curves of sound to carbonated cement paste in uniaxial compression test (Pc=0, Pi=0)

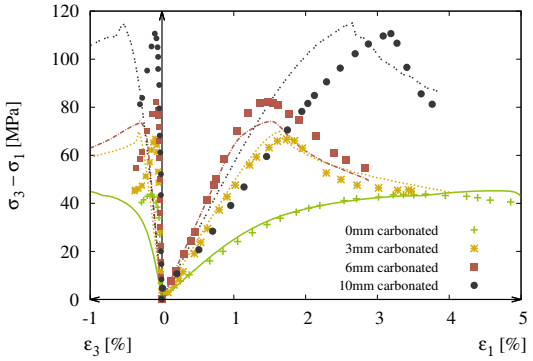

FIGURE D.8: Stress-strain curves of sound to carbonated cement paste in triaxial compression test (Pc=10, Pi=2.5)

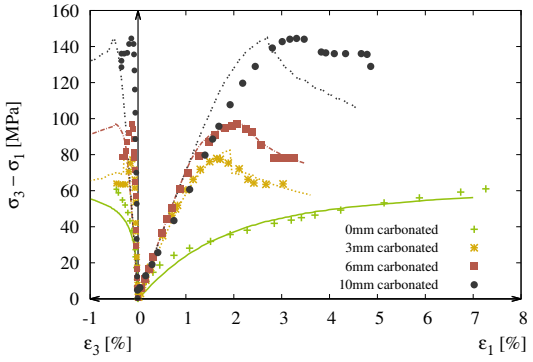

FIGURE D.9: Stress-strain curves of sound to carbonated cement paste in triaxial compression test (Pc=20, Pi=2.5)

D.3 Results from Chapter 3

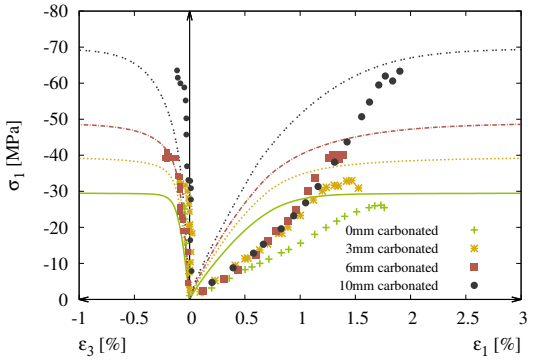

FIGURE D.10: Stress-strain curves of sound to carbonated cement paste in uniaxial compression test (Pc=0, Pi=0)

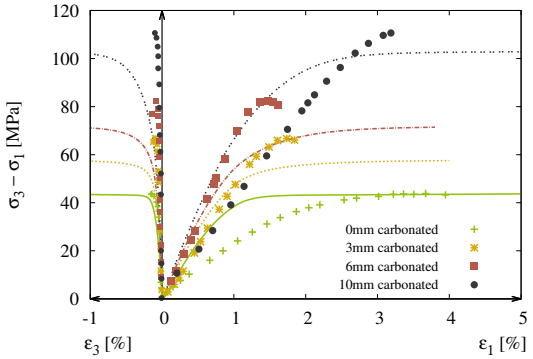

FIGURE D.11: Stress-strain curves of sound to carbonated cement paste in triaxial compression test (Pc=10, Pi=2.5)

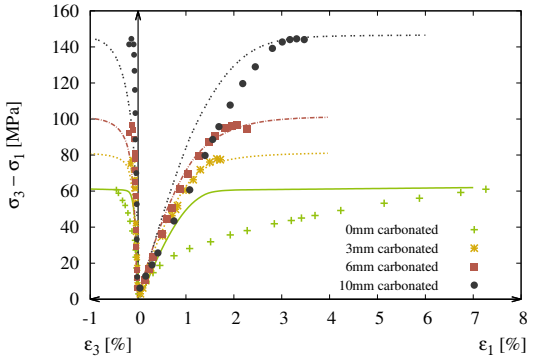

FIGURE D.12: Stress-strain curves of sound to carbonated cement paste in triaxial compression test (Pc=20, Pi=2.5)

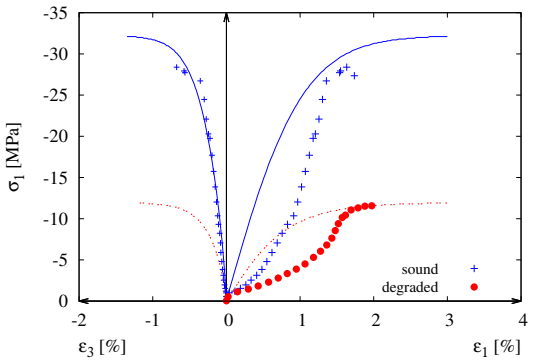

FIGURE D.13: Stress-strain curves of the sound and leached cement pastes in uniaxial compression test (Pc=0 MPa, Pi=0 MPa)

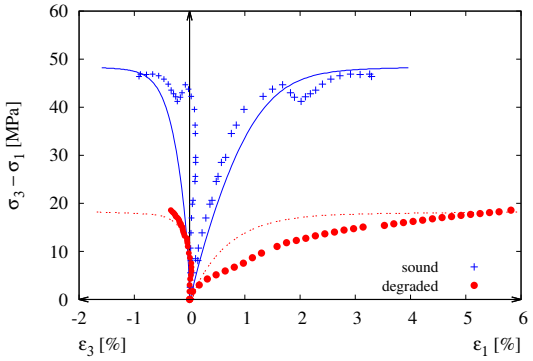

FIGURE D.14: Stress-strain curves of the sound and leached cement pastes in triaxial compression test (Pc=10 MPa, Pi=2.5 MPa)

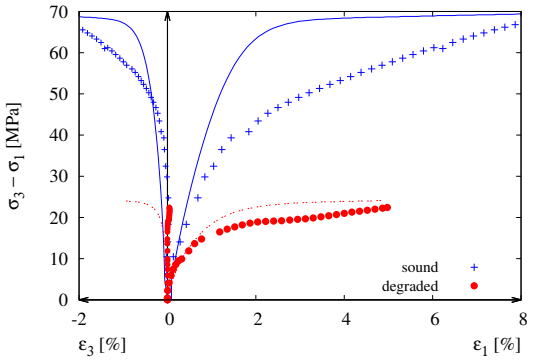

FIGURE D.15: Stress-strain curves of the sound and leached cement pastes in triaxial compression test (Pc=20 MPa, Pi=2.5 MPa)

Bibliography

[1] S. Pietruszczak, J. Jiang, and FA Mirza. An elastoplastic constitutive model for concrete. *International journal of solids and structures*, 24(7):705–722, 1988.

[2] S. Maghous, L. Dormieux, and J. F. Barthélémy. Micromechanical approach to the strength properties of frictional geomaterials. *European Journal of Mechanics - A/Solids*, 28(1):179–188, 2009.

[3] I Van Odler. Hydration, setting and hardening of portland cement. *Lea's chemistry of cement and concrete*, page 241, 2003.

[4] E. Gallucci and K. Scrivener. Crystallisation of calcium hydroxide in early age model and ordinary cementitious systems. *Cement and Concrete Research*, 37(4): 492–501, April 2007.

[5] Jean-Pierre Ollivier and Angélique Vichot. *La durabilité des bétons : Bases scientifiques pour la formulation de bétons durables dans leur environnement.* Presses Ponts et Chaussées, Paris, 2008.

[6] S. Brunauer and S. A. Greenberg. The hydration of tricalcium silicate and β dicalcium silicate at room temperature. *4^{th} International Symposium on the Chemistry of Cement, Washington*, pages 135–165, 1900.

[7] R. F. Feldman and P. J. Sereda. A model for hydrated portland cement paste as deduced from sorption-length change and mechanical properties. *Matériaux et Construction*, 1(6):509–520, November 1968.

[8] G.J. Verbeck and R.H. Helmuth. Structures and physical properties of cement paste. In *Principal paper, lntemational Symposium on Cement Chemistry, Tokyo*, 1968.

[9] J. Therrien, B. Bissonnette, and A. Cloutier. Early-age evolution of the mass transfer properties in mortar and its influence upon ultimate shrinkage. pages 247 – 268. RILEM Publications, 2000. Editors: V. Baroghel-Bouny and P.-C. Aïtcin.

[10] H.F.W. Taylor. *Cement chemistry.* Thomas Telford, 1997.

[11] K.O. Kjellsen, R.J. Detwiler, and O.E. Gjørv. Development of microstructures in plain cement pastes hydrated at different temperatures. *Cement and Concrete Research*, 21(1):179–189, 1991.

[12] A.M. Neville. *Properties of concrete*. 1995.

[13] J.-C. Maso. La liaison pâte-granulats. *Le béton hydraulique : connaissance et pratique, édité par Baron J. et Sauterey R., Presses de l'Ecole Nationale des Ponts et Chaussées*, pages 247–259, 1982.

[14] V. Baroghel-Bouny. *Caracterisation des pates de ciment et des betons - Methodes, Analyse, Interpretations*. PhD thesis, 1994.

[15] Ngoc Tru VU. *Contribution à l'étude de la corrosion par carbonatation du béton armé : approche expérimentale et probabiliste*. PhD thesis, University of Toulouse, 2011.

[16] Thierry Chaussadent. *Etat des lieux et réflexions sur la carbonatation du béton armé*. Laboratoire central des ponts et chaussées, Paris, 1999.

[17] M. Thiery. *Modélisation de la carbonatation atmosphérique des materiaux cimentaires; Prise en compte des effets cinétique et des modifications microstructurales et hydriques*. PhD thesis, Ecole Nationale des Ponts et Chaussées, 2005.

[18] M. Valcuende and C. Parra. Natural carbonation of self-compacting concretes. *Construction and Building Materials*, 24(5):848–853, 2010.

[19] Jiang Jhy Chang, Weichung Yeih, Ran Huang, and Chun Tao Chen. Suitability of several current used concrete durability indices on evaluating the corrosion hazard for carbonated concrete. *Materials Chemistry and Physics*, 84(1):71–78, 2004.

[20] Edward Bryant. *Climate process & change*. Cambridge University Press, Cambridge; New York, 1997.

[21] F. John Fayers. *Enhanced oil recovery: Proceedings of the third European Symposium on Enhanced Oil Recovery, held in Bournemouth, U.K., September 21-23, 1981*. Elsevier, 1981.

[22] Min Zhang and Stefan Bachu. Review of integrity of existing wells in relation to CO2 geological storage: What do we know? *International Journal of Greenhouse Gas Control*, 5(4):826–840, July 2011.

[23] V. Barlet-Gouédard, G. Rimmelé, B. Goffé, and O. Porcherie. Well technologies for CO_2 geological storage: CO_2-resistant cement. *Oil & Gas Science and Technology - Revue de l'IFP*, 62(3):325–334, May 2007.

[24] A. Fabbri, J. Corvisier, A. Schubnel, F. Brunet, B. Goffé, G. Rimmele, and V. Barlet-Gouédard. Effect of carbonation on the hydro-mechanical properties of portland cements. *Cement and Concrete Research*, 39(12):1156–1163, December 2009.

[25] Van der Lee, J and De Windt, L. CHESS tutorial and Cookbook/Version 3.0, users manual LHM. Technical report, RD/02/13, Ecole des mines de Paris, Fontainebleau, 2002.

[26] Emeline Drouet. *Impact de la température sur la carbonatation des matériaux cimentaires : prise en compte des transferts hydriques*. PhD thesis, École normale supérieure de Cachan - ENS Cachan, 2010.

[27] L. N. Plummer, T. M. L. Wigley, and D. L. Parkhurst. The kinetics of calcite dissolution in CO_2 -water systems at 5 degrees to 60 degrees c and 0.0 to 1.0 atm CO_2. *American Journal of Science*, 278(2):179–216, 1978.

[28] L. Niel Plummer and Eurybiades Busenberg. The solubilities of calcite, aragonite and vaterite in CO2-H2O solutions between 0 and 90°C, and an evaluation of the aqueous model for the system CaCO3-CO2-H2O. *Geochimica et Cosmochimica Acta*, 46(6):1011–1040, 1982.

[29] Barbara G. Kutchko, Brian R. Strazisar, David A. Dzombak, Gregory V. Lowry, and Niels Thaulow. Degradation of well cement by CO2 under geologic sequestration conditions. *Environmental Science & Technology*, 41(13):4787–4792, July 2007.

[30] Andrew Duguid. An estimate of the time to degrade the cement sheath in a well exposed to carbonated brine. *Energy Procedia*, 1(1):3181–3188, February 2009.

[31] M. Lesti, C. Tiemeyer, and J. Plank. CO2 stability of portland cement based well cementing systems for use on carbon capture & storage (CCS) wells. *Cement and Concrete Research*, 45:45–54, 2013.

[32] Y. H. Loo, M. S. Chin, C. T. Tam, and K. C. G. Ong. A carbonation prediction model for accelerated carbonation testing of concrete. *Magazine of Concrete Research*, 46(168):191–200, 1994.

[33] I. Takla. *Comportement Thermo-Hydro-Mécanique d'un ciment pétrolier sous l'effet du CO2*. PhD thesis, University of Sciences and Technologies of Lille, 2010.

[34] Cheng-Feng Chang and Jing-Wen Chen. The experimental investigation of concrete carbonation depth. *Cement and Concrete Research*, 36(9):1760–1767, September 2006.

[35] M. Thiery, G. Villain, P. Dangla, and G. Platret. Investigation of the carbonation front shape on cementitious materials: Effects of the chemical kinetics. *Cement and Concrete Research*, 37(7):1047–1058, 2007.

[36] Nourreddine Rafaï, Hugues Hornain, Géraldine Villain, Véronique Baroghel Bouny, Gérard Platret, and Thierry Chaussadent. Comparaison et validité des méthodes de mesure de la carbonatation. *Revue Française de Génie Civil*, 6(2): 251–274, January 2002.

[37] Y. Lo and H. M. Lee. Curing effects on carbonation of concrete using a phenolphthalein indicator and fourier-transform infrared spectroscopy. *Building and Environment*, 37(5):507–514, May 2002.

[38] George J Verbeck. *Carbonation of hydrated Portland cement*. [Portland Cement Association], Chicago, 1958.

[39] Yves F. Houst and Folker H. Wittmann. Depth profiles of carbonates formed during natural carbonation. *Cement and Concrete Research*, 32(12):1923–1930, December 2002.

[40] Yves Freddy Houst. *Diffusion de gaz, carbonatation et retrait de la pâte de ciment durcie*. PhD thesis, EPFL, Lausanne, 1993.

[41] V. T. Ngala and C. L. Page. Effects of carbonation on pore structure and diffusional properties of hydrated cement pastes. *Cement and Concrete Research*, 27(7):995–1007, July 1997.

[42] Emilio Zornoza, Jordi Payá, José Monzó, María V. Borrachero, and Pedro Garcés. The carbonation of OPC mortars partially substituted with spent fluid catalytic catalyst (FC3r) and its influence on their mechanical properties. *Construction and Building Materials*, 23(3):1323–1328, March 2009.

[43] V. G. Papadakis, C. G. Vayenas, and M. N. Fardis. Physical and chemical characteristics affecting the durability of concrete. *ACI Materials Journal*, 88(2):186–196, April 1991.

[44] M. Thiéry, V. Baroghel-Bouny, A. Morandeau, and P. Dangla. Impact of carbonation on the microstructure and transfer properties of cement-based materials. *Transfert2012*, 2012.

[45] S. E. Pihlajavaara. Some results of the effect of carbonation on the porosity and pore size distribution of cement paste. *Matériaux et Construction*, 1(6):521–527, November 1968.

[46] W Eitel. *Silicate science. Volume V, Volume V,*. Academic Press, New York, 1966.

[47] E. G. Swenson and P. J. Sereda. Mechanism of carbonation shrinkage of lime and hydrated cement. *Journal Applied Chemistry /UK/*, April 1968.

[48] H. Hornain. Carbonatation accélérée et résistances mécaniques. In *Rilem International Symposium, Carbonation of Concrete, Cement and Concrete Association*, page paper 5.2, Slough, 1976.

[49] D. I. Rodway, G. W. Groves, and I. G. Richardson. The carbonation of hardened cement pastes. *Advances in Cement Research*, 3(11):117–125, July 1990.

[50] S. E. Pihlajavaara. An experimental study of the effect of carbonation on the strength of concrete. *RILEM International Symposium, Carbonation of concrete, Cement and Concrete Association, Slough,*, Paper 4.5, 1976.

[51] Jianzhuang Xiao, Jie Li, Bolong Zhu, and Ziyan Fan. Experimental study on strength and ductility of carbonated concrete elements. *Construction and Building Materials*, 16(3):187–192, April 2002.

[52] Cheng-Feng Chang and Jing-Wen Chen. Strength and elastic modulus of carbonated concrete. *ACI Materials Journal*, 102(5):315–321, 2005.

[53] Ján Jerga. Physico-mechanical properties of carbonated concrete. *Construction and Building Materials*, 18(9):645–652, 2004.

[54] I. Takla, N. Burlion, J. Shao, J. Saint-Marc, and A. Garnier. Effects of the storage of CO2 on multiaxial mechanical and hydraulic behaviors of oil-well cement. *Journal of Materials in Civil Engineering*, 23(6):741–746, 2011.

[55] Kristada Sisompho et Lutz Franke. Carbonation rates of concretes containing high volume of pozzolanic materials. *Cement and Concrete Research*, 37:1647–1653, 2007.

[56] Ismail Yurtdas, He Peng, Nicolas Burlion, and Frédéric Skoczylas. Influences of water by cement ratio on mechanical properties of mortars submitted to drying. *Cement and Concrete Research*, 36(7):1286–1293, 2006.

[57] M. C. M. Nasvi, P. G. Ranjith, and J. Sanjayan. Effect of different mix compositions on apparent carbon dioxide (CO2) permeability of geopolymer: Suitability as well cement for CO2 sequestration wells. *Applied Energy*, 114:939–948, February 2014.

[58] Nadine Neuville, Georges Aouad, Eric Lecolier, and Denis Damidot. Innovative leaching tests of an oilwell cement paste for CO2 storage: Effect of the pressure at 80°c. *Energy Procedia*, 23:472–479, 2012.

[59] E. Lécolier, A. Rivereau, G. Le Saoût, and A. Audibert-Hayet. Durability of hardened portland cement paste used for oilwell cementing. *Oil & Gas Science and Technology - Revue de l'IFP*, 62(3):335–345, May 2007.

[60] Nadine Neuville, Eric Lécolier, Georges Aouad, Alain Rivereau, and Denis Damidot. Effect of curing conditions on oilwell cement paste behaviour during leaching: Experimental and modelling approaches. *Comptes Rendus Chimie*, 12(3-4):511–520, March 2009.

[61] Jean-Michel Torrenti, Olivier Didry, Jean-Pierre Ollivier, and Frédéric Plas. *La degradation des betons. Couplage fissuration-dégradation chimique*. Hermes Science Publications, Paris, January 1999.

[62] U. Berner. *A Thermodynamic Description of the Evolution of Pore Water Chemistry and Uranium Speciation During the Degradation of Cement*. Paul-Scherrer-Institut, 1990.

[63] Viet-Hung Nguyen. *Couplage dégradation chimique - comportement en compression du béton*. PhD thesis, Ecole des Ponts ParisTech, 2005.

[64] Frederic Adenot. *Durabilite du beton : caracterisation et modelisation des processus physiques et chimiques de degradation du ciment*. PhD thesis, Orléans, 1992.

[65] Christophe Carde. *Caractérisation et modélisation de l'altération des propriétés mécaniques due à la lixiviation des matériaux cimentaires*. Thèse de doctorat, INSA Toulouse,, S.l, France, 1996.

[66] Hiroshi Saito and Akira Deguchi. Leaching tests on different mortars using accelerated electrochemical method. *Cement and Concrete Research*, 30(11):1815–1825, 2000.

[67] F. H Heukamp, F. J Ulm, and J. T Germaine. Mechanical properties of calcium-leached cement pastes: Triaxial stress states and the influence of the pore pressures. *Cement and Concrete Research*, 31(5):767–774, 2001.

[68] T. de Larrard, F. Benboudjema, J. B. Colliat, J. M. Torrenti, and F. Deleruyelle. Concrete calcium leaching at variable temperature: Experimental data and numerical model inverse identification. *Computational Materials Science*, 49(1):35–45, 2010.

[69] Siham Kamali, Bruno Gérard, and Micheline Moranville. Modelling the leaching kinetics of cement-based materials—influence of materials and environment. *Cement and Concrete Composites*, 25(4–5):451–458, 2003.

[70] H. Yang, L. Jiang, Y. Zhang, and Q. Pu. Flexural strength of cement paste beam under chemical degradation: Experiments and simplified modeling. *Journal of Materials in Civil Engineering*, 25(5):555–562, 2013.

[71] V. H. Nguyen, H. Colina, J. M. Torrenti, C. Boulay, and B. Nedjar. Chemo-mechanical coupling behaviour of leached concrete: Part I: Experimental results. *Nuclear Engineering and Design*, 237(20-21):2083–2089, November 2007.

[72] Christophe Carde, Raoul François, and Jean-Michel Torrenti. Leaching of both calcium hydroxide and c-s-h from cement paste: Modeling the mechanical behavior. *Cement and Concrete Research*, 26(8):1257–1268, August 1996.

[73] Christophe Carde and Raoul François. Modelling the loss of strength and porosity increase due to the leaching of cement pastes. *Cement and Concrete Composites*, 21(3):181–188, 1999.

[74] Christophe Carde and Raoul François. Effect of the leaching of calcium hydroxide from cement paste on mechanical and physical properties. *Cement and Concrete Research*, 27(4):539–550, 1997.

[75] Franz H Heukamp, Franz-Josef Ulm, and John T Germaine. Poroplastic properties of calcium-leached cement-based materials. *Cement and Concrete Research*, 33(8): 1155–1173, August 2003.

[76] C. Bellégo, B. Gérard, and G. Pijaudier-Cabot. Chemo-mechanical effects in mortar beams subjected to water hydrolysis. *Journal of Engineering Mechanics*, 126 (3):266–272, 2000.

[77] S. Y. Xie, J. F. Shao, and N. Burlion. Experimental study of mechanical behaviour of cement paste under compressive stress and chemical degradation. *Cement and Concrete Research*, 38(12):1416–1423, 2008.

[78] I. Yurtdas, SY Xie, N. Burlion, J.F. Shao, J. Saint-Marc, and A. Garnier. Influence of chemical degradation on mechanical behavior of a petroleum cement paste. *Cement and Concrete Research*, 41(4):412–421, 2011.

[79] Bruno Gérard. *Contribution des couplages mécanique-chimie : transfert dans la tenue à long terme des ouvrages de stockage de dechets radioactifs*. PhD thesis, Cachan, Ecole normale supérieure, 1996.

[80] Franz-Josef Ulm, Franz H. Heukamp, and John T. Germaine. Residual design strength of cement-based materials for nuclear waste storage systems. *Nuclear Engineering and Design*, 211(1):51–60, January 2002.

[81] F. Agostini, Z. Lafhaj, F. Skoczylas, and H. Loodsveldt. Experimental study of accelerated leaching on hollow cylinders of mortar. *Cement and Concrete Research*, 37(1):71–78, January 2007.

[82] Caroline Le Bellego. *Couplage chimie-mécanique dans les structures en béton attaquées par l'eau : étude expérimentale et analyse numérique*. PhD thesis, Laboratoire de mécanique et technologie, ENS Cachan, 2001.

[83] P. Jamet, A. Millard, and G. Nahas. Triaxial behaviour of a micro-concrete complete stress-strain curves for confining pressures ranging from 0 to 100 mpa. In *International conference on concrete under multiaxial conditions. Toulouse: RILEM*, 1984.

[84] D. Sfer, I. Carol, R. Gettu, and G. Etse. Study of the behavior of concrete under triaxial compression. *Journal of engineering mechanics*, 128(2):156–163, 2002.

[85] P. Menetrey and K. William. A triaxial failure criterion for concrete and its generalisation (department of civil, environmental, and architectural engineering, university of colorado at boulder). Technical report, CU/SR-93/12, 1993.

[86] HB Poorooshasb and S. Pietruszczak. On yielding and flow of sand; a generalized two-surface model. *Computers and Geotechnics*, 1(1):33–58, 1985.

[87] C. J. Haecker, E. J. Garboczi, J. W. Bullard, R. B. Bohn, Z. Sun, S. P. Shah, and T. Voigt. Modeling the linear elastic properties of portland cement paste. *Cement and Concrete Research*, 35(10):1948–1960, October 2005.

[88] S. Pietruszczak and G. Xu. Brittle response of concrete as a localization problem. *International Journal of Solids and Structures*, 32(11):1517–1533, June 1995.

[89] S.-C. R. Lo, I. K. Lee, and J. Chu. Strain softening and shear band formation of sand in multi-axial testing. *Géotechnique*, 46(1):63–82, January 1996.

[90] Zhiwei Gao and Jidong Zhao. Strain localization and fabric evolution in sand. *International Journal of Solids and Structures*, 50(22–23):3634–3648, October 2013.

[91] Sajjad Maqbool and Junichi Koseki. Large-scale plane strain compression tests on compacted gravel. 2007.

[92] K. Alshibli and S. Sture. Shear band formation in plane strain experiments of sand. *Journal of Geotechnical and Geoenvironmental Engineering*, 126(6):495–503, 2000.

[93] Caifeng Jin. *Modélisation multi-échelle du comportement mécanique des matériaux cimentaires – effets des agrégats*. PhD thesis, Université Lille 1, 2012.

[94] S. Pietruszczak and X. Niu. On the description of localized deformation. *International Journal for Numerical and Analytical Methods in Geomechanics*, 17(11): 791–805, November 1993.

[95] James R Rice. *The localization of plastic deformation*. Division of Engineering, Brown University, 1976.

[96] B. Shieh-Beygi and S. Pietruszczak. Numerical analysis of structural masonry: mesoscale approach. *Computers & Structures*, 86(21–22):1958–1973, November 2008.

[97] A. Abou-Chakra Guery, F. Cormery, J.-F. Shao, and D. Kondo. A micromechanical model of elastoplastic and damage behavior of a cohesive geomaterial. *Int.J.Solids Struct*, 45(5):1406–1429, 2008.

[98] W.Q. Shen, J.F. Shao, D. Kondo, and B Gatmiri. A micro-macro model for clayey rocks with a plastic compressible porous matrix. *International Journal of Plasticity*, 36:64–85, 2012.

[99] W. Q. Shen, D. Kondo, L. Dormieux, and J. F. Shao. A closed-form three scale model for ductile rocks with a plastically compressible porous matrix. *Mechanics of Materials*, 59:73–86, April 2013.

[100] P. Suquet. Overall properties of nonlinear composites: a modified secant moduli approach and its link with pont castaneda's nonlinear variational procedure. *C.R.Acad.Sc.Paris,IIb*, 320:563–571, 1995.

[101] P. Ponte Castaneda. The effective mechanical properties of nonlinear isotropic composites. *J.Mech.Phys.Solids*, 39:45–71, 1991.

[102] P. Ponte Castaneda. New variational principles in plasticity and their application to composite materials. *J.Mech.Phys.Solids*, 40:1757–1788, 1992.

[103] P. Suquet. Effective properties of nonlinear composites. in: Suquet, p.(ed), continuum micromechanics. vol. 377 of cism lecture notes. *C.R.Acad.Sc.Paris,IIb*, Springer Verlage, New York:pp.197–264, 1997.

[104] P. Ponte Castaneda and P. Suquet. Nonlinear composites. *Adv.Appl.Mech.,Academic Press, New York*, 34:171–302, 1998.

[105] J.F. Barthélémy and L. Dormieux. A micromechanical approach to the strength criterion of drucker-prager materials reinforced by rigid inclusions. *International Journal for Numerical and Analytical Methods in Geomechanics*, 28:565–582, 2004.

[106] L. Dormieux, A. Molinari, and D. Kondo. Micromechanical approach to the behavior of poroelastic materials. *Journal of the Mechanics and Physics of Solids*, 50:2203–2231, 2002.

[107] Wan Qing Shen. *Modélisations micro-macro du comportement mécanique des matériaux poreux ductiles : application à l'argilite du Callovo-Oxfordien.* PhD thesis, Université de Lille 1, 2011.

[108] P. Suquet. Overall properties of nonlinear composites: a modified secant moduli theory and its link with ponte castañeda's nonlinear variational procedure. *Comptes rendus de l'Académie des sciences. Série II, Mécanique, physique, chimie, astronomie*, 320(11):563–571.

[109] Jean-François Barthélémy and Luc Dormieux. A micromechanical approach to the strength criterion of drucker-prager materials reinforced by rigid inclusions. *International Journal for Numerical and Analytical Methods in Geomechanics*, 28 (7-8):565–582, 2004.

[110] P. Suquet. Effective properties of nonlinear composites. In P. Suquet, editor, *Continuum Micromechanics*, number 377 in International Centre for Mechanical Sciences, pages 197–264. Springer Vienna, January 1997.

[111] Z. Hashin and S. Shtrikman. A variational approach to the theory of the elastic behaviour of multiphase materials. *Journal of the Mechanics and Physics of Solids*, 11(2):127–140, 1963.

[112] L. Dormieux, A. Molinari, and D. Kondo. Micromechanical approach to the behavior of poroelastic materials. *Journal of the Mechanics and Physics of Solids*, 50(10):2203–2231, 2002.

[113] Q. Z. Zhu, J. F. Shao, and M. Mainguy. A micromechanics-based elastoplastic damage model for granular materials at low confining pressure. *International Journal of Plasticity*, 26(4):586–602, 2010.

[114] Akhtar S. Khan, Ying Xiang, and Sujian Huang. Behavior of berea sandstone under confining pressure part i: Yield and failure surfaces, and nonlinear elastic response. *International Journal of Plasticity*, 7(6):607–624, 1991.

[115] Jiang Jhy Chang, Weichung Yeih, Ran Huang, and Jack Maochieh Chi. Mechanical properties of carbonated concrete. *Journal of the Chinese Institute of Engineers*, 26(4):513–522, 2003.

[116] T Mori and K Tanaka. Average stress in matrix and average elastic energy of materials with misfitting inclusions. *Acta Metallurgica*, 21(5):571–574, 1973.

[117] Upendra J. Counto. The effect of the elastic modulus of the aggregate on the elastic modulus, creep and creep recovery of concrete. *Magazine of Concrete Research*, 16(48):129–138, 1964.

[118] Peter Simeonov and Shuaib Ahmad. Effect of transition zone on the elastic behavior of cement-based composites. *Cement and Concrete Research*, 25(1):165–176, 1995.

[119] M. Anson and K. Newman. The effect of mix proportions and method of testing on poisson's ratio for mortars and concretes. *Magazine of Concrete Research*, 18 (56):115–130, 1966.

[120] JC Simof and TJR Hughes. Computational inelasticity. 2008.

[121] W. Pabst, G. Ticha, and E. Gregorova. Effective elastic properties of alumina-zirconia composite ceramics-part 3. calculation of elastic moduli of polycrystalline alumina and zirconia from monocrystal data. *Ceramics- Silikaty*, 48(2):41—48, 2004.

[122] William M. Haynes, David R Lide, and Thomas J Bruno. *CRC handbook of chemistry and physics a ready-reference book of chemical and physical data: 2013-2014*. CRC Press, Boca Raton (Fla.); London; New York, 2013.